The baryon content of distant X-ray Galaxy Clusters

Dissertation der Fakultät für Physik
der
Ludwig-Maximilians-Universität München

vorgelegt von Joana Pedroso Raio Silvério dos Santos
aus Sintra, Portugal

München, September 2008

1. Gutachter:	Prof. Dr. Hans Böhringer
2. Gutachter:	Prof. Dr. Ortwin Gerhard
Tag der mündlichen Prüfung:	09.12.2008

When one sees eternity in things that pass away
and infinity in finite things,
then one has pure knowledge.
But if one mereley sees the diversity of things,
with their divisions and limitations,
then one has impure knowledge.
And if one selfishly sees a thing as if it were everything,
independent of the ONE and the many,
then one is in the darkness of ignorance.
Baghavad Gita, XVIII. 20-22

If a man will begin with certainties,
he shall end in doubts,
but if he will be content to begin with doubts,
he shall end in certainties.
Francis Bacon, "The Advancement of Learning", Book V

Ideas are like fish.
If you want to catch little fish, you can stay in the shallow water.
But if you want to catch the big fish, you've got to go deeper.
David Lynch, "Catching the big fish"

What am I doing here?
Bruce Chatwin

Contents

Zusammenfassung

Galaxienhaufen sind die größten virialisierten Systeme im Universum. Im Rahmen des weitgehend akzeptierden Standardmodells sind Galaxienhaufen Materiekonzentrationen, die durch sogenannte dunkle Materie dominiert werden. Auf den Gehalt an herkömmlicher Materie, kurz als Baryonen bezeichnet, entfallen rund 15% des Gesamtbetrags der Haufenmasse, die eine kalte Phase in Form der leuchtenden Galaxien, und eine heiße Phase in Form von einem heißen intergalaktischen Medium (ICM) beinhalten. Während das Verhalten der Dunklen Materie nur durch die Gravitation bestimmt wird und relativ einfach beschreibbar ist, wird die Entwicklung der baryonischen Materie wesentlich auch durch nicht-gravitative Prozesse beeinflusst, wie Kühlung, Sternbildung und Feedback-Mechanismen. Das Zusammenspiel der komplexen Prozesse zwischen der "kalten" und "heißen" baryonischen Phase ist weitgehend ungeklärt.

In dieser Arbeit untersuche ich die Eigenschaften des ICM und die Galaxienpopulation in entfernten Galaxienhaufen, die durch Röntgenbeobachtungen entdeckt wurden, mit dem Ziel, mehr über die physikalischen Prozesse zu erfahren, die die Entwicklung von Galaxienhaufen, ihres ICM und ihrer Galaxienpopulation bestimmen.

Die inneren Regionen von nahen Galaxienhaufen zeigen oft intensive Strahlungskühlung und werden daher als "cool cores" (CC) bezeichnet. Wir haben einen wichtigen Schritt bei der Untersuchung von "cool cores" in entfernten Galaxienhaufen unternommen, indem wir eine effiziente Methode der Identifizierung von "cool cores" an Hand von nahen, gut untersuchten Galaxienhaufen entwickelt haben und diese dann auf eine Stichprobe der entferntesten Galaxienhaufen (im Rotverschiebungsbereich z = 0.7 - 1.4) mit Beobachtungen aus dem *Chandra* Archiv angewandt haben. Der Anteil an "cool cores" in der Galaxienhaufenpopulation nimmt offenbar mit der Rotverschiebung ab. Ich finde, dass die meisten entfernten Galaxienhaufen nur moderate aber keine starken "cool cores" besitzen, die auf einen intermediären Zustand der Kühlung hinwiesen.

Hochrotverschobene Galaxienhaufen (z >1) sind schwer zu finden. Das XMM-Newton Distant Cluster-Projekt (XDCP) ist eine Himmelsdurchmusterung zur Konstruktion einer Stichprobe von entfernten, röntgenleuchtenden Galaxienhaufen, die in Archivdaten von *XMM-Newton* Beobachtungen entdeckt werden können. Im Rahmen dieses Projekts wurde eine große Anstrengung unternommen, um Galaxienhaufen mit

Hilfe von optischen/Nahinfrarot Beobachtungen und einer zwei-Farben Methode sicher zu identifizieren und einen groben Wert für die Rotverschiebung abzuschätzen. Dafür wurden in einem Teilprojekt 22 Galaxienhaufen in zwei Beobachtungskampagnien auf dem ESO/La Silla Observatorium beobachtet. Auf Grund der Farbaufnahmen im I und H band konnte die Hälfte der Haufen als potentielle, entfernte Haufenkandidaten identifiziert werden. Die angewandte photometrische Technik hat sich also für die Erkennung von Galaxienhaufen im Rotverschiebungsbereich $z > 0.8$ bewährt.

Die Entstehung und Entwicklung von massiven E und S0 Galaxien (Frühtyp Galaxien, ETGs) ist immernoch weitgehend ungeklärt, da die bevorzugte Standardtheorie für die Strukturentwicklung, "hierarchical structure formation", nicht vollständig mit den Beobachtungen konsistent ist. Mit Hilfe von sehr hoch aufgelösten Himmelsaufnahmen mit dem Hubble Space Telescope/ACS und mit VLT FORS2 Spektroskopie, konnte ich die Galaxienpopulation im Haufen XMMU J1229+0151 bei einer Rotverschiebung von $z = 0.975$ untersuchen, der im Rahmen des XDCP entdeckt wurde. Die Ergebnisse zeigen eine "red-sequence" im Farb-Helligkeitsdiagramm, die von Galaxien mit integrierten Sternmassen von 5×10^{10} - 2×10^{11} $M_{\odot}$ und Altern von 3-4 Gyr bevölkert wird. Diese "red-sequence" ist sebst bei dieser Rotverschiebung schon sehr eng (mit einer Streuung von 0.05 vergleichbar der des Coma Galaxienhaufens). Dies zeigt, das die E und S0 Galaxien schon sehr früh und innerhalb eines engen Zeitrahmens gebildet wurden. Ihre Sternbildung und die chemische Anreicherung des ICM wurde schon früh abgeschlossen, wie auch die hohe Metallizität (Häufigkeit schwerer Elemente) zeigt ($Z/Z_{\odot} \sim 0.3$), die mit Hilfe von *XMM-Newton* Spektroskopie in entfernten Haufen ermittlet wurde.

Abstract

In the framework of the current cosmological paradigm, cosmic evolution is mostly driven by gravity through the hierarchical growth of cold dark matter structures. However, the evolution of the directly observed luminous component involves complex non-gravitational processes such as cooling, star formation and feedback mechanisms involving the conventional matter well known to us, termed shortly as baryons. Clusters of galaxies are the largest virialized systems in the Universe, hence are ideal laboratories to study the evolution of baryons. The baryon content of clusters accounts for roughly 15% of their total mass, encompassing a "cold phase" in the form of luminous galaxy masses, and a "hot phase" corresponding to the X-ray emitting intracluster medium (ICM). The thermodynamics of baryons is affected by non-trivial phenomena and the interplay of the intricate processes between these two phases remains, to a large extent, unclear.

In this thesis I investigate the properties of both the ICM and the underlying galaxy populations in X-ray selected distant clusters, with the aim of constraining physical processes governing the evolution of clusters and their galaxies.

The inner regions of local clusters often exhibit radiative cooling, termed cool cores (CC). I have made an important step in investigating the abundance of cool cores in the distant cluster population, by devising efficient methods to characterize local CCs, that were applied to the highest redshift cluster sample currently available ($0.7 < z < 1.4$) from the *Chandra* archive. The fraction of CCs seems to decrease with redshift, since I find that the majority of the distant clusters are in an intermediate state of cooling.

High-z ($z \gtrsim 1$) clusters are hard to find. The XMM-Newton Distant Cluster Project (XDCP) is a survey aimed to construct a complete sample of $z \sim 1$ clusters from the *XMM-Newton* archive. Within this scope a large effort has been done to confirm potential distant cluster candidates by exploring a new optical & near-infrared imaging technique to identify overdensities of galaxies. Twenty-two cluster candidates were imaged during two runs at the ESO/La Silla Observatory, of which around half are potential distant clusters, based on their I-H images. The applied photometric technique has thus proven to be reliable in identifying $z \geq 0.8$ overdensities of galaxies.

The formation and evolution of massive early-type galaxies (ETGs) is still an open question, since the observational data cannot be easily reconciled with the preferred, hierarchical galaxy formation scenario. Using high-resolution *Hubble Space*

Abstract

Telescope/ACS imaging and VLT/FORS2 spectra, I studied the galaxy population of XMM1229 at z=0.975, discovered in the XDCP. The results show a red-sequence populated by galaxies with stellar masses in the range 5×10^{10} - 2×10^{11} $M_{\odot}$ and old (3-4 Gyr) underlying stellar population formed at $z_f \sim 4$. The color-magnitude relation at this high redshift is found to be already very tight (with a 0.04 spread similar to the local Coma cluster). This confirms that ETGs in clusters assembled early on and in short timescales, and their star formation processes have already completed the essential part of their chemical enrichment, as elucidated by the high metal abundance (Z $\sim$ 0.3 solar) of the ICM, measured with XMM spectra.

1

Introduction: scope of the thesis

This thesis is dedicated to the investigation of the total baryon content of X-ray selected distant clusters, both in their hot (intracluster gas) and cold (galaxies) phase. Even though there is yet no integrated picture of the history of cosmic baryons, it is indisputable that the processes of galaxy formation and evolution affect the properties of the ICM. How these mechanisms work remains an open question which, however, can be addressed by tracing the circulation of metals and the effect of heating processes, through the study of gas properties such as metallicity, temperature and entropy, linking them to the stellar mass content and star formation rates of the underlying galaxy populations.

In this perspective, this thesis is intended to contribute to the knowledge of the physical processes taking place in the high-z cluster population. The high-quality data - both in terms of high-resolution and large photon collecting power - provided by the X-ray observatories *Chandra* and *XMM-Newton*, and the optical *Hubble Space Telescope*, has been fundamental to probe high-redshift clusters with unprecedented detail, having allowed us to study the evolution of the intracluster medium (ICM) and the galaxy populations in distant clusters.

This dissertation comprises essentially three parts: (*i*) the analysis of a low- and a high-redshift cluster sample observed with *Chandra*, to address the evolution of cooling cores; (*ii*) the near-infrared (NIR) & optical follow-up of X-ray distant cluster candidates conducted in the framework of the survey XMM-Newton Distant Cluster Project (XDCP); and (*iii*) the study of the galaxy population in a rich cluster at $z \sim 1$ detected in the XDCP, using high-resolution ACS/HST optical imaging and

spectroscopy.

The thesis begins with an introduction to the underlying theoretical framework of large-scale structure formation in which galaxy clusters are embedded, as well as a review of the main observational X-ray properties of the ICM (Chapter 2), that is intended to provide a foundation and motivation to the first (Chapter 4) and second (Chapter 5) parts of this work. A brief account on galaxy evolution is also provided, from theory to the state-of-art observations of galaxies in dense environments (Chapter 3), which is suited to frame the work on the second and third (Chapter 6) parts of the thesis.

Cool core clusters (or "cooling flows" as they were termed originally) were discovered in 1977 by Fabian & Nulsen (1977) and Cowie & Binney (1977), and have since then been the subject of intense investigation and debate (see Fabian et al. (1984), Fabian et al. (1994) for detailed reviews). The lack of detection of very cold gas or intense star formation in cluster cores have shown that the predicted rate of radiative cooling is not confirmed by observations of galaxy clusters. Indeed, the X-ray analysis of the temperature and cooling time profiles confirmed that cool cores (CCs) are missing the colder phases expected from steady state cooling (e.g. Peterson et al. (2001, 2003)), motivating scenarios where a heating source counteracts the cooling. Although several accounts on the abundance and characterization of the local cool core population have been published, pointing to a fraction of CCs ranging from 50 to 70% (Peres et al. (1998), Chen et al. (2007)); only one preliminary study on the fraction of CCs at high-redshift has been presented so far (Vikhlinin et al. (2007)). This situation is mostly due to the low photon statistics characteristic of high-redshift data, preventing the application of spectroscopic techniques to measure the temperature distribution in cluster cores, which is the best estimator of cooling.

In the first part of this thesis (Chapter 4) we investigate the abundance of cool core clusters in a statistically complete sample with redshift $0.7 < z < 1.4$ - the most distant sample compiled from the *Chandra* archive at present. To understand how to characterize cool cores in a robust way we start by defining criteria to classify and quantify cool cores in a morphologically diverse sample of nearby clusters ($0.15 < z < 0.3$). The analysis undertaken is based essentially on the surface brightness properties of the clusters. Initially we obtained azymuthally averaged surface brightness profiles, which were then fitted with single and double beta models. At low-z this is a good strategy to single-out cool cores, as they require a 2-component model to properly describe the center SB excess. This is not so straightforward for the high-z sample which suffers from poor photon statistics (Ota & Mitsuda (2004), Ettori et al. (2004)). Therefore we defined a simple, yet robust parameter based on the surface brightness concentration of the clusters, c_{SB}, with which we made

an initial classification of the low-z clusters with the purpose of calibrating the c_{SB} method, since there is published information on the CC properties of these clusters. To port this parameter to high-z we developed the cloning technique, a practical and powerful method to construct mock clusters with a given distribution of realistic physical morphologies, assuming no intrinsic cluster evolution. We cloned the low-z sample to the redshifts and cluster counts of the high-z sample and measured the c_{SB} parameter in the simulated clusters. The constancy of the results obtained for parameter validates its application to high-z. We, therefore, obtained a phenomenological method to quantify cooling both in the local and distant samples. To strengthen this result we coupled the c_{SB} information with the SB profiles, scaling them according to the empirical scaling relations (Arnaud & Evrard (1999)). Our results indicate three categories of CCs in the low-z sample: non-CC, moderate and strong; whereas the distant sample covers only the first two. Additionally to the SB analysis we also measured the clusters cooling time, as this is a more physical method to probe radiative cooling. We find good agreement in the results obtained with the two methods and we conclude that the majority of the distant clusters do show signs of moderate cooling at their centers, although no strong cool core was found. This result favors a picture of the high-z population in which clusters are in an intermediate cooling state, which is plausible within the current hierarchical scenario of structure formation. Most of the content of this chapter has been published in A&A (Santos et al. (2008)).

To further emphasize the potential and usefulness of the cloning technique as a powerful tool to simulate realistic clusters, we present in Appendix the test case of simulating an eROSITA (Predehl et al. (2006)) survey field, based on the *XMM-Newton* point source catalog of COSMOS, adding *Chandra* low-z clusters cloned to redshifts 0.7-1.3. With this exercise we investigate the capability of eROSITA to detect distant clusters with different morphologies.

In Chapter 5 I introduce the XMM-Newton Distant Cluster Program and present my contribution to this project. The XDCP (Böhringer et al. (2005)) explores the *XMM-Newton* archive with the purpose of constructing a statistically significant sample of distant clusters (z$\sim$1) to characterize the cluster population at high-redshift, intending as well to constrain cosmological parameters. First results of the survey include the discovery of the massive distant clusters XMMUJ2235.3-2557 at z=1.393 (Mullis et al. (2005); XMMUJ1229+0151 at z=0.975 (Chapter 6 of this thesis) and XMMUJ0104.4-0630 at z=0.947 (Fassbender et al. (2008)).

The first step to confirm cluster candidates is to search for galaxy overdensities with inexpensive imaging. To this end, an extensive program of follow-up observations in the optical and NIR was undertaken during this thesis in the 4 m-class telescopes at the Calar Alto observatory (Spain) and at the ESO/La Silla observatory (Chile),

in addition to VLT snapshot imaging. The redshift regime we are targeting implies the need to use the reddest combination of filters, as the galaxies we are seeking are old and passively evolving. We explore a new two-band imaging strategy, the I-H method, which has a potentially high performance for high-redshift objects. A total of 22 cluster candidates have been observed in the I- and H-bands during two observing runs at ESO/La Silla in 2007, for which we present the photometric analysis. The I-H color images immediately give a first order evaluation of the quality (and existence) of galaxy overdensities and provide and estimate of the redshift, being the first filtering process to decide whether to continue with the spectroscopic follow-up. We conclude that about 12 candidates are potential distant clusters. In addition, we also construct the color-magnitude relation (CMR) of one of the richest high-z candidates observed, cluster 165. The color-magnitude relation relies on the observation that the colors of early-type galaxies correlate with their absolute magnitudes (see, e.g., Baum (1959)), and has become one of the most common tools used to constrain the epoch of formation and the star formation history of these systems (Bower et al. (1992)). The CMR of target 165 shows a clear Red-Sequence ((Gladders & Yee (2000))), and according to simple stellar population models (see Fassbender (2008), Fig. 7.1), we infer that this is likely a cluster of redshift $z \gtrsim 0.8$. This target has already been awarded spectroscopic observations. The XDCP has thus proven to be a valuable source of distant clusters. The full photometric data analysis is ongoing and we can expect the discovery of more distant clusters within the next 1-2 years.

At redshift $\sim$1 only a handful of X-ray selected clusters have been analyzed in detail with high-quality data (Blakeslee et al. (2003, 2006); Mei et al. (2008) submitted to ApJ; Holden et al. (2005), Demarco et al. (2007), Rosati et al. (2008) in prep., Lidman et al. (2004, 2008)).

The outcome of the global analysis of these datasets indicates a consistent picture of the high-z galaxy population in clusters, in which early-type galaxies are already in an advanced stage of passive evolution, having formed rather early, at z$>$ 2. To confirm such results and thus place strong constraints on galaxy evolution scenarios, we need to increase the statistics on the studies of high-z galaxies in clusters.

Within this context, the last part of this thesis (Chapter 6) is dedicated to the study of the galaxy properties of a massive cluster at redshift z=0.975, discovered in the XDCP. We probed the ICM with the discovery *XMM-Newton* data, which revealed a hot (T=6.5 keV), luminous cluster (L_X0.5-2.0]keV = 3.2 10^{44} erg/s), with a metallicity of $Z/Z\odot \sim 0.34 \pm 0.13$. Using high-resolution HST/ACS images combined with optical ground based spectroscopy (VLT/FORS2) and NIR imaging (NTT/SOFI) we constructed the color-magnitude relation of $\sim$20 confirmed cluster members and additional 36 galaxies $i_{775} - z_{850}$ color selected located in the red-sequence. The $i_{775} - z_{850}$ CMR parameters, zero point ZP=0.829$\pm$0.041 and slope = -0.031$\pm$0.016,

are consistent with results on other clusters at high-redshift (see Mei et al. (2008) for a recent review on the analysis of 8 clusters observed with HST/ACS). A tight red-sequence is already in place, characterized by a small scatter of 0.042±0.011 mag. A structural analysis of all the red-sequence galaxies was carried out by fitting Sersic models and via a visual morphological classification (Postman et al. (2005)). We find a good agreement between the structural parameters effective radius (R_e) and Sersic index n with the spectral type. The bulk of the red-sequence is clearly dominated by elliptical galaxies (15/21 cluster members and 32/36 color-selected galaxies), with a fraction of S0's of only 4 out of 21 cluster members. The stellar content of the confirmed early-type galaxies is investigated by fitting synthetic stellar population models (Bruzual & Charlot (2003)) to the galaxies' spectral energy distributions (SEDs), in order to constrain star formation histories, stellar masses and formation ages. We find that the population of confirmed early-type galaxies is moderately massive (with stellar masses of the order of 7.10^{10} $M_\odot$), and rather old (3-4 Gyr), having formed at $z_f \sim 3-4$. These results indicate that star formation activity is likely to have ended, having allowed ETGs to enrich the ICM with metals, which is in agreement with the high metallicity of the ICM.

2

Galaxy clusters from an X-ray perspective

Abstract

This Chapter outlines the general theory of cluster formation and evolution based on the hierarchical scenario of structure formation, and focuses on X-ray observations of clusters. The properties of the intracluster medium are described, along with the observationally derived scaling relations. Furthermore, the yet unsolved "cooling flow problem" is discussed, since this is related to a major part of this thesis (see Chapter 4). An overview of current and upcoming X-ray surveys is presented, as this is the most powerful method to hunt for z$\geq$1 galaxy clusters. Finally, clusters are introduced as important cosmological probes suitable to constrain cosmological parameters.

2.1 Theoretical framework on cluster formation

The current cosmological Λ cold dark matter (ΛCDM) paradigm postulates a flat, low-density Universe, characterized by the following parameters: matter density $\Omega_m = 0.233 \pm 0.013$, dark energy density $\Omega_\Lambda = 0.721 \pm 0.015$, amplitude of fluctuations $\sigma_8 = 0.817 \pm 0.026$ and the present-day Hubble constant h=73 (up-to-date values taken from cosmic microwave background (CMB) WMAP data combined with the distance measurements from the Type Ia supernovae (SN) and the Baryon Acoustic Oscillations data, Komatsu et al. (2008)). In this so-called Concordance Cosmological model, quantum density perturbations formed in the early Universe grow through

gravitational interaction. The statistical properties of the primordial density perturbations can be described by their power spectrum, $P(k) \propto k^n T^2(k)$, where k is a comoving wavenumber, n is the spectral index, and T(k) is the transfer function which depends both on the cosmological parameters and on the cosmic matter constituents (see Kolb & Turner (1990)).

According to the hierarchical scenario of structure formation (Peebles (1993), Coles & Lucchin (1995), Peacock (1999)), clusters of galaxies form via the gravitational collapse of rare high density peaks of the initial density fluctuations, having a typical comoving scale of about $10h^{-1}$Mpc. The statistics on these large virialized objects can be described by a simple analytical formalism developed by Press & Schechter (1974).

Dark matter (DM) is the dominant form of matter in the Universe, and even if its nature remains obscure, the existence of DM has been established more than 70 years ago by F. Zwicky (Zwicky (1937)). High-resolution N-body simulations based on the hierarchical model indicate a universal dark matter halo density profile (Navarro et al. (1996, 1997)):

$$\rho_{DM}(r) = \frac{\rho_s}{\frac{r}{r_s}(1+\frac{r}{r_s})^2} \tag{2.1}$$

where r_s is a characteristic scale length and $\rho_s = \delta_c \rho_c$ is a characteristic density (see Sect. 2.1.1 for the definition of ρ_c).

Clusters are the most massive, gravitationally bound systems in the Universe, and therefore the last objects to develop and virialize. They are located at the intersections of filaments in the cosmic web, continuously accreting material from infalling groups/galaxies, and thus do not have a definite, clear-cut boundary. The non-linear evolution of density perturbations can be approximated by the spherical top-hat model, in which a cluster is considered as a spherical perturbation which has just collapsed. With this simplistic model, the formation and evolution of virialized DM halos can be well described.

2.1.1 The self-similar model

The overall dynamics of clusters is dominated by dark matter, which is subject only to gravity. Considering a purely gravitational scenario and assuming that gas follows the dark matter collapse, clusters are expected to form a regular population, hence a self-similar model (Kaiser (1986)) emerged to characterize clusters in a simple and convenient way. In the spherical collapse model, a cluster has the well defined boundary corresponding to $\Delta = 18\pi^2 \sim 200$, where Δ is defined as the density contrast with respect to the critical density of the Universe at the cluster redshift, $\rho_c \equiv 3H^2(z)/8\pi G$. In reality, the cluster mass is not a well-defined quantity in the sense

that clusters are not closed spheres, however, it is convenient to define it as the mass enclosed in a radius corresponding to a fixed Δ, with respect to ρ_c:

$$M_\Delta = M(< r_\Delta): \quad \frac{M_\Delta}{4/3\,\pi\, r_\Delta^3} = \Delta \times \rho_c. \tag{2.2}$$

In hydrostatic equilibrium the gas mass enclosed within the virial region is connected to the cluster global temperature via

$$\frac{G\mu m_p M_V}{2R_V} = \beta_T kT. \tag{2.3}$$

Even though the self-similar model has been well supported with N-body simulations and semi-analytical modelling, complex non-gravitational physical processes may cause deviations from the predictions derived by self-similarity as is the case in cool core clusters (see Sect. 2.2.1), particularly in the lower mass systems.

2.2 Properties of the Intracluster Medium

In the process of virialization, galaxy clusters undergo adiabatic compression and shocks (generated by supersonic motion), thus providing the primordial heat to the intracluster medium (ICM), a hot gas ($\sim 10^7$ K) confined by the cluster's gravitational potential well. Clusters are permeated by this low-density and optically-thin plasma, which strongly emitts X-ray radiation through thermal Bremsstrahlung processes and metal emission lines (see for e.g. Sarazin (1988)), proportional to the square of the gas density. The Bremsstrahlung emissivity of a plasma at temperature T is given by:

$$\begin{aligned} \epsilon_\nu &\equiv \frac{dL}{dV d\nu} \\ \epsilon_\nu &= \frac{2^4 e^6}{3 m_e \hbar c^2}\left(\frac{2\pi k_B T}{m_e c^2}\right)^{1/2} \mu_e n_e^2 g(Z,T,\nu) exp\left(\frac{h_P \nu}{k_B T}\right)(k_B T)^{-1} \end{aligned} \tag{2.4}$$

where ν is the frequency, Z and e are, respectively, the iron and electron charges, m_e is the electron mass, n_e is the electron number density, μ is the mean molecular weight, h_P and k_B are the Planck and Boltzmann constants, respectively, and $g(Z,T,\nu) \sim 1$ is the Gaunt factor.

The ICM is the major baryonic component in clusters, with a fraction that increases with the total cluster mass, and is, for massive clusters, on average ~ 5 times larger than the stellar baryon fraction. Therefore, X-ray observations of galaxy clusters are extremely valuable to assess the bulk of the cluster baryonic mass. The intracluster gas undergoes metal enrichment by supernovae - a clear sign of star formation in cluster galaxies - resulting in a typical metal abundance of 1/3 solar, in local clusters.

The most prominent signature of the metal enrichment is the iron K-line complex at 6.7 keV.

- Gas temperature

  The gas temperature is derived by fitting the observed spectrum with a thermal emission model, convolved with the instrument response. Massive clusters typically have T> 3 keV (below 3 keV are considered poor clusters or groups of galaxies). Temperature profiles obey self-similarity and are powerful probes that indicate the state of the gas in the core. Although temperature profiles of cool cores (CCs, see Sect. 2.2.1) are steeper in the central region with respect to non-CCs, a bimodality CC/non-CC cannot be claimed in representative samples as the XMM-LP (Böhringer et al. (2007)), where there is a gradual transition between the two extremes - see Fig. 2.1 where the radial temperature profile of each cluster was normalized by a global temperature, T_X, which should be representative of the virial temperature of the cluster. The spectroscopic temperature was measured within the region 0.1 R_{200} < r < 0.4 R_{200}, which was estimated in an iterative fashion, using the R_{200} T relation of Arnaud (2005) (see Sect. 2.2.2 for an introduction to the X-ray scaling relations).

- Surface brightness and gas density

  Assuming the physically-motivated hypotheses of hydrostatic equilibrium and spherical symmetry, we can describe the X-ray surface brightness with the isothermal β model by Cavaliere & Fusco-Femiano (1976):

  $$S(r) \propto (1 + (r/r_c)^2)^{-3\beta+0.5} \tag{2.5}$$

  where r_c and β are the core radius and slope, respectively. This model offers a generally good description of the observed profiles, with a typical value of β=2/3. Density radial profiles are obtained by deprojection of the surface brightness profiles along the line-of-sight:

  $$S_X(R) \propto \int_R^\infty n_e^2 dl \tag{2.6}$$

  where n_e is the electron density and R is the enclosed radius. In Fig. 2.2, the scaled density profiles of the XMM-LP sample are shown. Similarly to the temperature profiles, the density profiles smoothly populate the transition between CCs (center excess emission) and non-CC (flat profiles in the inner regions).

- Gas entropy

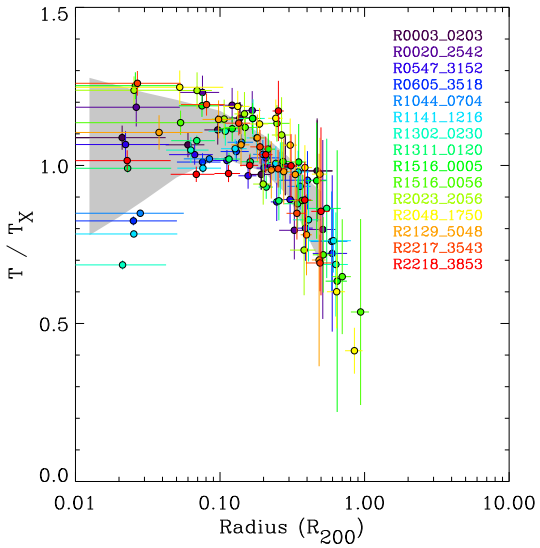

Figure 2.1: Scaled projected temperature profiles of 15 clusters from the XMM-LP sample, obtained with XMM-Newton observations from Pratt et al. (2007). The profiles have been normalized to the mean spectroscopic temperature in the 0.1 R_{200} $\leq$ r $\leq$ 0.4 R_{200} region, where R_{200} was determined iteratively using the RT relation of Arnaud et al. (2005). The shaded grey area corresponds to the region enclosed by the mean plus/minus the 1σ standard deviation.

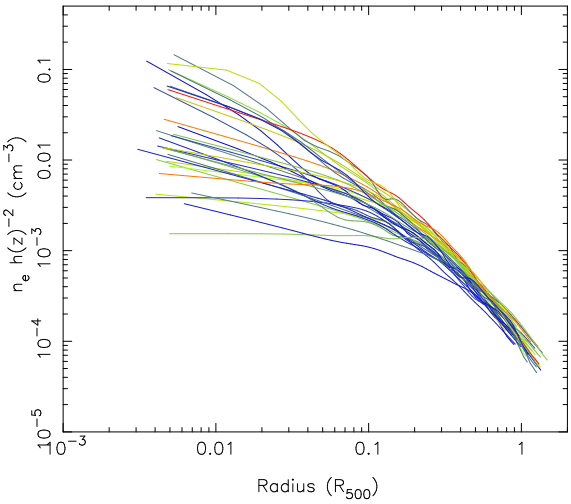

Figure 2.2: Scaled density profiles of the XMM-LP sample obtained from XMM-Newton observations from Croston et al. (2008).

The observed gas entropy results from shock heating of the gas during cluster formation and scales with the cluster temperature. The thermodynamic history of the ICM is strongly tied to the specific entropy K

$$K = T n_e^{-2/3} \tag{2.7}$$

since K always increases when heating takes places and always decreases when radiative cooling is dominant, thus preserving a record of the cooling and heating processes in the ICM. We note that K differs from S, the classical definition of entropy in thermodynamics, however these two quantities are related by $S \propto lnK + const.$

2.2.1 Complex physics in clusters cores: the "cooling flow problem"

Early X-ray observations revealed that a large fraction of clusters presented a bright central peak in their surface brightness, suggesting that the ICM in the clusters cores was considerably affected by radiative cooling, thus forming a "cooling flow" (Cowie & Binney (1977), Fabian & Nulsen (1977)). Further evidence gathered through the analysis of X-ray spectra, that indicated a temperature decrease towards the central region which, in addition to observations of the gas density, implied that the radiative cooling time of the gas was less than the Hubble time. These observations led to the formulation of a simple model for cooling flows, assuming that the observed X-ray emission is of thermal nature, and the cool core (CC) does not mix with the outer ICM, cooling radiatively. Furthermore - and here is where the model seems to fail - no source of heating is supposed to balance the cooling, therefore, the gas should be able to cool to very low temperatures. The absence of observational evidence for such cold cores is what became known as the "cooling flow problem". Indeed, the central temperature of cooling flows remains at a factor $\sim$1/3 of the overall cluster temperature (Peterson et al. (2003); Bauer et al. (2005)), and the mass deposition rates are much smaller than expected (Edge & Frayer (2003)). Therefore some form of heating must balance cooling, in a way that explains the similarity of, for e.g., the cooling time profiles of clusters. The most likely heating source is a central black hole, since its powerful jets can create bubble-like cavities in the ICM, as has already been observed (see review by Peterson & Fabian (2006)).

In the local Universe, extensive work has been done in investigating the abundance of cool cores, which is found to be of the order of 50-70 % (e.g., Peres et al. (1998); Chen et al. (2007)). At intermediate redshift ($z \lesssim 0.4$) no significant evolution has been found (Bauer et al. (2005)), however at further higher redshift ($0.5<z<0.9$) there has been a recent claim for strong evolution of cool cores (Vikhlinin et al. (2007)). The evolution of the number density of cool cores, particularly at high-redshift ($z \geq 1$), gives us insight on the physical processes affecting the cluster popu-

lation. A significant part of this thesis (Chapt. 4) is dedicated to study the fraction of cool cores at 0.7<z<1.4.

2.2.2 Scaling Relations

Due to the generally observed approximate self-similarity of the shapes and structures of clusters, one finds that global cluster properties scale with cluster mas. Observationally, the ICM temperature is found to be a good proxy for cluster mass, thus it is not surprising to find that the physical properties of the intracluster gas can be linked to its temperature via the scaling relations. These are simple, observationally derived power-law relations that underlie the general regularity of the cluster population. Scaling relations are essential for establishing a link with the cluster mass (which is not directly measurable from X-rays) since, in hydrostatic equilibrium, the gas temperature is a good proxy for the cluster total mass (see Eq. 2.3). In Table 2.1 we provide a summary of the scaling relations for nearby clusters as compiled by Arnaud (2005).

Table 2.1: Scaling relations from Arnaud (2005)

Relation	**Slope**	**Reference**
L_X-T	2.64±0.27	Markevitch, 1998, ApJ, 504, 27
	2.88±0.15	Arnaud & Evrard, 1999
M_{gas}-T	1.98±0.18	Mohr, Mathiesen & Evrard 1999
	1.71±0.13	Vikhlinin, Forman & Jones 1999
	1.89±0.20	Ettori, De Grandi & Molendi 2002
	1.80±0.16	Castillo-Morales & Schindler 2003
EM-T	1.38	Neumann & Arnaud 2001
S-T	0.65±0.05	Ponman, Sanderson & Finoguenov 2003
f_{gas}-T	0.34±0.22	Mohr, Mathiesen & Evrard 1999
	0.66±0.34	Ettori, De Grandi & Molendi 2002
R_{500}-T	0.5±0.05	Arnaud, Pointecouteau & Pratt 2005
L_X-M_{200}	1.81±0.08	Reiprich & Boehringer 2002

Deviations from self similarity have been observed, giving rise to an empirical L-T relation (Edge & Stewart (1991); Markevitch (1998); Arnaud & Evrard (1999)), where $L \propto T^{2.88}$. The nature of this scatter is likely non-gravitational, since it is established that CCs contribute significantly to the scatter in the L-T relation (e.g. Markevitch (1998)).

2.2.3 Cluster mass determination

The most reliable assessment of the mass distribution in clusters is obtained by solving the hydrostatic equation, knowing the X-ray gas density and temperature profiles. Currently there are three main methods to estimate the cluster mass through the scaling relations:

- gas temperature: direct application of the M-T relation (see Table 2.1)
- gas mass: in the ideal case in which all cluster baryons are in the ICM, and assuming that the baryonic fraction in clusters is representative of the cosmic value, the total mass is given simply by

$$M_{tot} = f_g^{-1} M_{gas}, \tag{2.8}$$

  where M_{gas} is provided by the X-ray data, and f_g, to the first approximation, equals Ω_b/Ω_m, the ratio which is accurately given by the CMB measurements (Spergel et al. (2007)). To estimate the mass corresponding to a given critical overdensity, we solve

$$\frac{M_{gas}(r)\, f_g^{-1}}{4/3\,\pi\, r^3\, \rho_c(z)} = \Delta \tag{2.9}$$

  to find the corresponding overdensity radius, r_Δ. Equation (2.8) with M_{gas} evaluated at r_Δ is then used to find M_{tot}.
- the quantity Y_X defined as $Y_X = T_X \times M_{\mathrm{gas},X}$, where T_X is the temperature derived from fitting the cluster X-ray spectrum integrated within projected radii, and $M_{\mathrm{gas},X}$ is the hot gas mass within the virial radius of the sphere. See Fig. 2.4 for a recent determination of the cluster mass function obtained with this method.

2.2.4 Evolutionary trends of cluster properties

All scaling relations evolve with redshift via the cosmological factor $h(z)$, defined as the Hubble constant normalized to its current value, $H_z/H_0 = \sqrt{\Omega_m(1+z)^3 + \Omega_\Lambda}$. This factor represents the evolution of the critical density of the universe, ρ_{crit}. Hence, all the relations compiled in Table 2.1 are applicable to high-z, provided the appropriate $h(z)^\alpha$ factor is introduced. In particular, the self-similar model predicts that clusters become denser, smaller and more luminous. From the M-T relation one obtains $L_X \propto h(z)T^2$, and as the $h(z)$ factor increases with redshift, it is straightforward that clusters should appear more luminous with increasing redshift. Conversely, the redshift evolution of the fiducial radius R_{500} is inversely proportional to $h(z)$, resulting in distant clusters appearing more compact. For instance, a local (z=0)

cluster with T=5 keV has R_{500}=1253 kpc, whereas at z=1.0 a cluster with the same temperature has R_{500}=711 kpc.

Concerning the chemical enrichment of the ICM, recent studies using *Chandra* archival data have confirmed a decrease of the metal abundance with redshift, down to a factor ∼2 at z=1.2, relative to the local value (Balestra et al. (2007)). Still, the ICM is already significantly enriched ($Z_{Fe} \sim 0.25 Z_o$) at a look-back time of 9 Gyr. This result, at such a high-redshift, provides significant constraints on the timescales and physical processes which drive the chemical enrichment of the ICM.

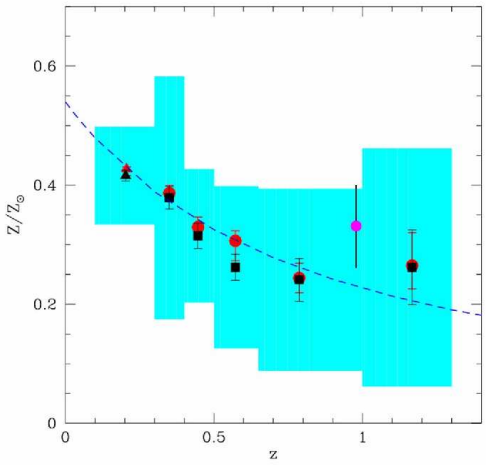

Figure 2.3: Evolution of the iron abundance in galaxy clusters from Balestra et al. (2007). The plot shows mean $Z/Z_\odot$ fraction in a sample of 56 clusters spanning the redshift range [0.2-1.2], binned in 5 redshift bins. The dashed line indicates the best fit over 6 redshift bins for a simple power law of the form $Z = Z_0(1+z)^{-1.25}$. The magenta dot at z=0.976 refers to the metallicity of cluster XMMU J1229+0151 analyzed in Chapter 6.

Using *Chandra* observations of statistically complete samples of low and high-z clusters drawn from the 400 deg^2 sample (Burenin et al. (2007)), Vikhlinin et al. (2008) have recently measured the evolution of the galaxy cluster mass functions up to z=0.5. These authors claim an evolution in the cluster comoving number density of a factor of ≈ 5 at $M_{500} = 2.5 \times 10^{14}\, h^{-1}\, M_\odot$ between $z = 0$ and 0.5 (see Fig. 2.4), which is expected in the ΛCDM model.

Although numerical simulations indicate a cluster merger rate almost twice higher at z>0.7 (Cohn & White (2005)) relative to local clusters, *Chandra* and *XMM-Newton* observations of distant clusters up to the current redshift limit z=1.45 (Stanford et al. (2006)) indicate that the high-z cluster population still displays a quasi-relaxed state where the gas is thermalized.

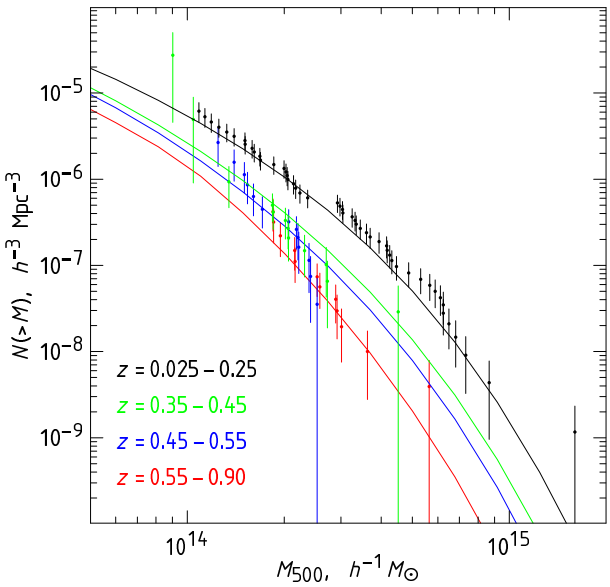

Figure 2.4: Cluster mass functions for the low and high-z samples from Vikhlinin et al. (2008). The masses were estimated by the Y_X method. The errorbars show the Poisson uncertainties. Solid lines show the model predictions in the standard cosmological model, with only σ_8 fit to the cluster data.

2.3 X-ray cluster surveys

Massive high-redshift clusters are optimally selected in X-rays since the emission of the intracluster medium peaks in the energy range [0.5-2.0]keV. This is a rather clean way of detecting clusters, not subject to projection effects along the line of sight which one frequently encounters in optical searches. The ROSAT (Truemper (1992)) mission was a milestone in systematically detecting a large number of galaxy clusters. The local REFLEX sample (∼500 clusters, Böhringer et al. (2004)), the 400 deg^2 sample (Burenin et al. (2007)) and the RDCS distant cluster sample (Rosati et al. (1998)) are some examples of prolific cluster samples based on the ROSAT mission.

The advent of major X-ray observatories as the *XMM-Newton*, *Chandra* and *Suzaku* has dramatically increased the quality and degree of detail to which we now trace the hot gas in clusters. At high-redshift, however, we are still striving for large cluster statistics with good angular resolution. To reach this goal, several cluster surveys based on the *XMM-Newton* data are ongoing, such as the XDCP (Böhringer et al. (2005)), a project in which I am involved and that will be discussed in Chapter 5; the XMM-LSS (Pierre et al. (2006)); the XCS (Romer et al. (2001)) and COSMOS (Scoville et al. (2007)).

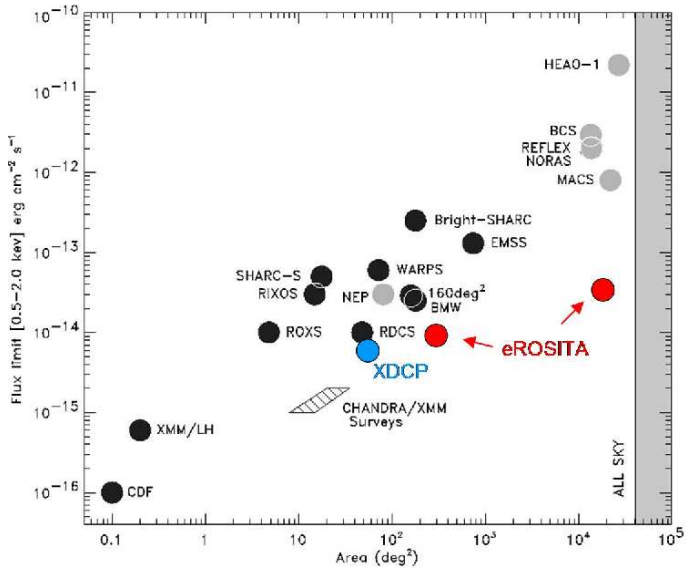

Figure 2.5: From Rosati et al. (2002), the XDCP point is taken from Fassbender (2008) and the eROSITA points are from G. Hasinger.

The main upcoming X-ray cluster survey is eROSITA (extended ROentgen survey with an Imaging Telescope Array, Predehl et al. (2006)) which has been already approved and is due to be launched in 2011. This mission is essentially dedicated to study the nature of dark matter and dark energy, by tracing the evolution of the cluster abundance with a sample of 50 000 - 100 000 clusters (Predehl et al. (2006))

Initial surveys designed to fullfill this aim included a (*i*) wide survey with a flux limit (0.5-4 keV) $\sim 3.10^{-14}$ erg s^{-1} cm^{-2} over 20 000 deg^2 during 3 years resulting in the discovery of 50 - 100 000 clusters, and (*ii*) deep survey with a flux limit $\sim 8.10^{-15}$ erg s^{-1} cm^{-2} over 200 deg^2 during 1/2 year, yielding about 6500 clusters, of which 200-300 at z>1. A new concept is currently being envisioned, based on continuous scanning with deeper exposures of the poles.

IXO is the most recent next generation X-ray observatory, which has been selected as a candidate large-class mission as part of ESA's Cosmic Vision 2015-2025 programme. The IXO concept is a joint effort of ESA, JAXA, and NASA and is expected for the Cosmic Vision downselection at the end of 2009/11. Even if this will not be a prime survey instrument, IXO should have the capability to obtain detailed cluster spectra up to z=2. Current science cases to be investigated include the evolution of black hole accretion and its relationship to galaxy formation, the growth and evolution of large scale structure, matter under extreme physical conditions around black holes and neutron stars and dynamics and chemistry of cosmic plasmas.

The solid angles and flux limits of the main past, present and upcoming surveys is shown in Fig. 2.5.

2.4 Clusters in a cosmological framework

In addition to being interesting astrophysical objects *per se*, galaxy clusters are also non-linear tracers of the large-scale structure, making them powerful tools to constrain the cosmological parameters Ω_m, σ_8 and to a lesser degree, Ω_Λ.

Several methodologies based on X-ray observations of clusters are available to constrain cosmological parameters, the most robust being:

- The **mass function of local clusters**, $n(M)$, can constrain the amplitude of the power spectrum, σ_8, and the matter density, Ω_m, at the cluster scale, through the comparison of the theoretical mass function (Jenkins et al. (2001)) with the observed X-ray luminosity function (XLF) (see for e.g., Böhringer et al. (2002)).

- Considering that the **baryon mass fraction f_b of clusters** is representative of the relative matter content of the Universe, and since the baryon density of the Universe Ω_b is known from the Big Bang Nucleosynthesis calculations or the CMB, the matter density can be constrained assuming Ω_m=Ω_b/f_b (e.g. White & Frenk (1991), see Vikhlinin et al. (2003) for more recent results)

- The **gas mass fraction in clusters**,f_{gas}, should be constant and a measure of the Universe's value. Therefore measurements of its apparent evolution ($f_{gas}(z) \propto d^{1.5}$) can used to probe the acceleration of the Universe, hence constraining Ω_Λ (Allen et al. (2008)).

- The **evolution of the cluster mass function** reflects the growth of density perturbations and can be used to constrain Ω_Λ, in addition to Ω_m and σ_8. This test requires a sample of clusters covering a large redshift range, for which the survey volume is well known. The application of the scaling relations to derive the X-ray temperature function (XTF) or the XLF (Mullis et al. (2004)) offer proxies to estimate the total mass, which are then compared to the $n(M, z)$.

- The **clustering properties of clusters** described by means of the power spectrum $P(k)$, can be used as a measure of the large scale-structure of the Universe, allowing us to constrain the cosmological parameters Ω_m, σ_8 (Schuecker et al. (2001, 2003a,b)) .

In this era of precision cosmology it is essential to obtain Ω_m and σ_8 with different methodologies in order to break degeneracies between these parameters. In this respect, clusters offer a valuable means to test cosmological models, complementary

to other observational probes such as the CMB (Spergel et al. (2007)) and SN Ia (Riess et al. (2004), Astier et al. (2006)), and are more competitive than weak lensing studies. However, cosmological parameters derived with clusters still have error bars larger than desired. This situation arises because clusters are not perfect standard candles as deviations have been observed in the scaling laws that provide the link with the total cluster mass. The nature of the scatter is under intense investigation, in order to decrease the uncertainties in the measurements of cosmological parameters derived with clusters. The future looks bright though, with eROSITA coming online in the next three years, the statistics of clusters will dramatically increase, improving the measurements of Ω_m and σ_8, in addition to constrain Ω_Λ.

3
Galaxy evolution in clusters

Abstract

This Chapter introduces the two main galaxy formation scenarios, the *monolithic* and the *hierarchical* models. A final consensus has not yet been reached between these contradictory hypotheses, thus motivating studies on the evolution of massive galaxies.

The properties of early-type galaxies are described with several methodologies: (*i*) via a morphological characterization; (*ii*) through the analysis of the color-magnitude relation, (*iii*) and by modelling the galaxies' spectral energy distributions or spectra.

To end this section we summarize the most recent results obtained with studies of galaxies in clusters at redshift $\gtrsim 1$.

3.1 Galaxy formation scenarios

Two conflicting scenarios of galaxy formation and evolution have been proposed over 30 years ago: the *monolithic collapse model* (Eggen et al. (1962); Larson (1974), Arimoto & Yoshii (1987)), in which massive galaxies result from a single burst of star formation at high redshift; and the *hierarchical merging model* (Toomre (1977), White & Rees (1978)), in which galaxies are formed by accretion of smaller proto-galaxies.

Early-type galaxies (ETGs) form a homogeneous class of massive, red and passively evolving galaxies, characterized by absorption-line spectra and negligible (if

any) emission lines. ETGs also contribute to most of the total stellar mass in clusters (∼60%), therefore the study of their evolution is essential to investigate galaxy formation and evolution.

In the current paradigm of the ΛCDM cosmology, large galaxies assembled over time through the accretion of smaller low-mass progenitors, thus favoring the *hierarchical* scenario. However, this picture apparently is at odds with the observation that (*i*) early-type galaxies are found to be the most massive *and* oldest systems, and (*ii*) their star formation histories indicate that the bulk of the stars in massive ellipticals formed at redshift z> 2 (van Dokkum (2005), Tran et al. (2005)), which is in contradiction with the predictions from the the ΛCDM model.

The physical processes involved in galaxy formation and evolution are numerous and complex, such as radiative cooling, AGN and supernova feedback, and star formation. Figure 3.1 taken from De Lucia et al. (2004), illustrates the complex interplay of processes affecting the state of the baryons in clusters. It is reasonable to say that we have not yet reached a full understanding of these intricate mechanisms in spite of major observational work and a large effort in developing semi-analytical models (SAM), which, when coupled to N-body simulations, provide a means to tackle these phenomena. Although simulations have for a long time overestimated the fraction of blue galaxies, the introduction of a heating mechanism in the form of AGN feedback has prevented the overproduction of stars. In this way, simulations have succeeded in predicting a large amount of massive old galaxies, thus providing a good match to the observations (De Lucia et al. (2004), Bower et al. (1992), Menci et al. (2006)).

Observations of metal abundances in the intracluster medium are one of the best means to place constraints on the star formation history in clusters - a measure of the efficiency with which gas was converted into stars, in addition to providing information on the processes responsible for the circulation of metals.

3.2 Structural properties of ETGs

The first classification scheme of galaxies (Hubble (1936)) was based on their visual morphological characteristics. Galaxies were broadly divided in ellipticals (bulge dominated), spirals (showing spiral arms), lenticulars or S0s (bulge with a disk), and irregulars (absence of any regular geometry). Even though such a simplistic sorting of galaxies is prone to uncertainties that cannot be easily accounted for, morphology does correlate with the stellar content of a galaxy, providing valuable information on the internal conditions of the galaxies. In fact, a visual classification based on HST imaging of seven clusters with $0.83 < z < 1.27$ published in Postman et al. (2005) has become a reference for classifying high-z galaxies.

The surface brightness of galaxies is generally well described by the combination of a bulge component and an exponential disk. The Sersic law (Sersic (1968)) is

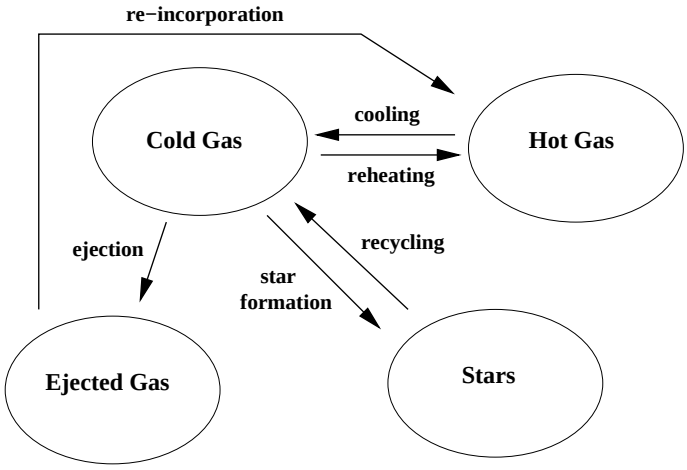

Figure 3.1: From De Lucia et al. (2004), Schematic representation of how mass is exchanged between the different phases considered in their semi-analytical models in the absence of accretion from outside. Metals follow the same routes as the mass.

commonly used to model bulges and can be described as:

$$\Sigma(r) \propto exp(r/r_e)^{1/n} - 1 \tag{3.1}$$

where $\Sigma(r)$ is the surface brightness at radius r. The most relevant parameters that characterize the shape of a galaxy are the effective radius, r_e, that encloses half of the galaxy light; and the index n, which is indicative of the concentration of the profile. Currently, there are several public software packages which do a good job in fitting galaxy models, e.g., GIM2D (Simard et al. (2002)) and GALFIT (Peng et al. (2002)) are two of the most commonly used.

ETGs are most often classified as ellipticals and S0s, hosting the major fraction of stars, and therefore of stellar mass in clusters. In contrast, late-type galaxies (LTGs) are typically spirals, are bluer and less massive than ETGs, and show emission lines indicative of ongoing star formation (see the mass function of local ETGs *versus* LTGs from Baldry et al. (2004)).

3.3 The Color-Magnitude Relation

Galaxy clusters are characterized by an old population of passively evolving galaxies, forming a distinct and tight sequence of galaxies in the color-magnitude relation, the red-sequence (Baum (1959), Visvanathan & Sandage (1977), Sandage & Visvanathan (1978), Bower et al. (1992)). This population has been observed to persist up to the

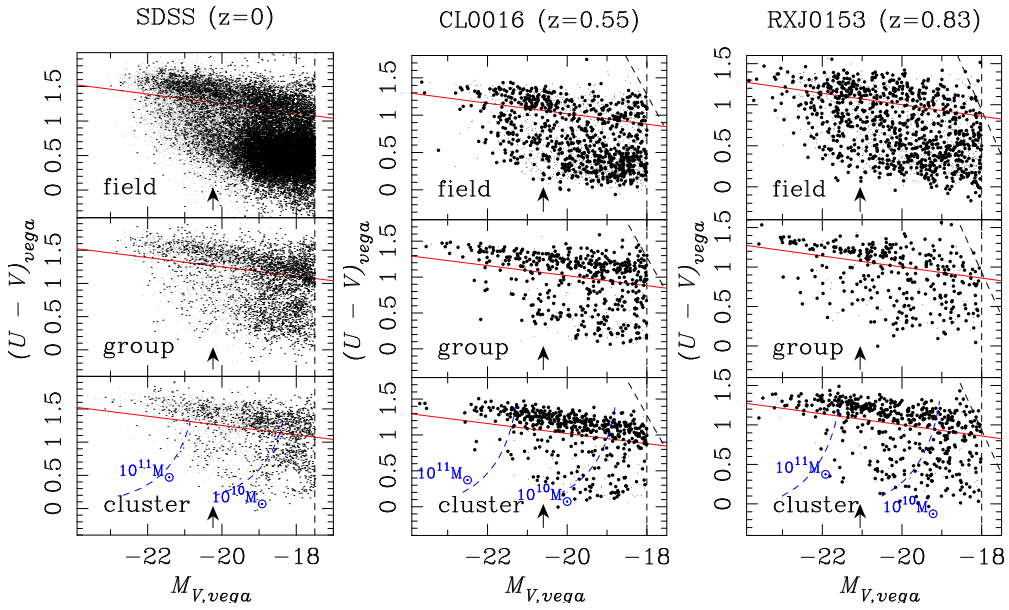

Figure 3.2: Color-magnitude diagrams at 3 redshifts: 0, 0.55, 0.83, and in 3 environments: the field, group and cluster. Red line indicates separation between red sequence and blue population. From Tanaka et al. (2005)

current redshift limit in clusters, that is z∼1.4 (Rosati (2008), Lidman et al. (2008), Stanford et al. (2006)), which is why the color-magnitude relation (CMR) is a fundamental scaling relation with which we can analyze galaxy properties over a large redshift range.

In addition to the red-sequence, a distinct population of blue late-type galaxies is also present in the CMR of galaxy clusters (as well as in the field though less markedly), evidencing a color bimodality strongly dependent on the sellar content of galaxies (Strateva et al. (2001)). The evolution of these two populations is presented in Fig. 3.2 from Tanaka et al. (2005), showing the CMR of galaxies in different environments: clusters (top), groups (middle) and the field (bottom)); over three epochs, z=0 (left), z=0.55 (middle) and z=0.83 (right). The red-sequence remains clearly distinguishable in all observations and the color bimodality (marked by the red line) is also present, although more strikingly in the high-density environments.

The CMR is an age indicator and can be understood as a mass-metallicity relationship (Kodama & Arimoto (1997); Gladders et al. (1998)), whose main parameters are the slope, zero point and scatter. If the brightest and the faintest galaxies evolve in the same timescale, we should expect metal-rich galaxies to become redder faster than the more metal-poor galaxies with increasing age. This is reflected in the slope of the CMR, where steeper slopes would indicate older galaxy age. However, recent

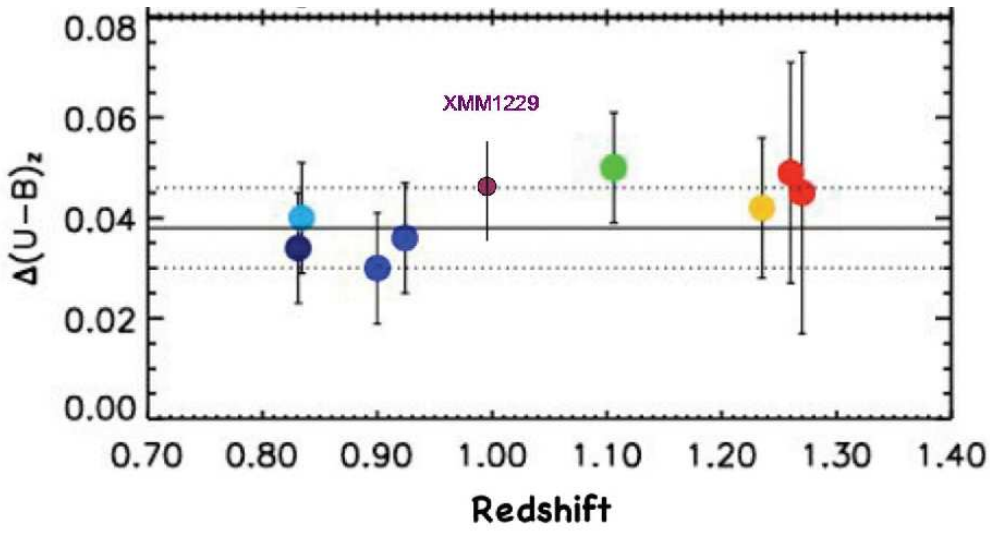

Figure 3.3: Evolution of the CMR scatter compiled by Mei et al. 2008. I have added the point corresponding to cluster XMMU J1229+0151 at z=0.975, which is analyzed in Chapter 6.

studies of galaxies in distant clusters indicate that the brightest galaxies seem to have already evolved and completed their star formation at z∼1 while fainter galaxies are still evolving and forming stars (e.g., Holden et al. (2005)).

The observed lack of strong evolution in the slope and scatter up to z∼1, supports the scenario of a mass-metallicity relation being the origin of the CMR. The scatter in the CMR is thought to originate mainly from galaxy age variations (e.g., Kodama & Arimoto (1997); Kauffmann & Charlot (1998)). Figure 3.3 shows the redshift evolution of the CMR scatter in a sample of eight clusters observed with HST/ACS, compiled by Mei (2008). The scatter is shown in the rest-frame (U-B) color.

3.4 The Fundamental Plane

The Fundamental Plane (FP) of elliptical galaxies (Dressler et al. (1987); Bender et al. (1992)) is an empirical relationship between the effective radius r_e, average surface brightness I_e and central velocity dispersion σ in the form $r_e \propto \sigma^{1.24} I_e^{-0.82}$. This relationship allows one to directly measure the mass and the mass-to-light ratio, M/L, of early-type galaxies, therefore the FP is a valuable tool to constrain the mass evolution of galaxies.

3.5 Synthetic stellar populations

Synthetic stellar population techniques are the common method to study the stellar content in galaxies, in order to constrain stellar masses, ages and star formation histories. Several codes are available to produce synthetic stellar populations, such as those of Fioc & Rocca-Volmerange (1997), Bruzual & Charlot (2003) and Maraston (2005), to cite a few of the most used codes. These models are based on stellar evolution theory assuming a Simple Stellar Population (SSP) where a single burst of star formation took place, with equal metallicity. SSP models require fairly complete libraries of stellar evolutionary sequences and stellar spectra to avoid false correlations (distorsions) on the stellar ages and metallicities, which are the main quantites to be determined. In addition to a stellar population synthesis code, we need to chose the initial mass function (IMF), describing the relative frequency with which stars of various masses are formed. Pioneering work in this field was done by Salpeter (Salpeter (1955)), although more recent developments have been reported, for instance in Chabrier (2003) and Kroupa & Weidner (2003).

Actually, the star formation history of galaxies is most likely due to a series of instantenous bursts, therefore their stellar population is better described with composite SSPs with different ages. Fitting these models to the observed spectral energy distributions (SED) is generally done through the minimization of the χ^2.

The star formation histories (SFH) of local galaxies in the field and in cluster environments was recently investigated in Thomas et al. (2005), modelling the formation and chemical evolution of galaxies assuming various SFHs characterized by different timescale formation histories. Galaxies in the field appear on average 1 to 2 Gyr younger than their counterparts in high density environments. This result is supported by similar studies from Sánchez-Blázquez et al. (2006) and Clemens et al. (2006).

Star formation histories are found to be mass dependent: the more massive elliptical galaxies have SFHs peaking at higher redshifts ($z \gtrsim 3$ in clusters) than less massive systems (De Lucia et al. (2004); Kodama et al. (2004); van der Wel et al. (2005)). This result is termed *downsizing*, in view of the star formation scenario proposed by Cowie et al. (1996). This is, nevertheless, in stark contrast to expectations based on the hierarchical growth of dark matter haloes in the adopted cosmology. The controversy of hierarchical and old ETGs is partly solved by allowing a late mass assembly via dry mergers, where small gas-free galaxies merge to form larger galaxies without increasing star formation. This implies that the stars in massive galaxies would be old, even though they would have formed recently (see for e.g. De Lucia et al. (2006)).

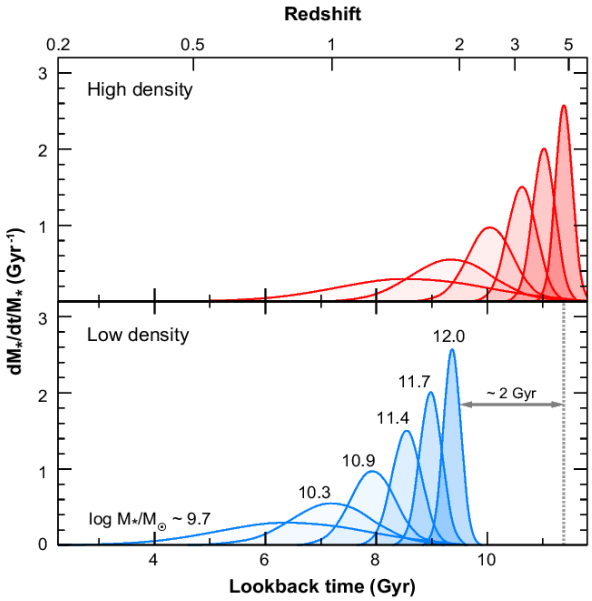

Figure 3.4: Star formation histories of early-type galaxies as a function of their stellar masses (see labels), in the cluster (*Top* panel) and field (*Bottom* panel) environments, from Thomas et al. (2005).

3.6 Brightest Cluster Galaxies

The central regions of massive galaxy clusters typically host a very bright and massive galaxy, the brightest cluster galaxy (BCG). Most BCGs are early-type galaxies, therefore their formation mechanism is still a matter of debate. The properties of BCGs are governed by their large stellar content and their ubiquitous location at the bottom of the potential well of their host cluster. In fact, BCGs are usually coincident with the peaks of X-ray emission and are connected with the presence of a cool core. They contribute to most of the iron content in the ICM. BCGs are also found to be larger and with higher velocity dispersions than non-BCGs of the same stellar mass, implying that BCGs contain a larger fraction of dark matter (von der Linden et al. (2007)).

Using high-resolution N-body simulations coupled to semi-analytic techniques, De Lucia & Blaizot (2007) investigated the formation and evolution of BCGs in a cosmological framework. Local BCGs seem to develop through the accretion of a small number of objects more massive than 10^{10}M$\odot$ with very low gas fractions and star formation rates. Such merging events are thus nearly dissipationless and are not associated with significant star formation. The bulk of the stars in BCGs starts

forming at very early times (about half of the stars in these systems have already formed by z∼5), though the final BCGs assemble from small progenitors rather late, by z ∼ 0.5. De Lucia & Blaizot also have shown that there is no substancial difference between local BCGs and the descendents of high-z BCGs and between high-z BCGs and the most massive progenitors of local BCGs.

3.7 The properties of cluster elliptical galaxies at z∼1

The study of cluster galaxies at z$\gtrsim$1 contributes with a strong leverage to constrain models of structure formation. Intense work has been done in this area in the last few years, mostly due to HST/ACS imaging, whose high-resolution is nearly mandatory for studies of high-redshift galaxies, although the newly commissioned ground-based HAWK-I NIR camera (Casali et al. (2006)) now online at the VLT has started to prove its competetiveness (Lidman et al. (2008)). In particular, the ACS Intermediate Redshift Cluster Survey, an ongoing guaranteed time observer (GTO) project, has the purpose of studying the properties and evolution of eight clusters and their galaxies in the redshift range z=[0.8 - 1.3], using the Wide Field Channel of the Advanced Camera for Surveys on the Hubble Space Telescope (Blakeslee et al. (2003, 2006), Homeier et al. (2005), Holden et al. (2005), Mei et al. (2006), Mei et al. 2008 submitted).

The rich, massive, and X-ray luminous cluster of galaxies RDCS 1252.9-2927 at z=1.237 (Rosati et al. (2004)) has been subject to extensive follow-up observations, from the UV to X-rays (e.g., Demarco et al. (2007), Gobat et al. (2008), Rettura et al. (2008)). Fundamental plane studies of four luminous early-type galaxies in this cluster confirm that massive cluster early-type galaxies appear to have a large fraction of stars that formed early in the history of the universe (Holden et al. (2005)). However, there is a large scatter in the derived M/L values, which is confirmed by the spread in the galaxies colors. Two lower mass galaxies in the z=1.25 sample have much lower M/L values, implying significant star formation close to the epoch of observation. There is thus evidence for significant recent star formation in the centers of some massive, M $\sim 10^{11}$M$\odot$, galaxies at z= 1.5. Gobat et al. (2008) have compared the SFHs of galaxies in this cluster and in galaxies at the same redshift in the GOODS field, in a similar fashion to the work done by Thomas et al. (2005) in local galaxies. Star formation histories were modelled with a delayed exponential parametrized by a time-scale τ, thus allowing for more complex SFHs. The authors find that cluster galaxies form the bulk of their stars $\sim$ 0.5 Gyr earlier than their counterparts in the field, with massive ETGs having already ended forming stars at z $>$ 1.5 in both environments. This is in agreement with other studies at similar redshift based on the measurement of the mass-to-light ratios of ETGs in cluster and field environments. (van Dokkum & van der Marel (2007)). Comparing these results

with the ones at low-redshift, one can be tempted to claim a true evolution of the SFH of ETGs. However, the observed discrepancy could be due to a progenitor bias: that the progenitors of the youngest E/S0 at low redshift are not classified as E/S0 at higher redshift, leading to an artificial slow evolution in colors and small color scatter at high-z, causing an overestimate of the epoch of formation of the bulk of the stars. Therefore, care must be taken when comparing high- with low-z samples.

One of the most distant clusters known to date, XMMU J2235.3-2557 at z=1.393 discovered in the XDCP survey (Chapter 5, Mullis et al. (2005)) has had a wide multi-wavelength coverage. In Fig. 5.1 we show the very recent HAWK-I J-Ks CMR from Lidman et al. (2008). Galaxies located in the cluster core form a well defined red-sequence with no evidence of ongoing star formation, however, cluster members outside the core are much more diverse. SSP models indicate that the core galaxies are about 3 Gyr old, corresponding to a redshift of formation of $z_f \sim 4$. These galaxies are therefore already very old, especially when we consider that the age of Universe at the cluster redshift is 4.6 Gyr. Several papers will follow in the near future, reporting the results obtained with the ACS and the *Chandra* data (see Rosati (2008)) of this unique system.

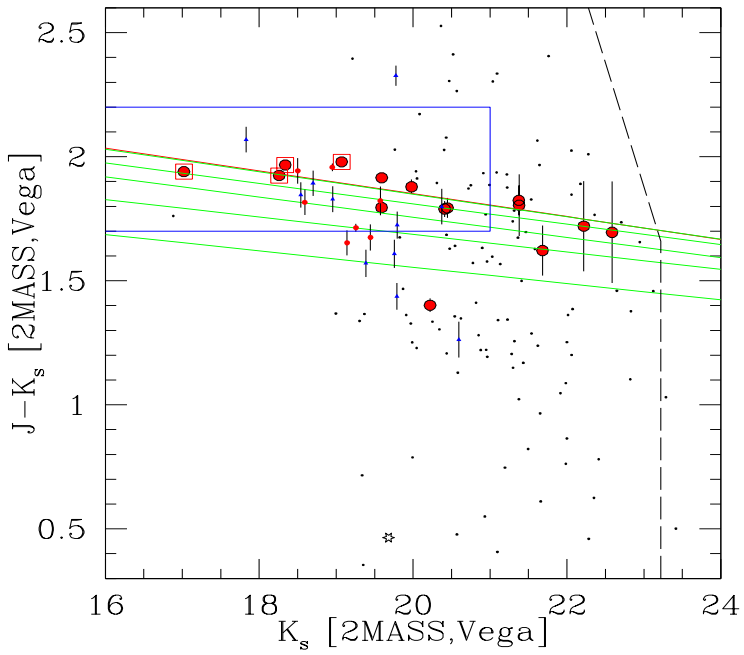

Figure 3.5: J-Ks color-magnitude relation of XMMU J2235.3-2557 at z=1.393 using HAWK-I, from Lidman et al. (2008)

Also a part of this thesis (Chapter 6) is dedicated to the study of the galaxy properties of XMMU J1229+0151, a cluster at z=0.975, using ACS imaging and FORS2 spectroscopy.

The combined outcome of these observational results complemented with advances in simulations, supports a scenario in which massive, passively evolving galaxies are already in place on the red-sequence at z$\sim$2 (Bernardi et al. (1998), van Dokkum et al. (2001)). Therefore the evolution of the number density of ETGs concerns mostly the fainter and less massive galaxies. Star formation appears to decline by $\sim 10^2$ from z=1.5 to z=0, although this effect is more dramatic (by a factor 1000) in massive early-types (Bower et al. (2006), Menci et al. (2008))

4

The evolution of Cool Core Clusters

Abstract

We investigate the detection of Cool Cores (CCs) in the distant galaxy cluster population with the purpose of measuring the CC fraction out to redshift $0.7 \leq z < 1.4$. Using a sample of nearby clusters spanning a wide range of morphologies, we define criteria to characterize cool cores, which are applicable to the high-redshift sample.

We analyzed azimuthally-averaged surface brightness (SB) profiles with the known scaling relations, and we fitted single/double β models to the data. Additionally, we measured a surface brightness concentration, c_{SB}, as the ratio of the peak over the ambient SB. To verify that this is an unbiased parameter as a function of redshift, we developed a model independent "cloning" technique to simulate the nearby clusters as they would appear at the same redshifts and luminosities as those in the distant sample. This method is based on the application of the cosmological surface brightness dimming to high-resolution Chandra images, assuming no intrinsic cluster evolution. We obtained a more physical parameterization of the CC presence by computing the cooling time at a radius of 20 kpc from the cluster center.

The distribution of the SB concentration and the stacked radial profiles of the low-z sample, combined with published information on the CC properties of these clusters, show 3 degrees of SB cuspiness: non-CC, moderate, and strong CC. The same analysis applied to the high-z clusters reveals two regimes: non-CC and moderate CC. The cooling time distribution corroborates this result by showing a strong negative correlation with c_{SB}.

Our analysis indicates a significant fraction of distant clusters harboring a moderate

CC out to z=1.4, similar to those found in the local sample. The absence of strong cooling is likely linked with a higher merger rate expected at redshift $z > 0.7$, and should also be related to the shorter age of distant clusters, implying less time to develop a cool core.

4.1 Introduction

Galaxy clusters are filled with hot, diffuse gas - the intracluster medium (ICM) - which strongly emits in X-rays. While the cluster dark matter distribution is generally described by its gravitational potential (Navarro et al. (1997)), the physical processes that govern the behavior of the ICM are complex and include non gravitational phenomena. Cool cores are a manifestation of these intricate processes.

According to observations (Jones & Forman (1984); Fabian et al. (1994); Peres et al. (1998); Chen et al. (2007)), relaxed galaxy clusters are most often found to exhibit at their centers a significant drop in the ICM gas temperature due to radiative cooling. It is by now established that the cooling time in the central regions of clusters is shorter than the Hubble time, thus originating very dense cores. Therefore, we expect to observe a surface brightness (SB) peak in these regions (with a typical radius of the order of 70 kpc - see, for example, Vikhlinin et al. (2005)) along with some other features such as an enhanced iron abundance.

The well-known cooling flow problem stems from the observation that the few detected emission lines are not as strong as expected to justify the predicted cooling rate. Further observational evidence is found in the ratio of the central temperature with respect to the global cluster temperature ($T_{central}/T$), which remains at a factor $\sim$1/3 (Peterson et al. (2003); Bauer et al. (2005)), and the mass deposition rates ($\dot{\mathrm{M}}$) are much smaller than expected (Edge & Frayer (2003)).

The existence of a feedback mechanism that counteracts the cooling is now widely accepted and currently, the most debated picture is heating by active galactic nuclei (AGN) (see review by Fabian et al. (1994)). Although several plausible models exist that may explain how this mechanism works (Churazov et al. (2000); Brüggen & Kaiser (2002)), and there is evidence for enough output mechanical energy to suppress cooling, it remains unclear how this energy is distributed in a homogenous way, such that cool cores appear in the form observed. Nevertheless, the cool core - AGN connection has been unambiguously demonstrated with observations, e.g., Burns (1990); Eilek (2004); Sanderson et al. (2006), report that nearly every cooling flow cluster hosts a radio-emitting AGN, creating cavities in the X-ray gas.

There is clear evidence for clusters harboring cool cores, however many clusters do not show any signatures of cooling. At this point, it may be pertinent to question whether there is a CC/non-CC bimodal cluster population. In this the case, are CC clusters primordial and were some of them (the non-cool core clusters) wiped out by

mergers or an AGN heating overshoot? Conversely, some authors support a scenario in which non-CC evolve to CC clusters if no major mergers occur (O'Hara et al. (2006)).

The role of mergers in destroying cool cores has long been debated (Fabian et al. (1984)), both from observational results and predictions from simulations. Currently, observations seem to favor CC destruction through cluster mergers (Allen et al. (2001); Sanderson et al. (2006)). Simulations, however, yield ambivalent results. Using adaptive mesh refinement simulations, Burns et al. (2008) advocate that non-cool core clusters undergo major mergers that destroy embryonic cool cores while CC clusters grow at a slower rate without suffering early substantial mergers. However, an analysis of smoothed particle hydrodynamical simulations of X-ray cluster mergers by Poole et al. (2006), suggests that the heating of the ICM arising from mergers is not sufficient to prevent cooling. They argue that, in the ΛCDM scenario, the merger rate is too small to account for the local abundance of non-CC clusters whose disruptions occurs on short timescales. We note, however, that a good agreement in the overall properties of observed and simulated CCs/NCCs is found by Burns et al., who were able to qualitatively reproduce the temperature structure observed in cool cores.

The present observational census on the abundance of cool core clusters sets a fraction of Cool Core Clusters (CCC) in the local Universe in the range of 50 -70 % (Peres et al. (1998); Chen et al. (2007)). As we move to increasing redshifts, there are fewer results on this topic. Using spatially resolved spectroscopy, Bauer et al. (2005) presented a comparative study of cool cores at low- and intermediate-redshift (mean z=0.06 and 0.22, respectively). The cool cores at intermediate redshift show the same temperature decrement, $T/T_{central} \sim$ 3-4, as the nearby CC's, and have a frequency rate similar to the local one. The central cooling time measurements confirmed this result. Consequently, they find no signs of evolution of the cool core fraction in the redshift range $z \sim\ 0.15 - 0.4$ to now.

At present, the knowledge of the high redshift cluster population is still rather poor: only 7 X-ray selected clusters with $z > 1$ have been confirmed (Rosati et al. (1999); Perlman et al. (2002); Stanford et al. (2002); Mullis et al. (2005); Stanford et al. (2006)). In particular, determining and quantifying the existence of cool cores at high redshift remains largely unexplored due to the lack of photon collecting power of current instruments to provide spectra with sufficient statistics for distant CC's. A first attempt to characterize a peaked core in high-redshift systems was undertaken in Ettori et al. (2004), using double beta model fitting. The outcome of this analysis states that a second beta model component cannot be required to describe the distant cluster data - at least, not in the same way as observed for nearby cool core clusters. Recently, Vikhlinin et al. (2007) presented a study on the evolution of CCC at $z > 0.5$ based on pure imaging data, using a distant cluster sample drawn from the 400SD survey imaged with Chandra. These authors claim a strong evolution of

the CC fraction in this redshift range, implying that we are missing cooling flows in the distant cluster population. However, this claim has been recently challenged with simulations by Burns et al. (2008), who found no evidence for such a decline in the Cool Core fraction in simulated data with redshift up to one.

The understanding of the formation and evolution of cooling flows is fundamental in pursuing cosmological studies with galaxy clusters. It is already known that cool core clusters affect the scaling relations causing a departure from the theoretical expectations and increasing the scatter (Fabian et al. (1994); Zhang et al. (2007)). Whether or not we can put together a consistent picture of clusters with and without cool cores will greatly affect the reliability of cluster results in deriving cosmological parameters.

In this paper, we investigate the fraction of cool core clusters in a high-redshift sample imaged with Chandra at $0.7 \leq z < 1.4$. To this aim we define and quantify criteria to select clusters as CCC in a sample of nearby clusters, $0.15 < z < 0.3$, which are then applied to the distant sample. The low-z clusters exhibit markedly different morphologies which is essential to characterize cool cores with varying strength. The low-photon statistics of the distant clusters made a spatially resolved temperature analysis inviable, constraining our study to a spatial analysis of the cluster images. We analyzed the overall surface brightness and determined cooling times in the clusters' central regions. The surface brightness diagnostics were developed based on the nearby sample and were validated to high-z with simulated distant clusters. These were obtained with the cloning technique, a novel method in which we simulate distant galaxy clusters by emulating the appearance of the low-z clusters at the same redshifts of the observed distant sample. Such simulations allow us to make an unbiased comparison of cluster spatial properties between nearby and distant populations.

The two cluster samples are drawn from the Chandra archive. The high-z sample, which is the most relevant for this study, is a statistically-complete sample based on the Rosat Distant Cluster Sample (RDCS), from Rosati et al. (1998). This dataset allows us to draw conclusions on the abundance of CCC when the Universe was $\sim 1/3$ of its age. On the other hand, we constructed the nearby sample by taking morphologically interesting archive clusters, and we used the sample as a test set to understand how we can characterize cool cores.

We note that archive samples will likely be biased in the sense that the majority of the observed clusters are "interesting", meaning showing signs of mergers / disruptions, or on the contrary, having very regular shapes. In addition, cluster selection based on flux limited samples will preferentially find high luminosity/mass clusters at high redshift. This effect, goes in the direction of favoring CC clusters (which have a bright core) with increasing z. For these reasons, constructing complete, unbiased samples to address issues of cluster evolution presents difficulties that should be carefully dealt with. Since the distant and nearby samples are not drawn from a

homogenous sample with a known selection function, we do not address the issue of evolution of cool cores on this paper.

As a complement to this X-ray study and with the aim of understanding sample selection effects, we shortly investigate the surface brightness properties of an optically-selected sample of high-z galaxy clusters imaged with Chandra. We assess the incidence rate of cool cores and compare it with the results on the X-ray selected cluster set.

We introduce the cluster samples in Sect. 2, and in Sect. 3 the surface brightness profiles are presented, together with the beta model fitting. In Sect. 4, we introduce the surface brightness concentration parameter (c_{SB}) and outline the simulation method we used to test its application. The combined results on the surface brightness profiles and concentration parameter are presented in Sect. 5. The cooling time analysis is described in Sect. 6; Sect. 7 is dedicated to a comparison of X-ray surface brightness properties in optically and X-ray selected high-redshift galaxy clusters. Finally, in Sect. 8 we discuss the results obtained and conclude. The cosmological parameters used throughout the paper are: H_0=70 km/s/Mpc, Ω_Λ=0.7 and Ω_m =0.3.

4.2 Cluster samples

We used archive Chandra ACIS-I and ACIS-S images in the [0.5-5.0] keV energy range: we selected the 11 low-z clusters (Table 1) from the sample compiled by Baldi et al. (2007); the high redshift X-ray selected sample, which comprises 15 clusters (first part of Table 2), was drawn from the sample presented in Balestra et al. (2007). We, therefore, refer the reader to these two papers for details in the data processing. In Table 2 we also present the optically-selected distant sample which will be discussed in Sect. 7.

We removed point sources from all images and filled the gaps between the detector chips assuming Poisson statistics, interpolating with neighboring pixels (dividing images by exposure maps is not enough for gap removal because the images are subject to noise propagation). We determined the local background in empty regions of the cluster images; when computing the background a Gaussian filter with a kernel of 1 was applied to the images to avoid zero pixel values. We determined the cluster number counts with the growth curve analysis (Böhringer et al. (2000)): cluster counts are calculated in circular apertures until the background level is reached. The maximum value of the growth curve was taken as the nominal cluster number of counts. For each cluster we determined the center-of-mass coordinates, and assigned this value to the cluster center.

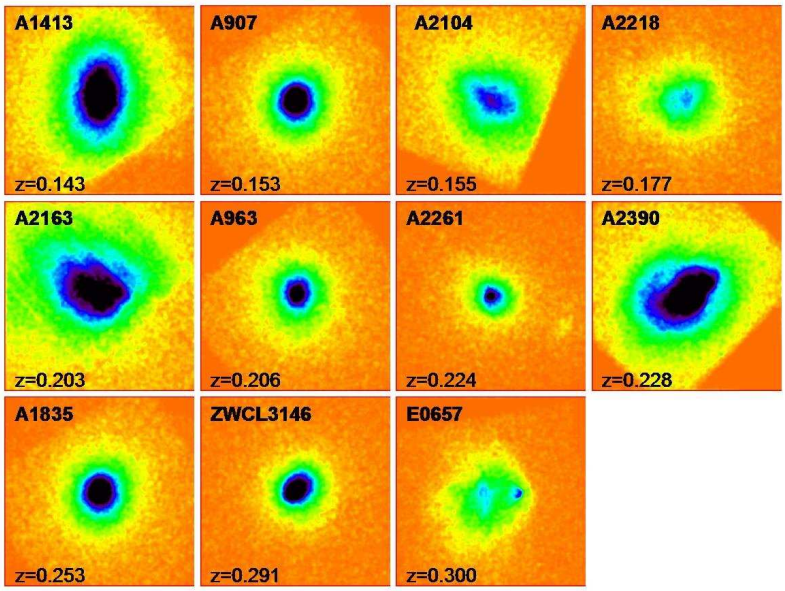

Figure 4.1: Nearby cluster sample observed with Chandra (point sources are removed). Images are smoothed with a gaussian of sigma=3 and rescaled by the square root of the intensity. Individual boxes have a size of 8x8 arcmin. Cluster redshift increases from top-left to bottom-right.

Table 4.1: Low redshift cluster sample.

Cluster ID	z	T (keV)	RA (Eq. J2000)	DEC (Eq. J2000)	Exposure (ksec)
A1413[a]	0.143	$7.52^{+0.20}_{-0.12}$	11:55:18.20	+23:24:28.80	136
A907[a]	0.153	5.82 $\pm$0.12	09:58:22.00	-11:03:50.40	100
A2104[a]	0.155	6.76 $\pm$0.19	15:40:07.90	-03:18:04.00	48
A2218[a]	0.177	6.25 $\pm$0.31	16:35:56.00	+66:12:45.00	57
A2163[b]	0.203	$12.3^{+1.3}_{-1.1}$	16:15:45.77	-06:08:55.00	80
A963[a]	0.206	$6.02^{+0.28}_{-0.19}$	10:17:03.40	+39:02:51.00	36
A2261[a]	0.224	$7.43^{+0.49}_{-0.27}$	17:22:27.20	+32:07:58.00	32
A2390[a]	0.228	9.35 $\pm$0.15	21:53:36.50	+17:41:45.00	111
A1835[a]	0.253	8.09 $\pm$0.53	14:01:02.00	+02:52:40.00	30
ZwCl3146[a]	0.291	8.59 $\pm$0.39	10:23:39.60	+04:11:10.00	45
E0657[c]	0.300	14.1 $\pm$0.2	6:58:28.60	-55:56:36.03	25

[a] Temperatures taken from Baldi et al. (2007), [b] temperature from Markevitch & Vikhlinin (2001), [c] temperature from Markevitch (2006).

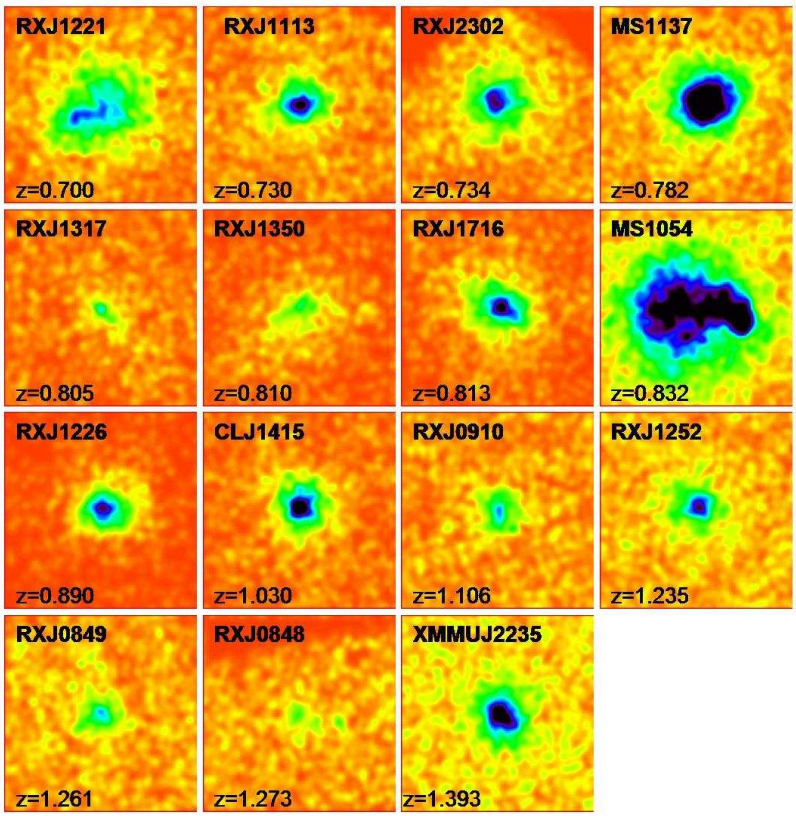

Figure 4.2: X-ray selected, distant cluster sample observed with Chandra (point sources are removed). Images are smoothed with a gaussian of sigma=3 and rescaled by the square root of the intensity. Individual boxes have a size of 3x3 arcmin. Cluster redshift increases from top-left to bottom-right.

4.2.1 Low-z sample

The nearby cluster sample ($0.15 < z < 0.3$, median z=0.21) is presented in Fig. 4.1. The selection criteria for its construction were essentially of observational nature, since we were interested in low-redshift clusters with a size that would properly fit within the field of view of Chandra (16 arcmin^2), and with sufficiently high number of counts ($>$ 10 000) to ensure a proper analysis with good enough statistics of the cloned data (see Sect. 4.2 for details on the cloning technique). The sample is heterogeneous in the sense that we wanted to have clusters with known classification in terms of CC/non-CC; we therefore gathered this information from the literature (Vikhlinin et al. (2005); Bauer et al. (2005); Reese et al. (2002); De Filippis et al. (2005); Arabadjis et al. (2002); Pratt & Arnaud (2002)). According to these various

Table 4.2: High redshift cluster samples.

Cluster ID	z	T (keV)	RA	DEC	Exp (ksec)
RX J1221+4918	0.700	$8.4^{+0.8}_{-0.8}$	12:21:24.50	+49:18:14.40	78
RX J1113-2615	0.730	$5.6^{+0.9}_{-0.6}$	11:13:00.00	-26:15:49.00	103
RX J2302+0844	0.734	$8.0^{+1.2}_{-1.1}$	23:02:48.06	+08:43:54.72	108
MS1137+6625	0.782	$6.8^{+0.5}_{-0.5}$	11:40:22.81	+66:08:14.50	117
RX J1317+2911	0.805	$4.4^{+1.4}_{-0.9}$	13:17:21.84	+29:11:17.00	111
RX J1350+6007	0.810	$4.5^{+0.7}_{-0.6}$	13:50:47.78	+60:07:13.32	58
RX J1716+6708	0.813	$6.9^{+0.8}_{-0.7}$	17:16:48.76	+67:08:25.81	51
MS1054-0321	0.832	$7.5^{+0.7}_{-0.4}$	10:56:58.00	-03:37:37.30	80
RX J1226+3333	0.890	$12.9^{+1.4}_{-1.3}$	12:26:58.20	+33:32:48.00	9.5 + 31.5
CL J1415+3612	1.030	$7.0^{+0.8}_{-0.7}$	14:15:11.20	+36:12:04.00	89
RX J0910+5422	1.106	$6.4^{+1.5}_{-1.2}$	09:10:45.41	+54:22:05.00	170
RX J1252-2927	1.235	$7.3^{+1.3}_{-1.0}$	12:52:54.50	-29:27:18.00	188
RX J0849+4452	1.261	$5.3^{+1.7}_{-1.1}$	08:48:58.52	+44:51:55.08	185
RX J0848+4453	1.273	$2.4^{+2.5}_{-1.0}$	08:48:36.20	+44:53:47.17	185
XMMU J2235-2557[a]	1.393	$6.0^{+2.5}_{-1.8}$	22:35:20.70	-25:57:40.70	189
RCS1419+5326	0.620	$5.0^{+0.4}_{-0.4}$	14:19:12.14	+53:26:11.56	56
RCS1107.3-0523	0.735	$4.3^{+0.5}_{-0.6}$	11:07:24.08	-05:23:23.19	93
RCS1325+2858	0.750	$1.8^{+1.2}_{-0.6}$	13:26:31.04	+29:03:25.02	62
RCS0224-0002	0.778	$5.1^{+1.3}_{-0.8}$	02:24:33.61	-00:02:24.68	101
RCS2318.5+0034	0.780	$7.3^{+1.6}_{-1.0}$	23:18:30.67	+00:34:03.03	50
RCS1620+2929	0.870	$4.6^{+2.1}_{-1.1}$	16:20:10.01	+29:29:15.41	34
RCS2319.9+0038	0.900	$5.3^{+0.7}_{-0.5}$	23:19:53.59	+00:38:09.05	62
RCS0439.6-2905	0.960	$1.8^{+0.4}_{-0.3}$	04:39:37.76	-29:04:49.40	92
RCS1417+5305	0.968	...	14:17:02.13	+53:05:23.57	62
RCS2156.7-0448	1.080	...	21:56:41.63	-04:47:53.47	71
RCS2112.3-6326	1.099	...	21:12:20.51	-63:26:13.97	68

[a] The temperature of this cluster was taken from Mullis et al. (2005). Temperatures for RCS clusters refer to Bignamini et al. (2008). All other temperatures refer to the values given by Balestra et al. (2007).

sources, clusters A2104, A2218, A2163, and E0657 are obvious non-coolcores whereas A1835 and ZWCL3146 are rare, high luminosity systems, exhibiting pronounced cool cores. Cluster temperatures obtained with spectroscopic fitting were taken mostly from Baldi et al. (2007) and also from Markevitch & Vikhlinin (2001); Markevitch (2006) for clusters A2163 and E0657, respectively. Cores were excised when a cool

core was present. All systems have $T > 5$ keV.

4.2.2 High-z sample

The distant cluster sample (Fig. 4.2) is drawn, mostly, from the RDCS (Rosati et al. (1998)), with one important addition: a 190 ksec Chandra exposure of XMMUJ2235.3-2557 (hereafter XMMUJ2235), with z=1.393. This massive object is the highest redshift cluster in our sample and the second most distant cluster (Mullis et al. (2005)) confirmed to date (the most distant cluster known so far has redshift 1.45 (Stanford et al. (2006)). The sample ranges from 0.70 to 1.39 in redshift (median z=0.83), which spans a lookback time between 6.3 and 9.0 Gyrs, for the assumed cosmology. These are all massive clusters, spanning approximately a decade in mass, with the exception of RXJ0848+4453 which has a temperature of 2.4 keV. The remaining clusters in the sample have bulk temperatures that range from 4.4 to 12.9 keV and were obtained by spectroscopic fitting. Temperature measurements and general Chandra imaging reduction was extensively described in Balestra et al. (2007). Concerning XMMUJ2235, we quote the temperature obtained by Mullis et al. (2005) using XMM-Newton data, although a more precise spectroscopic analysis of the new Chandra data will be available soon (Rosati (2008)). Cluster number counts range from 250 to 11000 with a median value of 1750 counts.

4.3 Surface brightness profiles

4.3.1 Scaled surface brightness profiles

Galaxy clusters are expected to exhibit self-similarity, which allows us to link their physical properties with temperature. This prediction is based solely on gravitational arguments where clusters are described as dark matter dominated entities. However, there has been evidence for a departure from the self-similar scaling scenario (Arnaud (2005); Chen et al. (2007)): the $L_X \propto T^2$ scaling relation expected in the case of gravitational only processes, is at odds with the observed $L_X \propto T^{2.88}$ relation. This implies the intervention of nongravitational phenomena that provide extra energy input (Arnaud & Evrard (1999)). An empirical scaling law was then derived which fits to the observations.

For comparison between the local and distant clusters, we scaled the surface brightness profiles according to both the empirical and self-similar scaling relations. In a self-similar, purely gravitational scenario, the surface brightness scales as $S_X \propto T^{0.5}$, whereas in an empirical derivation $S_X \propto T^{1.38}$ (Neumann & Arnaud (1999); Arnaud et al. (2002)).

We took into account the surface brightness dimming and considered the redshift evolution of the $L_X - T$ and $R - T$ relations (see e.g. Ettori et al. (2004)) obtaining:

$$S_X h(z)^{-3} \propto T^{\alpha}(1+z)^4 K_{corr} \tag{4.1}$$

where $h(z)$, the cosmological factor, is defined as the Hubble constant normalized to its current value, $H_z/H_0 = \sqrt{\Omega_m(1+z)^3+\Omega_\Lambda}$. The slope α is dependent on the scaling relation and K_{corr} is the K-correction, which is defined in Sect. 4.2.1.

The way in which scaling relations affect our analysis needs some clarification. The purely self-similar gravitational scenario (eg. Navarro et al. (1996, 1997)), which seems to be reasonably-well supported by observations, predicts an evolution of the dark matter halos becoming more compact for fixed enclosed mass with increasing redshift. This is reflected in the global appearance of the ICM and the cluster morphology in X-rays, including further modification due to changes in the ratio of gas to total mass (Arnaud et al. (2002)). This intrinsic evolution of the global cluster appearance is accounted for by the above-mentioned empirical scaling relations. Focusing on the study of cool cores in clusters, we are rather more interested in the local physical conditions at the cluster center that are, for example, characterized by the cooling time of the gas or the total radiative energy loss of the ICM in the cool core region. This characterization is not subject to the above-described scaling relations. Thus, if we are interested in comparing the rate at which the central ICM is radiatively cooling in nearby and distant clusters, we have to compare the cluster properties in fixed physical units. We will, therefore, in the following use the empirical scaling relations to reveal changes of the global cluster and cluster ICM structure properties, while we will use unscaled relations to directly compare physical conditions in the cooling cores.

We adopted a fixed density contrast Δ=500 with respect to the critical density of the Universe at the cluster redshift ($\rho_c(z)$) to study the global properties of clusters. The fiducial radius, R_{500}, was determined using the $R_{500}-T$ relation in Evrard et al. (1996), represented by the following fitting function:

$$R_{500} = h(z)^{-1} 2.48 (kT/10keV)^{0.5} H_{50}/H_{70} \tag{4.2}$$

Eq. (2) is applicable for clusters with T $>$ 3.5 keV.

From the top panels in Fig. 4.3, it is clear that the low-z profiles converge well for $r > 0.2 \times R_{500}$. However, at high-z two outliers are evident in the self-similar scaling (bottom-right plot): MS1054-0321 (hereafter MS1054) and RX J1226+3333. The former is a merging cluster and the latter is the hottest distant cluster. Interestingly, RX J1226+3333 does not appear as an outlier when using the empirical scaling. This reinforces the better use of the empirical relation, which does not boost the clusters at the extreme (highest temperature) outside the bulk of the data points in the relation.

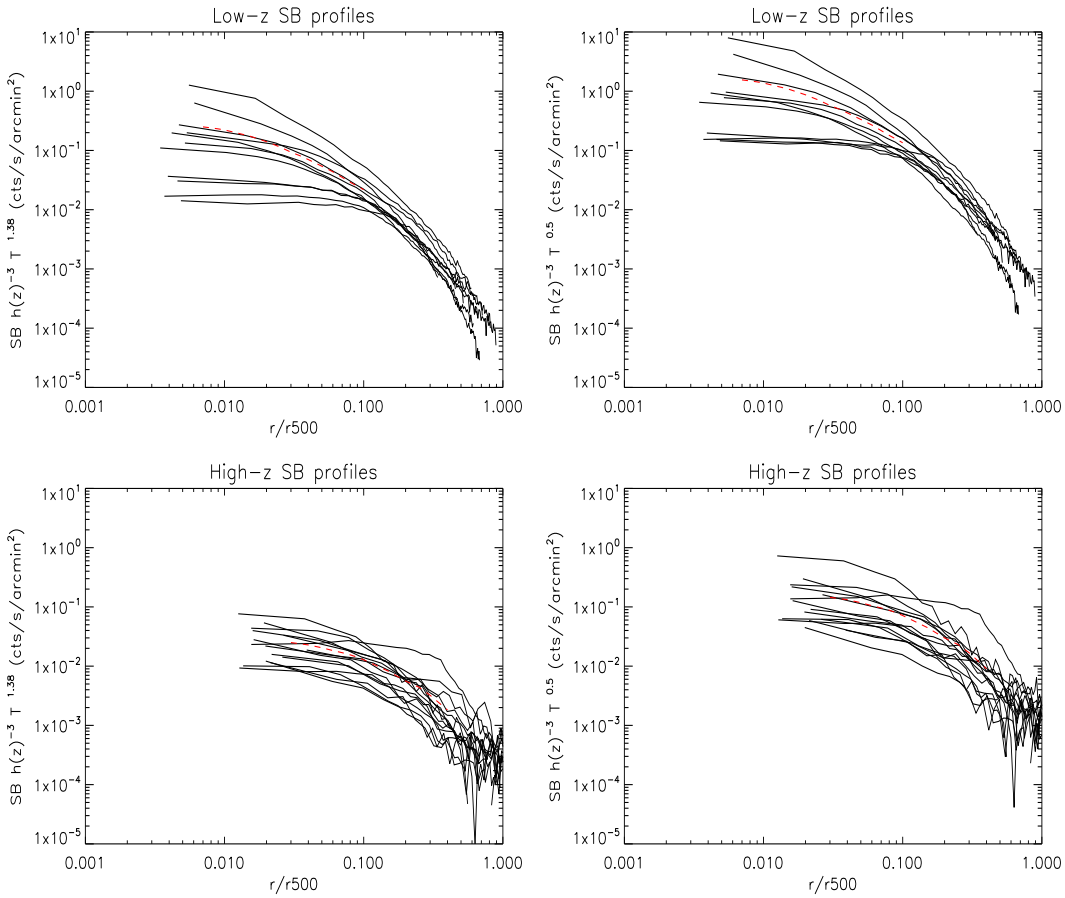

Figure 4.3: *Left* Empirical scaling of SB profiles - low-z sample (*Top*) and high-z sample (*Bottom*) *Right* Self-similar scaling of SB profiles - low-z sample (*Top*) and high-z sample (*Bottom*). The red-dashed lines correspond to the averaged profiles.

A striking difference between the CC and non-CC clusters in the nearby sample is evident in Fig. 4.3 (top panels). The flatness of the profiles of non-cool core clusters A2104, E0657, A2218, and A2163 are in obvious contrast with the remaining profiles that have a much higher central surface brightness - up to nearly 2 orders of magnitude larger - and a steepness that varies according to the strength of the cool core. This result is independent of the choice of scaling. At high redshift this marked distinction is not apparent.

The scatter of the surface brightness profiles scaled with $T^{0.5}$ amounts to 50% of the average value in the low-z sample at r=$0.3 \times R_{500}$. In the distant sample, the

Table 4.3: Single and double beta model fitting results: core radius, r_c, slope β and reduced χ^2. Errors are not presented when the parameter value is at the limit imposed by the fitting procedure.

	1β fit			2β fit				
cluster	β	r_c(kpc)	χ^2_{red}	β_1	r_{c1}(kpc)	β_2	r_{c2}(kpc)	χ^2_{red}
A1413	0.473±0.002	56±1	1.821	0.755±0.057	70±5	0.900	286±2	1.153
A907	0.515±0.002	42±1	6.360	0.635±0.152	29±6	0.706±0.045	131±16	1.439
A2104	0.566±0.014	161±6	1.335	–	–	0.542±0.018	162±7	1.447
A2218	0.841±0.150	222±30	1.220	–	–	0.606±0.007	159±4	1.326
A2163	1.003±0.056	349±15	1.277	–	–	0.517±0.003	184±2	2.909
A963	0.516±0.003	68±1	1.165	0.702±0.063	76±7	0.900	301±8	1.133
A2261	0.540±0.008	66±3	1.147	1.200	49±11	0.559±0.006	80±5	1.090
A2390	0.474±0.001	46±1	17.037	0.619 ±0.020	49±2	0.900	411±5	2.561
A1835	0.528±0.001	29±0.3	3.530	0.699 ±0.050	34±3	0.719±0.016	179±12	1.803
ZwCl3146	0.573±0.001	2±1	5.012	0.639± 0.156	18±5	0.667±0.023	93±9	1.224
E0657	1.000	477±4	1.864	–	–	0.900	433±3	1.919
RX J1221+4918	0.702±0.067	262±31	1.285	–	–	0.763±0.062	281±28	1.321
RX J1113-2615	0.668±0.066	107±17	1.178	1.000	98±46	0.800	188±84	1.048
RX J2302+0844	0.451±0.041	73±16	1.039	0.470±0.041	68±8	–	–	1.155
MS1137+6625	0.807±0.041	157±10	1.152	1.000	77±25	0.800	55±14	0.961
RX J1317+2911	0.537±0.094	67±29	1.039	1.000	52±38	0.800	175±53	1.020
RX J1350+6007	0.561±0.095	162±45	1.085	0.683 ±0.523	36±27	0.800	341±48	0.909
RX J1716+6708	0.740±0.062	165±20	0.988	1.000	28±6	0.695±0.071	154±25	0.930
MS1054-0321	1.000	443±5	2.826	–	–	0.800	360±5	2.924
RX J1226+3333	0.710±0.053	131±16	0.851	1.000	23±11	0.727±0.063	136±21	0.857
CL J1415+3612	0.552±0.026	61±8	1.043	0.704±0.094	140±40	0.800	35±12	0.954
RX J0910+5422	0.997±0.320	177±57	1.017	1.000	39±13	0.800	158±19	1.022
RX J1252-2927	0.557±0.067	89±21	1.103	1.000	33±18	0.601±0.111	108±41	1.114
RX J0849+4452	0.537±0.05	72±19	1.143	1.000	29±14	0.800	127±17	1.043
RX J0848+4453	0.590±0.179	122±69	0.823	1.000	32±54	0.800	188±62	1.193
XMMU J2235-2557	0.595±0.028	94±11	1.197	1.000	33±18	0.800	155±11	1.090

scatter is boosted by MS1054; if we neglect this outlier we obtain a dispersion around the mean value of 65% at the same radius.

4.3.2 Single and Double Beta model fitting

Cluster surface brightness profiles are commonly analyzed with the approximation of the single isothermal beta model (Cavaliere & Fusco-Femiano (1976)). We computed azimuthally-averaged surface brightness profiles in bins of fixed radius, which were fitted with a single β model:

$$S(r) = S_0(1 + (r/r_c)^2)^{-3\beta+0.5} + C \tag{4.3}$$

where S_0, r_c, β and C are the central surface brightness, core radius, slope and constant background, respectively. The fitting procedure was performed with a Levenberg-Marquardt least-squares minimization.

When a cluster harbors a cool core, a single beta model is often inappropriate to describe its central excess emission, requiring the use of a 2β model:

$$S(r) = S_{01}(1 + (\frac{r}{r_{c1}})^2)^{-3\beta_1+0.5} + S_{02}(1 + (\frac{r}{r_{c2}})^2)^{-3\beta_2+0.5} + C \tag{4.4}$$

Such a conclusion has been reached through observations (Jones & Forman (1984); Vikhlinin et al. (2005)) and is also expected from simulations (Burns et al. (2008)). However, this observation cannot be as clearly seen for the high-z clusters because the low statistics provides a good χ^2_{red} with either a single or a double β function. This has been previously noted by Ota & Mitsuda (2004) who analyzed a sample of 79 clusters with $0.1 < z < 0.8$, and in Ettori et al. (2004), where nearly all distant clusters in our sample were analyzed. There are however exceptions such as cluster CL J1415+3612 at z=1.03, in which the single beta model fails to capture the central SB. A double β model is qualitatively more appropriate to describe the core SB excess, although there are no significant differences in the reduced χ^2 values of the 1β and 2β model fit: χ^2_{red}=1.043 in the 1β model fit and χ^2_{red}=0.954 in the 2β model fit. These results make it obvious that fitting single/double β models to quantify the central surface brightness is not conclusive for the high-z sample.

Of particular interest is XMM2235, the most distant cluster in sample which, in spite of its high redshift, does require a 2-component β model to properly describe the surface brightness. In Fig. 5.1 we show the single and double beta model fit to the surface brightness profile; the 1β model fit (blue line) clearly does not capture the central excess however the double β model is a perfect match to the data. A comprehensive analysis is provided in Rosati (2008).

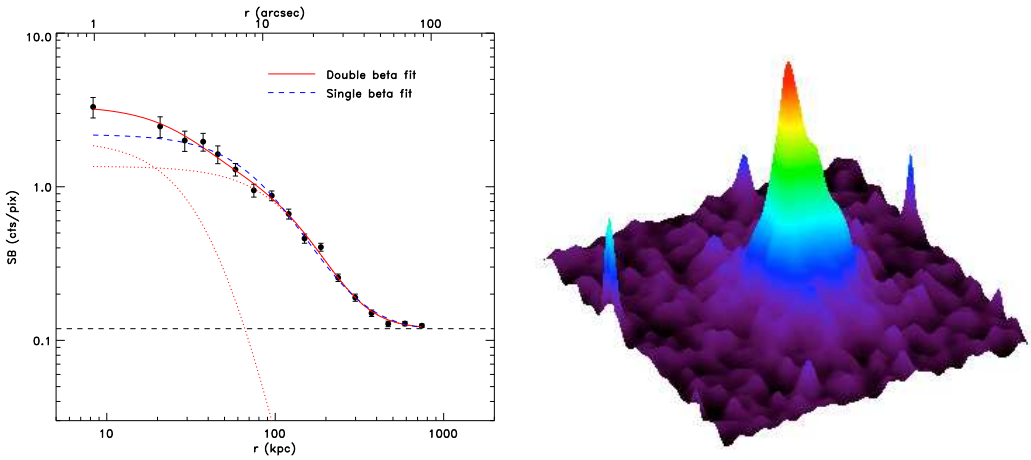

Figure 4.4: *Left* Surface brightness profile of XMM2235. The blue line refers to the 1β model fit which fails to describe the profile in the core region. A two component fit is shown in red: the solid line refers to the composite fit and in dash lines we show the two separate components. *Right* Surface plot of the X-ray image. The color scale indicates the intensity: red corresponds to higher intensity and blue corresponds to lower intensity.

The β-model parameters will not be used further in our study to characterize CCs, as we found them less useful than the following approaches. We, nevertheless, report our results in Table 3 for comparison with other work. Since the double-β model results give, in general, a good representation of the data within the error bars, the model fits also allow for an approximate check and reproduction of our analysis.

4.4 Surface Brightness Concentration

4.4.1 Introducing c_{SB}

In principle, the most stringent proof for the detection of a cool core is given by the temperature decrease in the core with respect to the bulk of the cluster. Unfortunately, the poor photon statistics does not permit a spatially-resolved spectroscopic analysis of the high-z sample.

Since a central surface brightness excess is a primary indicator (Fabian et al. (1984)) of the presence of a cool core, we evaluate the core surface brightness in nearby clusters by defining a concentration parameter as the ratio of the peak over the ambient SB. The aim of this approach is to use a single parameter to make a practical initial classification of cool cores. We chose the apertures corresponding to the peak and the bulk to yield the largest separation between the CC and non-CC domains. We optimized the c_{SB} parameter with the low-z sample, varying the radius of the central peak and external radius. The optimal c_{SB} is found for a peak radius of 40 kpc and a cluster bulk radius of 400 kpc:

$$c_{SB} = \frac{SB(r < 40kpc)}{SB(r < 400kpc)} \tag{4.5}$$

To support this result, we carried out extensive Monte Carlo simulations of CC and non-CC clusters modelled with, respectively, double and single beta profiles to optimize the choice of the internal and external apertures in the definition of c_{SB}. We explored the range of 30-80 kpc around the typical observed size of cool cores in nearby clusters. We selected an inner radius of 40 kpc to make the separation between CC and non-CC clusters more obvious. We measured the concentration parameter, as defined in Eq. (5), in simulated clusters and we found that it efficiently separates the two classes of objects.

Defining c_{SB} in terms of fractions of a scaled radius such as R_{500} proved not to be suitable because the wide range covered in redshift implies sampling cluster regions of various sizes for different redshifts. For example, $0.1R_{500}$ amounts to 132 kpc for the most nearby cluster, whereas for the most distant cluster it corresponds to 65 kpc. Keeping in mind that the cool core region has been broadly described as the inner 70 kpc of a cluster, it is evident that using fractions of R_{500} will introduce a bias toward lower redshift systems appearing more concentrated. In addition, scaling the radius

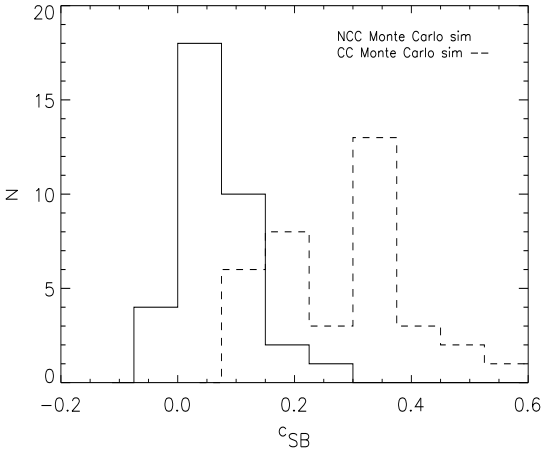

Figure 4.5: c_{SB} distribution of Monte Carlo simulations of cool core clusters (solid) and non-cool core clusters (dashed).

with temperature would only be meaningful if the cluster samples spanned a different temperature range and/or if there were poor ($T < 3.5$ keV) systems, which is not the case here. Therefore we used a physical radius for measuring the concentration index.

Having thus defined the empirical c_{SB} parameter with the low-z sample, we investigate whether there is a redshift dependence bias associated with this parameter that would invalidate the comparison of c_{SB} results between the samples. To this end, we developed a simulation method that clones the observed low-z clusters to high redshift. Measuring the c_{SB} of simulated distant clusters provides a straightforward way to test for a redshift dependence. We describe this technique in the following section.

4.4.2 Testing c_{SB} with the Cloning method

The cloning technique has been applied in an optical study by Bouwens et al. (1998), with the purpose of quantifying the evolution of faint galaxies, using low-z galaxies in the Hubble Deep Field. By applying a pixel-by-pixel K-correction map to high resolution images of bright galaxies, a set of no-evolution deep fields was created, taking into account the space density and the cosmological volume.

We have revised and adapted the cloning method with the purpose of simulating distant clusters of galaxies as standard nonevolving clusters that can be compared with distant samples. We cloned the low-z sample to the redshifts matching those of the distant sample, and for consistency in the comparison we normalized the

simulated cluster counts to the corresponding expected high-z cluster counts, adding the observed high-z background as well. Chandra angular resolution is essential for our analysis. Its point spread function (PSF) with a FWHM of $\sim$ 1 arcsec corresponds to 8 kpc at z=1. Considering that the typical physical size for the CC region is about an order of magnitude larger than the instrument resolution, there is no need to deconvolve the images with the PSF, which would make the application of our method very difficult. One of the main advantages of this technique is that it is model independent, implying that the simulations are under control, as no tuning of parameters is required. The assessment of the selection effects is rather robust since we only have to rely on the data.

The procedure comprises essentially 2 steps: the flux decrease and the spatial rescaling which the template cluster undergoes.

4.4.2.1 Flux dimming: luminosity distance and K-correction

The cluster flux decrease is due to both the physical luminosity distance, D_L, and the redshifted energy band. In the adopted cosmology, D_L is given by (see for instance, Carroll et al. (1992); Perlmutter et al. (1997)):

$$D_L = \frac{c(1+z)}{H_0} \int_0^z h(z)^{-1} dz \quad . \tag{4.6}$$

The X-ray flux is thus given by

$$F_x = \frac{L_x}{4\pi D_L^2} \tag{4.7}$$

where L_X is the X-ray luminosity in the observed frame. Therefore, when cloning to a higher redshift, we must compute the ratio of the squared luminosity distances.

As we are using images in a given energy band (0.5-5.0 keV), a bandpass correction - the K-correction - plays an important role in the flux rescale because we are dealing with high redshift values (Hogg et al. (2002)). If f_ν is the unabsorbed spectral flux density, we can express the K-correction for an energy band $[E_1, E_2]$ as:

$$K_{corr} = \frac{f_\nu(z_1, \frac{E_1}{1+z_1}, \frac{E_2}{1+z_2})}{f_\nu(z_2, \frac{E_1}{1+z_1}, \frac{E_2}{1+z_2})} \frac{ecf(\frac{E_1}{1+z_1}, \frac{E_2}{1+z_2}, z_1, N_H, Z)}{ecf(\frac{E_1}{1+z_1}, \frac{E_2}{1+z_2}, z_2, N_H, Z)} \tag{4.8}$$

where ecf stands for energy conversion factor, a term that relates flux to counts, and depends on the cluster redshift, hydrogen column density, N_H, and metallicity, Z.

Since the emissivity is not very temperature sensitive in the energy band used for the surface brightness measurements, it is practical and justified to treat the cluster

ICM as isothermal. The K-correction terms are dependent mostly on the cluster redshift (this dependence is stronger for $z > 0.5$) and temperature. The latter has a steeper effect for poor systems ($T < 3$ keV) which is not the case here. Applying single cluster temperatures, we computed K-corrections with XSPEC v11.3.1 (Arnaud (1996)). We used the optically-thin MEKAL model spectra (Kaastra (1992)) with photoelectric absorption (WABS(MEKAL)), setting the metallicity to 0.3 solar and N_H=8×10^{20}cm^{-2}. The spectra were folded with Chandra responses. The metallicity and the N_H have a weak influence in the K-correction: at the median redshift and temperature of the high-z sample, using a higher value for the metallicity, e.g., Z/Z_{solar}=0.6, results in a decrease of the K-correction by $\approx$ 8%, and a lower N_H value of 10^{20}cm^{-2} has the marginal effect of raising the K-correction by $\approx$ 2% - see Fig. 4.6 for a description of how the K-correction varies in these parameters.

Eq. (8) thus becomes:

$$K_{[0.5-5.0]keV} = \frac{\int_{0.5}^{5.0} f_\nu d\nu}{\int_{0.5(1+z)}^{5.0(1+z)} f_\nu d\nu} \tag{4.9}$$

so that $L_X = L_{X0}/K_{[0.5-5.0]}$, where L_{X0} is the rest frame luminosity of the source. The calculated correction ratios range from a minimum of 1.5, when we clone a high temperature cluster at $z \sim 0.3$ to a final redshift of 0.7, and may reach a maximum of 4 when the cloning redshift is the largest value, i.e, 1.393. If a second temperature component related to the cluster core were considered, this would increase the K-correction by a factor of 10-20%.

4.4.2.2 Spatial rescaling

The spatial rescale that a cluster undergoes when cloned to a higher redshift corresponds to the ratio of the angular distances, $D_A = D_L/(1+z)^2$. Since the premise of this method is non-evolution of the clusters, it should be clear that the size rescale does not account for the shrinking expected when applying the cosmological factor h(z), which comes about as an intrinsic evolution of clusters. The spatial resizing was implemented with a gridding linear interpolation. Note that, as explained above, apart from the redshift resizing, no additional size scaling of the kind of Eq. (2) was applied, as we compare the cluster cores in physical units.

To illustrate this method, we show, in Fig. 4.7, an example of cloning. We clone A2163, a non-cool core cluster at z=0.2, to redshifts 0.7 and 1.0. The observed high-z clusters at the same redshifts (RXJ1221 at z=0.7 and CLJ1415 at z=1.0) are displayed in the lower panels. The simulated X-ray images were normalized to have an identical number of counts as the corresponding high-z distant clusters, and the same background, which were measured as described in Sect. 2.

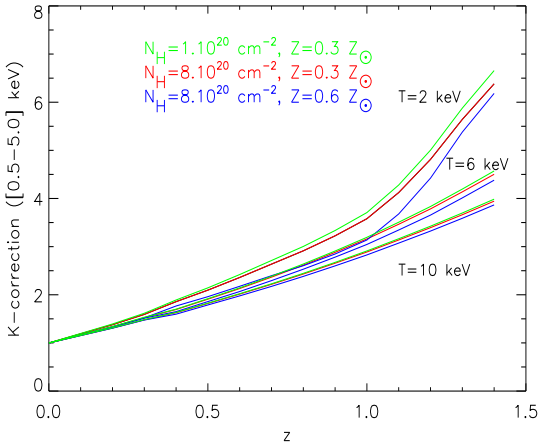

Figure 4.6: K-correction ratios computed with a MEKAL model: we show the dependence on redshift for temperatures [2,6,10]keV. Red lines refer to an N_H of 8×10^{20} cm^{-2} and a metallicity of 0.3 solar; blue lines refer to $N_H = 8 \times 10^{20}$ cm^{-2} and Z/Z$_{solar}$=0.6; and green lines refer to $N_H = 1 \times 10^{20}$ cm^{-2} and Z/Z$_{solar}$=0.3.

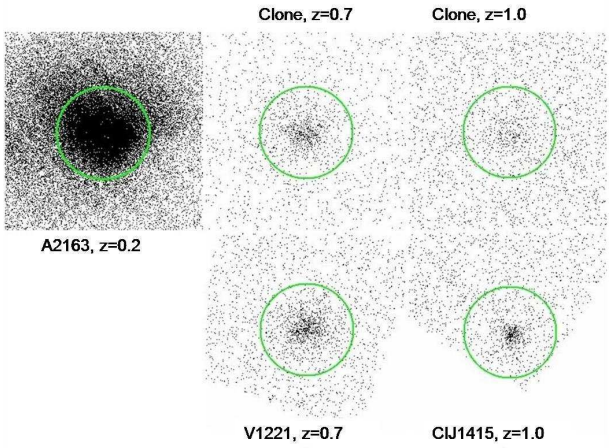

Figure 4.7: Cloning example: Chandra image of low-redshift non-CC cluster, A2163, and 2 cloned images (top), compared with a non-cool core cluster at z=0.7, RXJ1221 (bottom left), and a CC cluster at z=1.0, CLJ1415 (bottom right). Green circles have a radius of 2 arcmin.

A simple consistency check, which allows us to evaluate the procedure resides in measuring the surface brightness within a physical aperture, both in the real and

simulated image. For a given energy band we should obtain a ratio of the integrated flux which scales as follows:

$$\frac{S_X(z_i)}{S_X(z_f)} = \frac{(1+z_f)^4}{(1+z_i)^4} K_{corr} \tag{4.10}$$

We recover perfect agreement of the results from the two approaches (within the expected numerical errors).

4.4.3 The c_{SB} distribution

We find a very good agreement between the surface brightness concentration of the clones and the parent (low-z) c_{SB} distribution, implying no redshift dependence in c_{SB}. This can be exemplified by making 10 realizations of cloning the complete nearby sample to $0.7 \leq z < 1.4$ and computing the ratio $c_{SB}[clones]/c_{SB}[low-z]$ as a function of redshift. This is illustrated in Fig. 4.8: the ratio of c_{SB} randomly fluctuates around one with no trends in redshift, which is confirmed by the weighted mean linear fit to the data. Moreover, no dependence with temperature was found. This indicates that c_{SB} is an unbiased quantity which can be applied to the real high-z sample, therefore we can safely compare the nearby with the distant samples using c_{SB}.

The distribution of c_{SB} for both the nearby and distant cluster samples is presented in Fig. 4.9: the histogram of the low-z sample is shown in blue with the CCC in blue-hatched and the high-z sample is represented in red. A Kolmogorov-Smirnov (KS) test yields a probability of 45% that both c_{SB} distributions were drawn from the same population, implying there is no significant difference between the two samples with respect to the c_{SB} parameter. We measured c_{SB} by performing aperture photometry in central regions enclosing 40 and 400 kpc. Errors were determined using Poisson statistics - see Table 4 for a listing of these values.

4.5 Stacked SB profiles in bins of c_{SB}

Owing to the low number of counts of the distant cluster sample, we resorted to stacking the scaled SB profiles that we computed in Sect. 3.1, making use of the c_{SB} results (Table 4). From Fig. 4.9, we define three categories of cool cores: non-CC ($c_{SB} < 0.075$), moderate ($0.075 < c_{SB} < 0.155$), and pronounced ($c_{SB} > 0.155$) CC.

Figure 6.15 shows the stacked profiles of both samples scaled according to the empirical scaling law, in units of R_{500}. At high-z we are limited by the spatial resolution of Chandra up to $0.03 \times R_{500}$, and at low-z we are constrained by the background and cluster size to probe regions up to $0.5 \times R_{500}$ (with the exception of A2104, which can be traced only as far as $0.3 \times R_{500}$). We excluded the clusters with

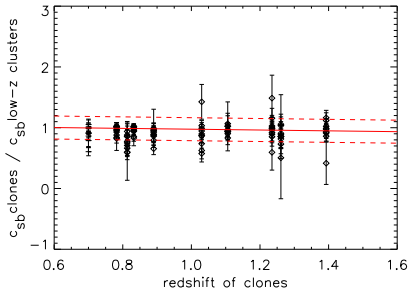

Figure 4.8: Analysis of 10 realizations of cloning the nearby cluster sample to high-z: we plot the ratio $c_{SB}[clones]/c_{SB}[lowz]$ as a function of cloning redshift. Individual error bars refer to 1-sigma confidence level. The red-solid line represents the linear fit to the data and corresponding 1-sigma errors are shown in dashed line.

Table 4.4: Surface brightness concentration, c_{SB} of the nearby and distant samples

Low-z ID	c_{SB}	High-z ID	c_{SB}
A1413	0.095 ± 0.001	RXJ1221+4918	0.028 ± 0.004
A907	0.169 ± 0.002	RXJ1113-2615	0.095 ± 0.012
A2104	0.044 ± 0.001	RXJ2302+0844	0.072 ± 0.009
A2218	0.042 ± 0.001	MS1137+6625	0.096 ± 0.007
A2163	0.024 ± 0.002	RXJ1317+2911	0.123 ± 0.030
A963	0.101 ± 0.002	RXJ1350+6007	0.057 ± 0.012
A2261	0.111 ± 0.003	RXJ1716+6708	0.082 ± 0.010
A2390	0.120 ± 0.001	MS1054-0321	0.016 ± 0.002
A1835	0.236 ± 0.003	RXJ1226+3333	0.083 ± 0.011
ZwCl3146	0.217 ± 0.003	CLJ1415+3612	0.151 ± 0.015
E0657	0.017 ± 0.001	RXJ0910+5422	0.101 ± 0.021
		RXJ1252-2927	0.088 ± 0.014
		RXJ0849+4452	0.099 ± 0.023
		RXJ0848+4453	0.064 ± 0.030
		XMMUJ2235-2557	0.103 ± 0.012

complex morphology due to mergers (E0657 at low-z and MS1054 at high-z) from the stacking procedure because they introduce strong deviations from the average profile. These deviations which are related to the difficulty of identifying the cluster center. The stacked profiles exhibit different shapes (slope and central emission) consistent with Fig. 4.9, where the low-z sample spans over 3 bins of c_{SB} whereas the high-z sample covers the first 2. Both the low- and high-redshift profiles are in

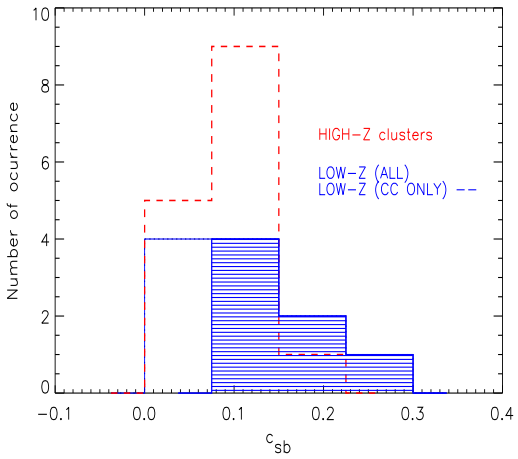

Figure 4.9: Histograms of c_{SB} for the low-z sample (blue solid line with the known CC clusters indicated in hatched) and for the high-z sample (red dash line).

full agreement on the outskirts at $r \approx 0.3 \times R_{500}$ (the deviation of the high-z NCC profile (bin1) at large radius is mostly due to the noise of the individual profiles), but not at the centers where we find a central emission offset: at $r/R_{500} = 0.03$ the SB of bin1 is 0.023±0.005 and 0.014±0.006 cts/s/$arcmin^2$ for the low-z and high-z samples, respectively, with a ratio SB(low-z)/SB(high-z)=1.6. At the same radius the offset is larger for the second bin: SB=0.089±0.026 cts/s/$arcmin^2$ for nearby clusters and 0.029±0.019 cts/s/$arcmin^2$ for distant clusters, with a corresponding ratio of 3.0. The quoted errors refer to the standard deviations associated with the stacking process, which are larger than the combined measurement errors.

The central surface brightness clearly does not follow the expected predictions from scaling relations. As mentioned above, it may be more meaningful to compare the physical state of the ICM directly, thus dropping the temperature and redshift ($h(z)$) scaling. In this case, we obtain a closer match between the low-z and high-z profiles, indicating that the physical conditions are similar.

4.6 Cooling time analysis

The radiative cooling of the intracluster gas originates mainly from thermal bremsstrahlung emission, with additional line and recombination radiation. The cooling time is defined as $dt/dlnT_{gas}$ (Sarazin (1988)) and allows the evaluation of the cooling rate in galaxy clusters. Adopting a gas enthalpy model for the cooling function, t_{cool} can be

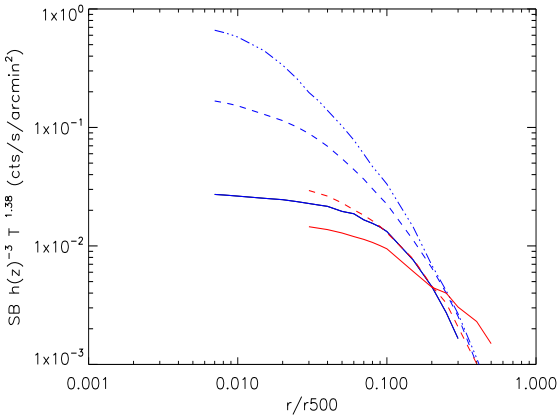

Figure 4.10: Stacked surface brightness profiles according to c_{SB} bins: the nearby sample (blue) presents 3 bins: non-cool core (solid, bin 1), moderate CC (dash, bin 2), and strong CC (dash-dot, bin 3); the distant sample (red) shows 2 bins: non-cool core (solid, bin 1) and moderate CC (dash, bin 2).

approximated by:

$$t_{cool} = \frac{2.5 n_g T}{n_e^2 \Lambda(T)} \tag{4.11}$$

where $\Lambda(T)$, n_g, n_e and T are the cooling function, gas number density, electron number density and temperature respectively (Peterson & Fabian 2005), and with n_g=1.9n_e. The central cooling time is a sensitive parameter to characterize a cool core: when a cool core forms, the central temperature decreases and conversely the central density increases, resulting in a small cooling time. Thus, we expect that CCC present cooling times shorter than the Hubble time or the time since the last major merger event.

4.6.1 Density profiles

Gas density profiles were obtained by deprojection of the surface brightness profiles. We corrected the gas density for the cosmological expansion: attending the $M_{gas} - T$ and $R - T$ scaling relations (Arnaud et al. 2005a) it follows that n_{gas} should be scaled by $h(z)^{-2}$ to account for the more compact shape of distant clusters. The density profiles of both cluster populations are presented in Fig. 4.11. Similar to what we found earlier in the scaled surface brightness profiles, the high-z density in the core region is also systematically lower than the central low-z gas density. This should be due to the h(z) scaling, as explained earlier in Sect. 5.

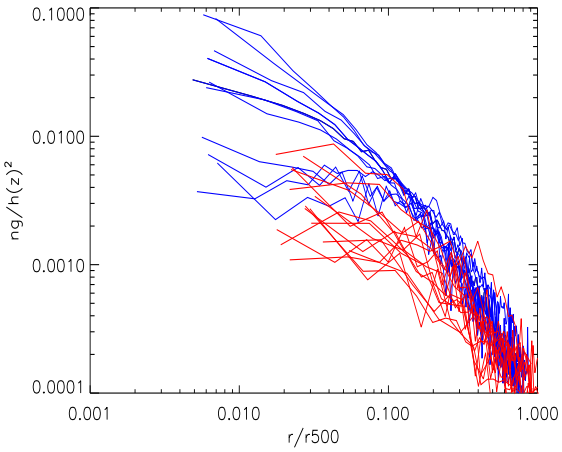

Figure 4.11: Scaled density profiles: low-z (blue) and high-z (red) clusters

4.6.2 Cooling time at r=20 kpc

The cooling time was measured within a central aperture of 20 kpc radius extrapolating the density profiles with a 1β model. We found it preferable to use an aperture with a fixed physical radius for a consistent analysis of all clusters, as we are limited by the instrument's resolution at high redshift. Using a fraction of a scaled radius was not suitable as the redshift range is fairly large, and therefore we would probe larger areas at low redshift, introducing a bias. As a result, the strong cool cores would have a (artificially) boosted cooling time by a factor $\sim$ 2-3.

Since temperature profiles cannot be derived from high-z data, we used the spectral fit temperature in the single temperature (MEKAL) model for the cooling time computation. As a result, the t_{cool} values in this case are an upper limit because in the presence of cool cores the central temperature would be lower, decreasing the cooling time.

The cooling time distribution is plotted in Fig. 4.12 and presented in Table 5; we obtained errors from the propagation of the errors on the temperature and ng. Four low-z clusters (A1835, ZwCl3146, A2390 and A907) present a cooling time < 3 Gyrs and the 4 nearby non-CC show a $t_{cool} > 10$ Gyrs. At high-z there is no system with $t_{cool} < 3$ Gyrs, although the majority (11/15) has $t_{cool} < 10$ Gyrs, with only 4 clusters presenting a $t_{cool} > 10$ Gyrs.

While similar cooling times or cooling rates in the nearby and distant samples point to similar physical conditions in the central cluster regions, the different ages of the clusters lead to some different conclusions of these results. The cooling rates for more than half of the nearby clusters are shorter than their estimated ages ($\sim$10 Gyr)

which implies that they approach a steady state of cooling, some mass deposition, mass inflow and reheating by central AGN. With the same cooling time distribution, only a small fraction of the distant clusters (with ages between 5-8 Gyr) will have a chance to reach this steady state. If we therefore use the classical definition of cooling flows in which $t_{cool} < t_{age}$ also for the distant clusters, we find that the fraction of CCs is 4/15, which is significantly smaller than the ratio found for nearby clusters (e.g., Peres et al. (1998); Bauer et al. (2005); Chen et al. (2007)).

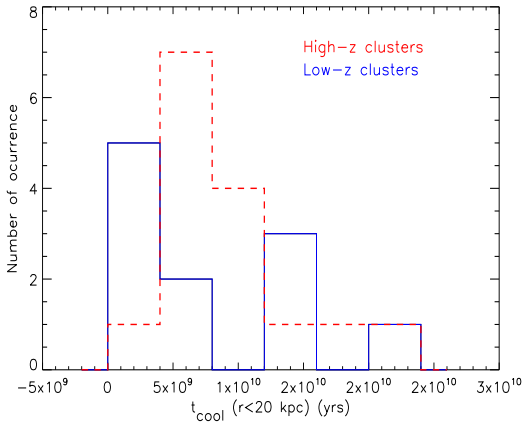

Figure 4.12: Distribution of the cooling time, t_{cool}, in the low-z (blue) and high-z (red) samples.

4.6.3 The correlation t_{cool} - c_{SB}

As we are interested in evaluating the degree of cooling of the central intracluster gas with a simple function that can be deduced from imaging data only, we investigated the relation between the cooling time and the surface brightness concentration. We found a strong negative correlation with a Spearman's ρ rank correlation coefficient of -0.84 and a significance of non-correlation $p = 8.15\text{x}10^{-8}$. Using 1000 bootstrap samples, we performed a linear fit in the log-log plane of t_{cool} and c_{SB}, from which we derived an average slope of the power-law function that describes the correlation between the two cooling estimators. A composite fit to both cluster samples yields $t_{cool} \propto c_{SB}^{-1\times10\pm0.15}$, (Fig. 4.13). Fitting the nearby and distant samples separately yields the following correlations: $t_{cool}(high_z) \propto c_{SB}^{-0.92\pm0.26}$ and $t_{cool}(low_z) \propto c_{SB}^{-1.16\pm0.14}$.

Using the single fit correlation we obtain the cooling time at the reference thresholds $c_{SB} = 0.075$ and $c_{SB} = 0.155$, as 6.9 Gyrs and 3.1 Gyrs, respectively.

Table 4.5: Cooling time, t_{cool} measured at 20 kpc, of the nearby and distant samples

Low-z ID	t_{cool} (Gyr)	High-z ID	t_{cool} (Gyr)
A1413	$5.50^{+0.23}_{-0.17}$	RX J1221+4918	$20.60^{+4.55}_{-4.61}$
A907	2.91 ± 0.10	RX J1113-2615	$7.01^{+1.75}_{-1.38}$
A2104	15.10 ± 0.99	RX J2302+0844	$14.70^{+3.85}_{-3.67}$
A2218	12.10 ± 1.22	MS1137+6625	$6.38^{+0.86}_{-0.83}$
A2163	$15.10^{+2.06}_{-1.81}$	RX J1317+2911	$8.77^{+4.17}_{-3.36}$
A963	$4.52^{+0.32}_{-0.26}$	RX J1350+6007	$10.90^{+3.65}_{-3.24}$
A2261	$3.89^{+0.38}_{-0.26}$	RX J1716+6708	$6.39^{+1.34}_{-1.25}$
A2390	2.67 ± 0.07	MS1054-0321	$16.70^{+3.25}_{-2.43}$
A1835	1.13 ± 0.09	RX J1226+3333	$4.11^{+0.88}_{-0.83}$
ZwCl3146	1.32 ± 0.08	CL J1415+3612	$3.90^{+0.72}_{-0.71}$
E0657	20.80 ± 1.62	RX J0910+5422	$8.65^{+3.11}_{-2.71}$
		RX J1252-2927	$7.35^{+2.01}_{-1.78}$
		RX J0849+4452	$9.02^{+4.12}_{-3.11}$
		RX J0848+4453	$6.19^{+7.87}_{-4.00}$
		XMMU J2235-2557	$4.84^{+2.38}_{-1.82}$

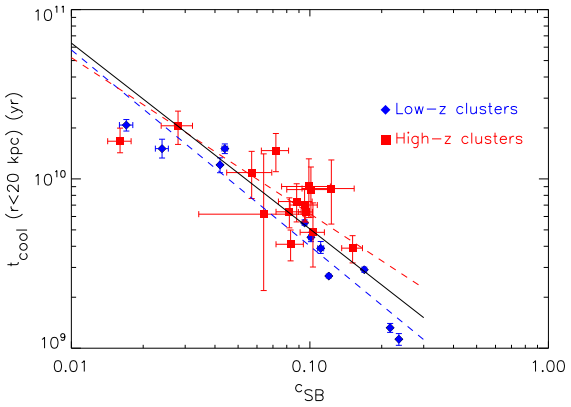

Figure 4.13: Correlation between cooling time, t_{cool} and the surface brightness concentration, c_{SB}, for the low-z (blue diamonds) and high-z (red squares) samples. The black-solid line refers to the composite (both populations) bootstrap fit; the blue- and red-dashed lines refer to separate fits to the nearby and distant samples, respectively.

4.7 Comparing X-ray and Optically selected distant clusters with c_{SB}

In this section, we briefly analyze the X-ray surface brightness properties of distant galaxy clusters detected in the optical. Specifically, we evaluate the degree of cooling using the previously defined c_{SB} parameter and compare this degree with the results obtained for the X-ray selected high redshift sample.

The Red Sequence Cluster Survey (RCS) aims at finding and characterizing distant galaxy clusters using R and z-band imaging, up to redshift z=1.4 (Gladders & Yee (2000)). Selecting clusters in the optical allows us to study high redshift poor systems with low temperature, which are usually not found in flux limited samples restricted to high L_X objects at high redshift.

Although there are indications of a large scatter in the $L_X - T$ relation of the RCS sample, such clusters with low temperature (median T = 5 keV) enable us to probe a larger dynamical range in the $L_X - T$ relation.

The connection between optical and X-ray characteristics of these distant clusters has been under investigation (Hicks et al. (2008)). Currently, 11 clusters with $0.6 < z < 1.2$ have been observed with Chandra and X-ray properties as temperature and luminosity have been derived (Hicks et al. (2008); Bignamini et al. (2008)). We based our analysis on Chandra images reduced by Bignamini et al. - see Table 2 for an overview of the sample.

We find that 3 of the 11 RCS clusters are barely detected in X-rays and have such a low surface brightness that a c_{SB} analysis is not possible. The measurement of the surface brightness concentration as described in Sect. 4.3, yields that the majority (6 of 8) of the RCS clusters with measurable X-ray emission have $c_{SB} < 0.075$, thus falling in the non-CC regime. Of the remaining two: RCS1107 has a $c_{SB} = 0.143$ indicating a moderate CC, and RCS1419 has $c_{SB} = 0.185$, suggesting a strong CC (see histogram in Fig. 4.14). The c_{SB} distribution of the X-ray distant clusters is overplotted in the same figure (red line) for direct comparison. The Kolmogorov-Smirnov statistic between the two c_{SB} distributions is 0.4, with a probability of the samples being drawn from the same distribution of 20%. With such low statistics, the KS test does not provide a sensitive distinction on these two datasets.

The outcome of this analysis, based on our small samples suggests that high-z optically selected clusters may have a lower fraction of cool cores with respect to clusters detected in X-rays. Larger samples are needed to draw conclusions on possible different physical conditions of the ICM in optically-selected clusters, which may have not reached a final state of virialization

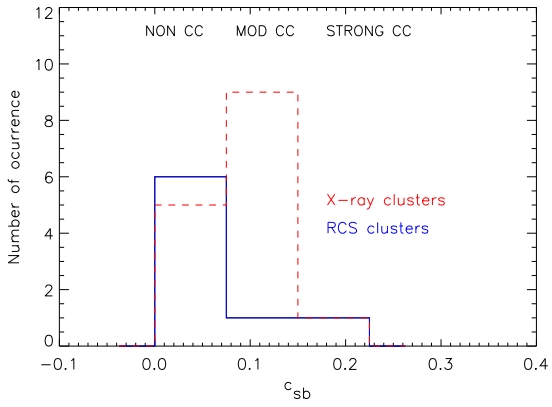

Figure 4.14: Histogram of c_{SB} for the RCS sample in solid blue line; the high-z X-ray sample is overplotted in red dashed line.

4.8 Discussion and Conclusions

In this paper we investigate the detection and quantify the strength of cool cores in the high redshift cluster population. We obtained azimuthally-averaged SB profiles and scaled them, in this manner accounting for different cluster temperatures. The segregation of cool cores at low redshift using this method is evident in Fig. 4.3 (top panels). However, this segregation is not obvious in the distant sample, and the use of single/double β model fitting does not provide conclusive results.

A surface brightness concentration index, c_{SB}, was then defined and measured in the local sample, which efficiently separates the non-cool core from the cool core regime. This is in agreement with previously published results on the cuspiness of these clusters. In Hashimoto et al. (2007), a similar surface brightness concentration was defined, using the ratio of elliptical aperture radii enclosing, respectively, 30 and 100 % of the cluster surface brightness. This parameter was applied to a sample of 101 clusters with $0.05 < z < 1$, these including 4 of the 11 nearby clusters and 12 of the 15 distant clusters we study here. Comparing the results from both measurements for individual clusters we find a good agreement with our results, with the exception of A1835.

We also developed a robust, parameter-free method to simulate galaxy clusters at redshift $z \geq 0.7$, making use of the heterogeneous nearby ($0.15 < z < 0.3$) sample. These simulated clusters serve as a benchmark for nonevolving clusters, which allow us to test the suitability of indicators of cool cores at high redshift. Using our cloning technique, we verified the redshift independence of c_{SB}, thus making it a simple, unbiased quantity to study cool cores in the distant cluster sample (Fig. 4.9). The analysis of the concentration and radial profiles allows us to define three c_{SB} bins,

which distinguish different regimes: non-CC ($c_{SB} < 0.75$), moderate CC ($0.75 < c_{SB} < 1.55$) and strong CC ($c_{SB} > 1.55$). By stacking the profiles in these bins (Fig. 6.15), we obtained a robust classification of cool cores, indicating the range of different cooling rates the two cluster samples span. This is particularly useful for the distant sample that is affected by low X-ray count statistics.

From the overall surface brightness analysis we conclude that the majority (10/15) of the high-z clusters present mild cool cores, similar to those found in the nearby sample. In addition to the surface brightness analysis, we measured the clusters' cooling time in a central region with 20 kpc radius, using a single global temperature. Analyzing the reference, low-z sample, we conclude that strong cool cores present $t_{cool} < 3$ Gyrs, whereas moderate CC have $3 < t_{cool} < 10$ Gyrs and finally non-CC show $t_{cool} > 10$ Gyrs. The majority (11/15) of the high-z clusters are characterized by $3 < t_{cool} < 10$ Gyrs with only 4 systems showing $t_{cool} > 10$ Gyrs. We found no distant clusters with $t_{cool} < 3$ Gyrs. Similar cooling time bins were provided by Bauer et al. 2005, to discriminate between strong, mild and non-cool core systems. These authors measured the central cooling time and also the cooling time at 50 kpc: good agreement on their t_{cool} at 50 kpc and our t_{cool} at 20 kpc is found for the common objects in the intermediate-z sample of Bauer et al. (2005) (4/6 objects within 1σ errors). Although the distribution of the cooling time is quite similar in the nearby and distant samples, a smaller fraction of distant clusters has $t_{cool} < t_{age} \sim t_{Hubble}$, and therefore the fraction of distant CCs following the classical cooling flow distribution is smaller than for local clusters.

We find a strong correlation between t_{cool} and c_{SB}, which allow us to reliably relate a physical quantity with a phenomenological parameter. This correlation is described by a power-law fit: $t_{cool} \propto c_{SB}^{-1\times10\pm0.15}$ (Fig. 4.13). The correlation does not change significantly if we fit the two samples separately. The low-z clusters show a slightly steeper slope (-1.16 ± 0.14) when compared with the high-z slope (-0.92 ± 0.26).

Investigating galaxy cluster properties at high redshift is difficult as these systems have small angular size, requiring high resolution instruments and long integration time, particularly for spectroscopy. It is, therefore, understandable that few attempts have been made to probe the centers of distant galaxy clusters. Vikhlinin et al. 2006 presented a study on the evolution of CCC in the redshift range [0.5-0.9], which they compared to a local sample. They found evidence for evolution of the CC fraction, with a lack of cool cores in the distant sample. They use a different indicator for the surface brightness cuspiness, which might have a lower sensitivity to moderate cool core systems. A meaningful comparison with our study would require a detailed analysis of the different cool core estimators.

One often finds that massive, luminous galaxies containing AGN, lie at the centers of cool core clusters (Eilek (2004)). In an attempt to establish such a correlation we searched for cD galaxies in the cluster samples, examining available optical images. We find that, in the low-z sample, all CCC indeed host a bright, massive galaxy, but

also A2104, a non-cool core cluster, possesses a cD galaxy with an associated AGN (Liang et al. (2000); Martini et al. (2004)). Could this be a sign of an AGN heating overshoot that could have contributed to destroy the cool core? At high redshift there is no obvious trend: the majority of the clusters possess a cD galaxy but it does not correlate with c_{SB}.

In the established scenario of hierarchical structure formation, galaxy clusters develop through mergers and by accretion of neigboring smaller objects. Numerical simulations (Cohn & White (2005)) predict higher cluster merger rates with increasing redshift, where the fraction of clusters with recent mass accretion due to mergers can be doubled at z=0.7, with respect to the local abundance. This framework provides a possible mechanism for preventing the formation of prominent cool cores at high redshift. However, since high-z clusters are younger, other mechanisms may cause a delay in the formation of cool cores due to some internal energy release, such as AGN activity and star formation processes. The observed absence of pronounced CC at $z \geq 0.7$ is therefore plausible in the current cosmological framework.

We also investigated possible sample selection effects in the search for high redshift cool cores by studying 11 optically-selected clusters from the RCS sample, which have a median temperature of 5 keV. We found that, unlike the X-ray sample, the majority of clusters in the RCS subsample have $c_{SB} < 0.075$, i.e., they lie in the non-cool core category.

To further extend this analysis we need to construct a complete low redshift sample, possibly with the same selection function as the distant sample, to be able to trace the evolution of the abundance of cool cores. A good prospect for this study is the local representative cluster sample XMM-Large Programme (Böhringer et al. (2007)), which comprises 33 clusters in the redshift range z=0.055 to 0.183, drawn from the REFLEX sample (Böhringer et al. (2001)). An intermediate redshift sample (z=0.3-0.6) from a similar project is also available (P.I. M. Arnaud), which provides an intermediate step in the assessment of the cool core evolution with redshift.

Clearly, having a high-z data set covering a larger volume would also be very advantageous. Serendipitous cluster surveys currently underway, such as the XCS (Romer et al. (2001)), the XDCP (Mullis et al. (2005); Böhringer et al. (2005)) and XMM-LSS (Pierre et al. (2006)), will yield suitable distant samples for these studies in the near future.

A comparison of our results with cosmological simulations would also provide additional new constraints to cluster formation scenarios. In fact, new insights on the evolution of simulated CCs and NCCs have recently been published in Burns et al. (2008), which are in good agreement with our findings.

Acknowledgements

We would like to thank A. Baldi for giving access to the low redshift Chandra data. JSS thanks Y-Y. Zhang, G. Pratt, D. Pierini and I. Balestra for useful discussions. JSS is supported by the Deutsche Forschungsgemeinschaft under contract BO702/16-2. PT and SE acknowledge the financial contribution from contract ASI-INAF I/088/06/0.

Appendix: a test case for the cloning technique

To further demonstrate the potential of the cloning technique in simulating realistic galaxy clusters, we applied this method in a modest attempt to qualitatively evaluate the detection of high-z clusters in an eROSITA-like configuration.

We consider the following eROSITA parameters in the 4-year all-sky survey mode (7 telescopes):

- Field of View = 1 $\deg^2$
- pixel scale = 9.67"/pix
- average exposure time = 2440 sec
- energy range = [0.5-2.0] keV
- background=0.146 cts/pix
- psf modelled with a gaussian with 25" FWHM
- flux limit: $f_X > 10^{-14}$ erg/s/cm^2

We construct a mock eROSITA background field based on the *XMM-Newton* COSMOS catalog of point sources (from A. Finoguenov), since the *XMM-Newton* survey of the COSMOS field (2 Msec exposure, Hasinger et al. (2007)) is to date the deepest wide field X-ray survey performed. The survey covers an area of 2 $\deg^2$ and reaches a sensitivity of $\sim 10^{-15}$ erg s^{-1} cm^{-2}, making this a small-scale precursor of eROSITA.

Point sources are modelled with a gaussian kernel matching the instrument's PSF. Ten high-z clusters are expected to be found in an area of 1 $\deg^2$, as derived from the logN-logS in Rosati et al. (2002). Therefore we clone 10 low-z *Chandra* clusters to redshifts $0.7 < z < 1.2$, with X-ray luminosities spanning $\sim$1-14.10^{44} erg/s (values taken from the high-z sample described in Sect. 4.2.2) and add them to the background image, assuming a Poisson distribution of the photons. Energy conversion factors are computed with response matrices from P. Friederich (priv. communication). The cloned image stamps are convolved with the PSF of eROSITA, by applying a gaussian filter.

Using realistic cluster morphologies has the advantage of covering a wide range in surface brightness (CCs, non-CCs), which would not be evident in β-models. Peaked clusters are potentially a matter of concern in the detection of very distant and hence small clusters, since the instrument's PSF is broad and the pixel scale is large, leading to a smearing of the cluster.

The mock eROSITA image is presented in Fig. 4.15.

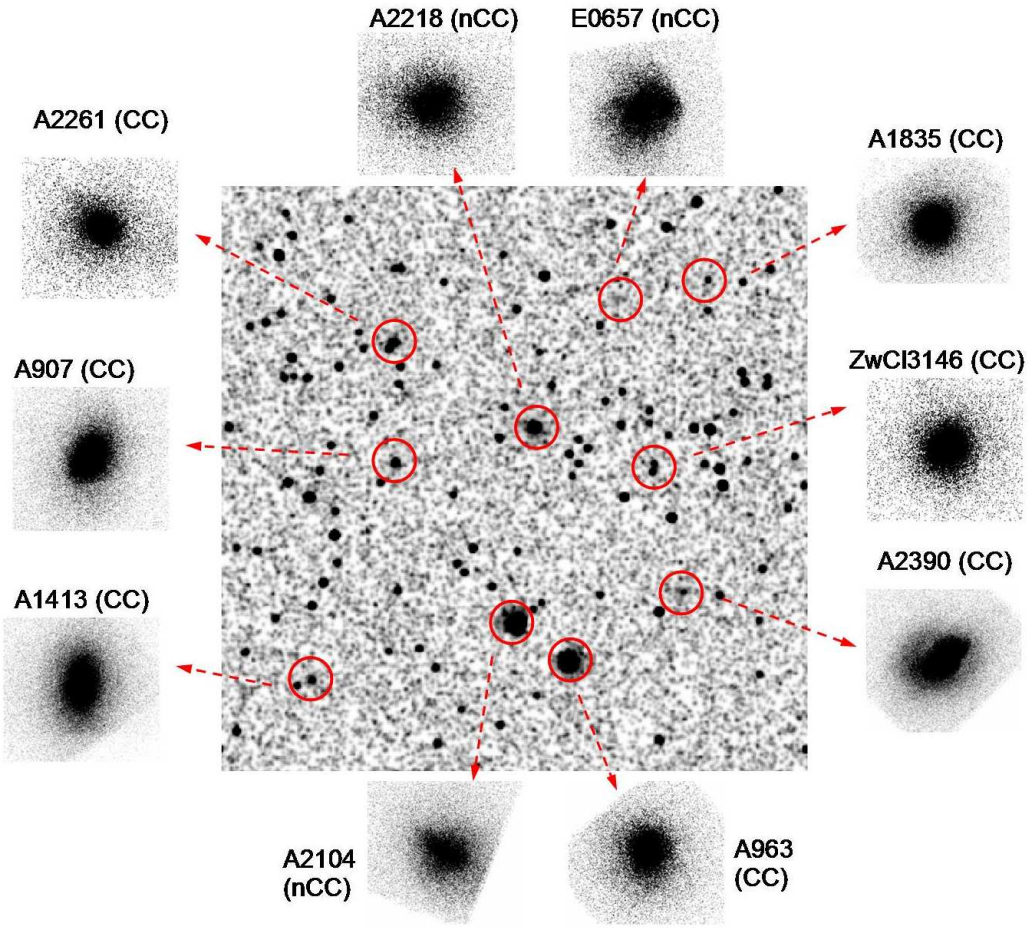

Figure 4.15: Mock eRosita image (1 deg^2, exposure time=2.4 ksec) based on the point source catalog of the COSMOS field, with added clones marked in red circles. The corresponding *Chandra* low-z templates are also shown for comparison in 8x8 armin stamps. The image is smoothed with a gaussian kernel of 1.

Expected cluster counts

We also investigate the expected cluster counts in an eROSITA configuration by cloning the complete *Chandra* local sample to redshifts z=[0.7, 1.0]. Given an input rest-frame X-ray luminosity, we apply a K-correction corresponding to the cloning redshift, obtaining an unabsorbed flux and therefore the expected cluster net counts - see Table 4.7. Since we can expect to detect only the most massive distant clusters, we focus on the bright end of the X-ray luminosity in this test. We find that, clusters with redshift 1.0 will be detected with 50 to 260 counts in this range of luminosities,

Table 4.6: Cloning parameters referring to Fig. 4.15: clone ID; cloning redshift; rest-frame luminosity in erg/s; expected total net counts.

Clone ID	**z**	$\mathbf{L}_X(10^{43})$	**cts**
A1413	0.81	8	37
A907	1.03	33	84
A2104	0.70	70	462
A2218	0.81	19	194
A963	0.89	138	503
A2261	1.03	33	84
A2390	0.81	8	37
A1835	1.24	19	31
ZwCl3146	1.11	20	42
E0657	1.24	19	31

whereas the z=0.7 clusters will be detected with almost a factor 2 higher net counts.

Table 4.7: Net counts of cloned low-z sample to redshifts 0.7 / 1.0 as measured in a mock eROSITA image for various input cluster rest-frame luminosities.

Clone ID	$\mathbf{L}_X = 5.10^{44}$	$\mathbf{L}_X = 10^{45}$	$\mathbf{L}_X = 2.10^{45}$
A1413	93 / 52	186 / 104	373 / 208
A907	96 / 52	192 / 104	384 / 208
A2104	96 / 53	191 / 105	382 / 211
A2218	99 / 55	198 / 109	395 / 219
A2163	100 / 58	200 / 115	400 / 231
A963	102 / 58	204 / 115	409 / 231
A2261	103 / 59	207 / 118	414 / 237
A2390	105 / 59	210 / 119	421 / 238
A1835	106 / 62	211 / 123	422 / 246
ZwCl3146	90 / 52	180 / 104	359 / 208
E0657	113 / 66	227 / 131	454 / 263

5

Optical and NIR follow-up of the XMM-Newton Distant Cluster project

Abstract

In this Chapter, the XMM-Newton Distant Cluster Project is introduced, and a summary of the main scientific results obtained so far with this survey is presented.

Two observing runs were carried out in 2007 at ESO/NTT to extensively collect imaging data in the NIR (SOFI) and optical (EMMI), to follow-up 36 X-ray selected cluster candidates. We explored a new I-H photometric technique, and we present the data reduction, as well as the visual evaluation of 22 cluster candidates, based on their I-H color images. In addition, we show the color-magnitude diagram of a potential z$\sim$1 cluster, where the red-sequence is clearly visible.

5.1 Goals and general description of the XDCP

As mentioned in the introductory Chapter 2, at high-redshift we face a lack of confirmed X-ray clusters. Distant clusters are not detectable with sufficient contrast in the projected galaxy distribution without advanced techniques of color selection, hence very good multi-color data are needed to detect the distant clusters as galaxy overdensities. In addition, large survey volumes are needed to find clusters. This makes distant cluster surveys expensive, at least for current instruments with limited FoV and sensitivity. Therefore, a large effort needs to be dedicated to efficiently select distant cluster candidates.

The XMM-Newton Distant Cluster Project (Böhringer et al. (2005)) aims at constructing a statistically significant sample (with ∼40) of distant clusters in the redshift regime $z \sim 1$. The main objectives of this programme are (i) to characterize the evolution of cluster properties by meaningful distribution functions with at least 20 objects and (ii) to obtain constraints on the cluster abundance evolution at high redshift. This survey is based on the serendipitous detection of clusters using XMM-Newton archival data, selecting fields with low Galactic absorption at a safe distance from the Magellanic Clouds and with a minimun exposure time of 10 ksec. In total, 469 fields have been successfully proccessed and analysed, covering an area of about 50 deg^2. The survey is sensitive down to an average flux limit of approximately 10^{-14}erg s^{-1} cm^{-2}.

The source detection method (see the dissertation of Fassbender (2008), for a comprehensive description) is based on the sliding box and subsequent maximum likelihood technique. A final catalog with ∼250 distant cluster candidates was released in Fassbender (2008). The first filtering process of the candidates consists in searching for nearby visible counterparts in the Digitized Sky Survey (DSS). Since the DSS is sensitive to overdensities of galaxies up to z∼0.5 we do not expect to visually identify a distant ($z \gtrsim 1$) cluster in the DSS.

The follow-up observations of cluster candidates are, in a first stage, NIR and optical imaging, and afterwards optical spectroscopy. The two-band photometry data are used to distinguish medium distant clusters from the high-redshift target cluster candidates ($z \gtrsim 0.9$). Two photometric strategies were explored in this project: the I-H color (which will be discussed in detail in the next section) and the z-H photometry. The latter option is extensively described in Fassbender (2008) and was used in observations at the Calar Alto Observatory.

Spectroscopy is the final step necessary to confirm a cluster's redshift and this is the most expensive and time-consuming observations to obtain. Therefore, a good strategy in imaging is required to efficiently use spectroscopic time.

5.2 First results of the XDCP

The pilot project conducted in 2003/2004 has yielded the discovery of the most distant cluster known at the time, XMMU J2235.3-2557 at z=1.393 (Mullis et al. (2005)). This cluster (Fig. 5.1) was detected in X-rays with 280 counts and was further observed with VLT/FORS2, HST/ACS, Spitzer, Chandra (Rosati (2008)) and HAWK-I (Lidman et al. (2008)) . The Chandra X-ray analysis and ACS weak lensing studies indicate this is one of the hottest, most massive high-z clusters known. XMMU J2235.3-2557 appears to be surprinsingly relaxed, even likely to have developed a cool core (Santos et al. (2008)). Furthermore, the study of its galaxy population shows a well defined red sequence (Rosati et al. 2008) with a clear BCG.

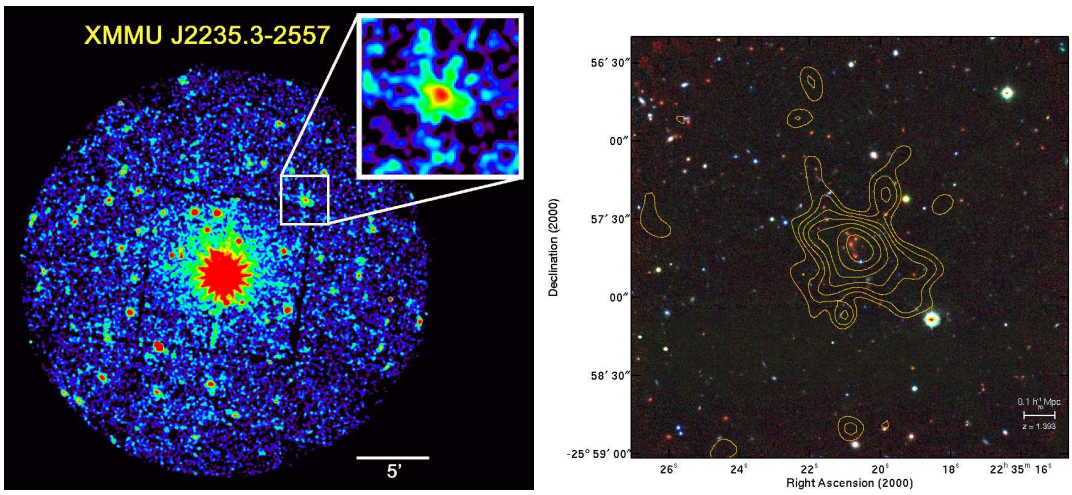

Figure 5.1: *Left* XMM-Newton discovery image of XMMU J2235.3-2557. *Right* Ks+Z+R color composite image with X-ray contours overlaid.

The discovery and analysis of a massive, X-ray lumninous cluster at redshift z=0.976, XMMU J1229+0151 will be discussed in detail in Chapter 6.

Two clusters at redshift z∼0.95 indicate the existence of a large-scale structure with 3 Mpc size (Fassbender et al. (2008)). Cluster XMMUJ0104.4-0630 at z=0.947 ±0.005 is a compact and evolved system hosting a central radio source. The color-magnitude diagram shows a clear transition toward a bluer galaxy population at 1-2 core radii from the cluster center. A second cluster with photometric z=0.95±0.05 is found at a projected distance of $\sim$ 3 Mpc from the first cluster, with a CMD consistent with the one of XMMUJ0104.4-0630. There are indications for these two clusters being dynamically linked, thus forming part of the same large-scale structure.

In addition to the above mentioned clusters, this survey has detected 10 clusters with $z > 1$ (see Table 9.1 in Fassbender (2008)).

5.3 Optical and Near Infrared Follow-up procedure

My participation in the XDCP project concerns the optical and NIR follow-up of cluster candidates selected in the archival XMM-Newton observations. To this purpose

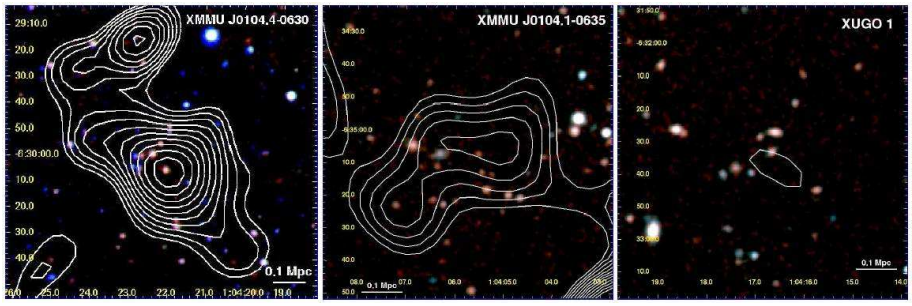

Figure 5.2: *Left* R+z+H color image of XMMUJ0104.4-0630 at z = 0.947 with white X-ray contours overlaid. *Center* z+H color composite of the second X-ray selected cluster in this field XMMUJ0104.1-0635, with a concordant redshift estimate. *Right* zoom on one of the X-ray undetected overdensities of bluer galaxies in the center of the field.

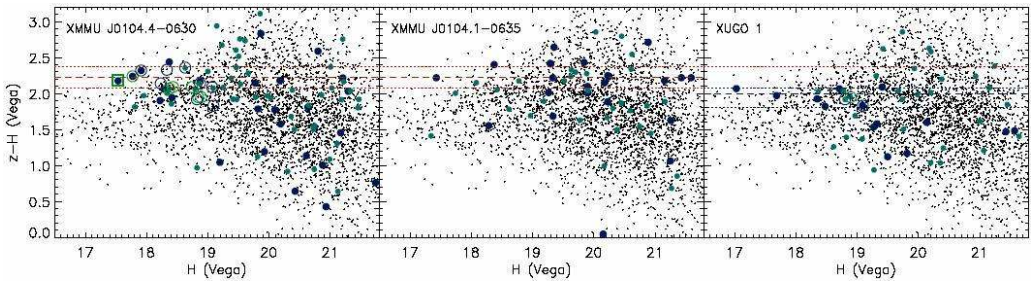

Figure 5.3: Corresponding z-H color-magnitude diagrams of the three objects shown in Fig. 5.2. *Left* and *center* CMDs of the two X-ray selected galaxy clusters with concordant red-sequence colors. Spectroscopically confirmed cluster members of XMMUJ0104.4-0630 are indicated in the left panel by open symbols. The BCG is marked by the green square, the six additional secure members by green circles, and the eight tentative cluster members by blue open circles. *Right* CMD of the galaxy overdensity between the two X-ray clusters with a bluer red-sequence color. The dashed blue line is shown at the color of the apparent object locus (Figures from Fassbender et al. (2008)).

I participated in two observing runs at the ESO/La Silla observatory (March and September 2007, hereafter P78 and P79), where we acquired NIR and optical imaging with SOFI and EMMI respectively, both at the 3.5 m New Technology Telescope (NTT).

Initial NIR imaging in H-band allows us to discriminate between nearby galaxy overdensities (based on the galaxy magnitude distribution), obvious outliers (false positives) and potential clusters with larger redshifts including the range $z \gtrsim 1$. As a reference, a M*+1 galaxy with z=1.4 will have an H-band magnitude of 20.8,

requiring 1 hour of exposure time. Our strategy was thus to make a first exposure with 30 min (depth of H ∼20.4 mag) and if a galaxy overdensity appears to be too dim - indicating a high-z population - we return the subsequent night with an additional 30 min exposure. Following this procedure, the H-band preselected objects are subsequently observed in I-band (while this is the preferred methodology, in P78 the observing time was scheduled differently, the EMMI observing time was allocated before the SOFI slot). With two-band photometry we can then derive color-magnitude diagrams that will indicate the existence of a well-defined red sequence, confirming the presence of a population of passive galaxies, and thus the confirmation of a cluster. Photometric redshifts will be derived to obtain a first estimate of the cluster redshift in a next step. The latter was beyond the scope of this thesis.

The cluster candidates have been attributed a quality flag based on the X-ray contours and DSS counterparts. Quality flags range from 1 (very good) to 4 (likely spurious source). The targets in these runs have mostly a low quality flag (2-3) as the best ones were selected to be observed in FORS2 at the VLT. However, understanding the selection efficiency of the survey close to the detection limit is crucial since this is the region where most distant cluster candidates are expected.

In both runs we observed several fields affected with very bright stars, which makes the data reduction difficult, if not impossible. The statistics on the 36 cluster candidates observed in the two runs are summarized in Table 5.2.

5.3.1 NIR observations and data reduction

SOFI (Son OF Isaac, Moorwood et al. (1998)) is a single chip Hawaii HgCdTe detector offering imaging at different pixel scales and Field of View (FoV). We chose to use the *Large field* observation mode, corresponding to a 5'x5' Field of View (FoV), with a 0.288 arsec/pixel.

The NIR background is highly variable due to strong atmospheric emission. Therefore observing in the NIR presents more difficulties than in the optical regime. In particular, the background level is high and one has to be careful when optimizing the Detector Integration Time (DIT). In the H-band the background level should be around 2500 ADU to ensure that the signal of the observed target is on the linear part of the detector's dynamical range, below 10000 ADU. Since the background presents strong temporal and spatial variations, a small dithering pattern has to be applied in order to ensure an accurate sky model. We used a jitter box with a width of 30 arcsec. Generally, we chose a DIT=15 sec in the H-band, although this was subject to the observing conditions. Each science target had 20 exposures of DIT*NDIT = 30 min.

Table 5.1: Summary of imaging targets observed at ESO/NTT: P78 in the first 21 lines up to the break, and P79 follows.

ID	RA	DEC	H-band	I-band	quality
106	05:15:53.5	+01:04:00.9	x	x	2
116c	07:51:12.4	+18:01:16.3	x	x	3
127b	10:30:24.8	+05:18:52.6	x	x	2
127c	10:44:07.8	-01:27:25.6	x	x	2
128	11:06:33.7	-18:26:48.0	x	-	3
139	11:23:39.1	+05:27:52.9	-	x	3
142	11:40:26.7	-01:47:48.8	-	x	3
146	11:50:27.7	+01:45:34.9	-	x	1
149	12:11:33.0	+13:08:49.9	x	x	2
153	12:17:24.7	-11:52:40.9	x	x	2
154	12:20:04.0	+06:31:54.9	-	x	3
156	12:30:08.3	+13:25:32.0	x	x	3
159	12:31:08.6	+16:14:04.9	x	-	3
165	12:42:50.5	+02:27:45.8	x	x	2
171	12:53:00.8	+15:33:47.0	-	x	3
173	12:53:30.7	-29:27:28.5	x	x	2
179	13:14:58.1	-16:40:03.8	-	x	3
185	13:39:48.0	-31:33:27.1	-	x	1
190	14:00:39.7	-11:05:48.8	x	-	2
192	14:48:56.8	+09:02:53.9	x	-	2
201	16:16:18.9	-05:50:55.0	-	-	3
014	00:42:03.60	-09:44:18.30	x	x	2
015	00:44:05.20	-20:33:59.70	x	x	2
015b	00:47:01.70	-25:11:11.40	x	-	2
035	01:24:14.20	03:56:31.50	x	x	2
036	01:24:40.60	03:44:15.90	x	x	2
039	01:40:43.30	06:21:48.90	x	x	3
045	02:07:30.50	02:37:29.70	x	x	3
059c	02:43:15.90	-00:08:11.20	x	x	3
083	03:57:31.80	00:59:45.40	x	x	2
209b	21:52:20.30	-27:30:24.80	x	x	2
224	22:28:28.50	-05:26:00.40	x	x	3
225b	22:35:03.10	-26:01:58.00	x	x	1
226	22:51:46.10	-18:05:48.90	x	-	3
231	23:05:09.00	03:20:46.90	x	-	2
241	23:40:40.60	-12:13:31.00	x	x	2

5.3.1.1 Photometric calibration

The NIR calibration plan comprises the following steps:

- acquire dark frames with closed shutter, accounting for the thermal behavior of the detector
- acquire twilights flats at the beginning and end of the night to obtain a map of the pixel variations inherent to the detector
- observe photometric standard stars (Persson et al. (1998)) to calibrate the magnitudes. Standards were acquired on average three times per night, to properly sample variations in the airmass.

5.3.1.2 NIR data reduction

The NIR data was reduced with the software `MVM` (Vandame (2004)), a complex multi-instrument package that performs the reduction of the calibration files (master-dark and master-flat); combines and aligns calibrated (and background-subtracted) science frames; and finally makes the astrometric calibration of the images, by automatic retrieval of public catalogs such as the GSC2 or the USNO catalogs.

The zero point (ZP) of an instrument is, by definition, the magnitude of an object that produces one ADU or count per second. The zero points were computed using the reduced standards (count rate image), using the following relation:

$$ZP(VEGA) = mag + 2.5log(countrate) + atmcorr * airmass \tag{5.1}$$

(note that an additional $2.5log(DIT)$ term would be necessary if the images were not normalized to 1 sec.)

The stellar flux was measured within a circular aperture with 6" radius; such a large radius ensures that we account for the bulk of the stellar flux. The background was estimated with a 3σ clipping algorithm. Wavelength dependent atmospheric corrections ($atmcorr$) were available in the La Silla website.[1] for the various filters; the $atmcorr$ for the H-band corresponds to 0.03 mag. Airmass values are obtained from the FITS file header.

VEGA magnitudes were converted to the AB photometric system with an online ESO tool available at `http://archive.eso.org/apps/mag2flux/`.

5.3.2 Optical observations and data reduction

EMMI (ESO Multi Mode Instrument, Dekker et al. (1986)) offers wide field imaging by means of three thin, back-illuminated, scientific CCD cameras. Two of them are

[1] http://www.ls.eso.org/lasilla/sciops/ntt/sofi/setup/Zero_Point.html

arranged in a mosaic in the red arm and one is in the blue arm. We observe in the RILD (Red Imaging and Low Dispersion Spectroscopy) mode, which is suitable for observations redder than 400 nm, using the I#610 filter.In this mode we use the two mosaic CCD cameras which have a total FoV of 9.1' x 9.9' (with a gap of 0.7" between the two chips) and a pixel scale of 0.335"/pix using a 2.5x2.5 binning. For each science target we followed a dithering pattern in which the telescope was offset in RA and DEC by [-10,-10,5], [0,10, -20] arcsec respectively, to sample the gap between the detector chips. We, therefore, acquired three science frames, each with an exposure of 600 sec. The linear regime of the CCDs is below 65000 ADU.

5.3.2.1 Photometric calibration

The optical calibration plan comprises the following steps:

- acquire bias frames with closed shutter to measure the bias level set by detector electronics
- acquire dome/internal lamp flats to obtaine a map of the pixel variations inherent to the detector
- observe photometric standard stars (Landolt (1992)) on average three aquisitions per night, to properly sample variations in the airmass

5.3.2.2 Optical data reduction

The I-band data was reduced with the software `IRAF` and with customized `IDL` procedures. Each scientific target was processed in the following manner:

- combine the 2 detector chips to re-create a single frame using a MIDAS script available from http://www.ls.eso.org/lasilla/sciops/ntt/emmi/
- background subtraction
- flatfield normalization
- align images with reference stars
- merge the 3 dithered frames
- evaluate the image astrometric solution given a calibrated POSS/SERC-J plate

The transformations to a standard photometric magnitude system were determined by observing a set of Landolt photometric standard stars (Landolt (1992)), with which we computed zero points for each science field folowing the relation in Eq. 5.1.

5.3.3 I-H color images

In total, 22 fields were imaged both in the I- and H-bands during P78 and P79. In the following we show the corresponding I-H color images of the observed fields. The SOFI images were mapped to the pixel scale of EMMI using the routines *geomap* and *geotran* of IRAF. The *left* I+H color stamps have a 4.5 armin size whereas the *right* I-band stamps correspond to the inner 2.5 arcmin region; the X-ray contours are overlaid in blue. The software `Fitscut` was used to produce the color images. Visual inspection of the richness of the galaxy overdensities and coincidence of galaxies with X-ray peaks allows us to make an evaluation about the potential clusters. Thus, we outline the ensuing visual evaluation for the promising targets:

Table 5.2: ID and comment on the promising distant cluster candidates in P78 (first 4 lines up to the break), and in P79 (following 9 lines).

ID	Comment
116c	overdensity of galaxies coincident with X-rays
127b	likely very distant - faint galaxies
153	distinct BCG
165	rich cluster at z$\sim$1 - see Sect. 5.3.4
015	likely very distant - faint galaxies
035	distinct BCG
036	faint overdensity of galaxies coincident with X-rays
039	overdensity of galaxies coincident with X-rays
045	distinct BCG
059c	2 possible clusters
083	overdensity of galaxies coincident with X-rays
209b	faint overdensity of galaxies coincident with X-rays
241	distinct BCG

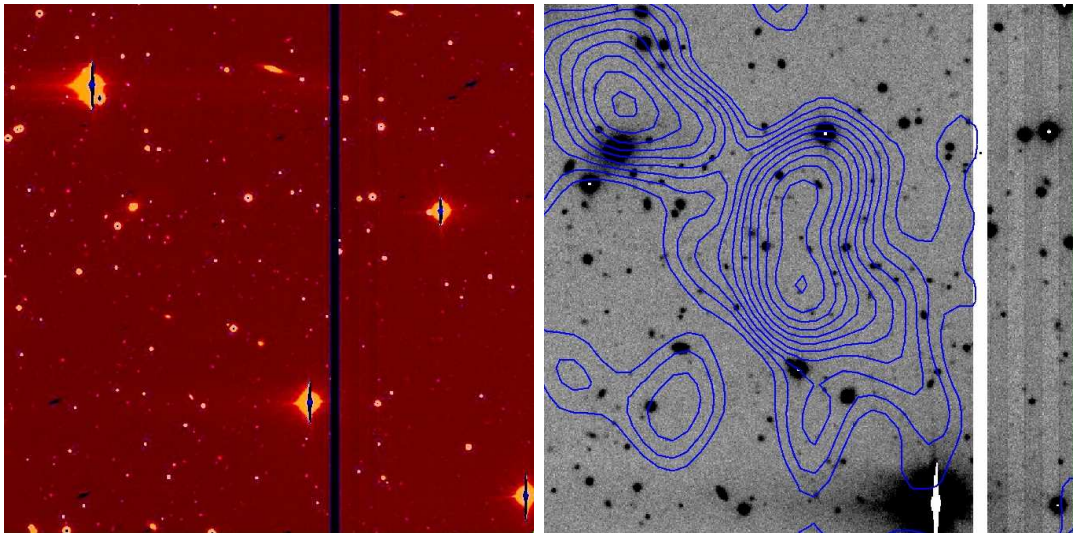

Figure 5.4: Cluster candidate 106. *Left* 4.5x4.5 arcmin I-H image of the field centered in the target. *Right* 2.5x2.5 arcmin optical image showing inner region of the field. No clear overdensity of galaxies is coincident with the X-ray contours, which also are of low significance.

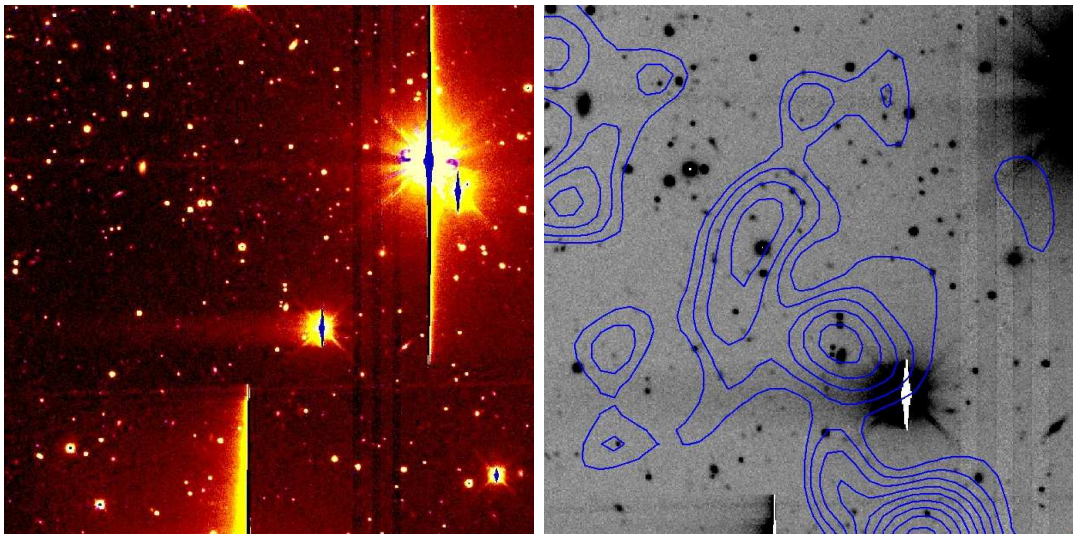

Figure 5.5: Cluster candidate 116c. *Left* 4.5x4.5 arcmin I-H image of the field centered in the target. *Right* 2.5x2.5 arcmin optical image showing inner region of the field. Several galaxies are coincident with the central "double" X-ray contours.

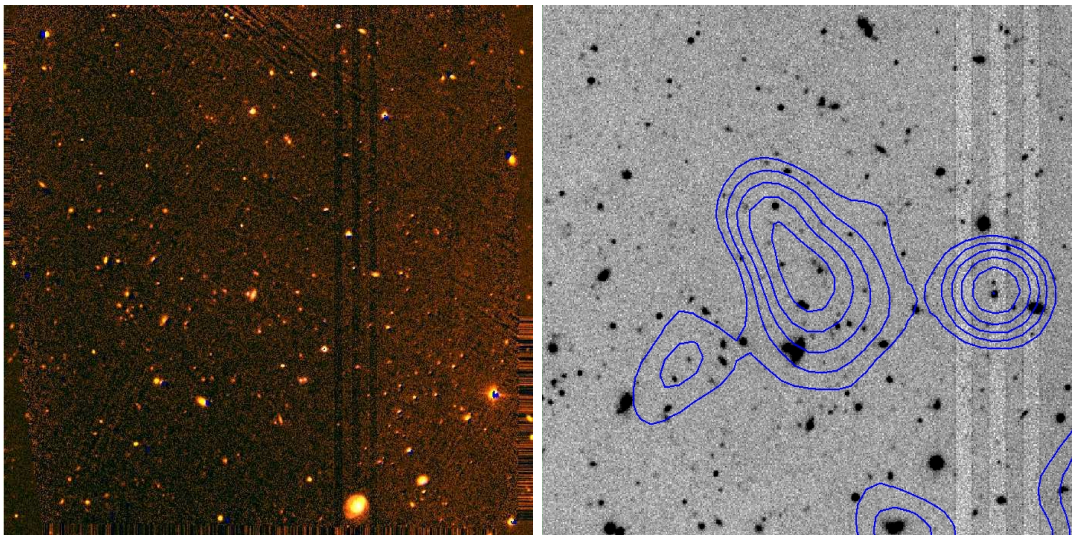

Figure 5.6: Cluster candidate 127b. *Left* 4.5x4.5 arcmin I-H image of the field centered in the target. *Right* 2.5x2.5 arcmin optical image showing inner region of the field. Faint galaxies are seen around the X-ray contours; this is likely a distant cluster.

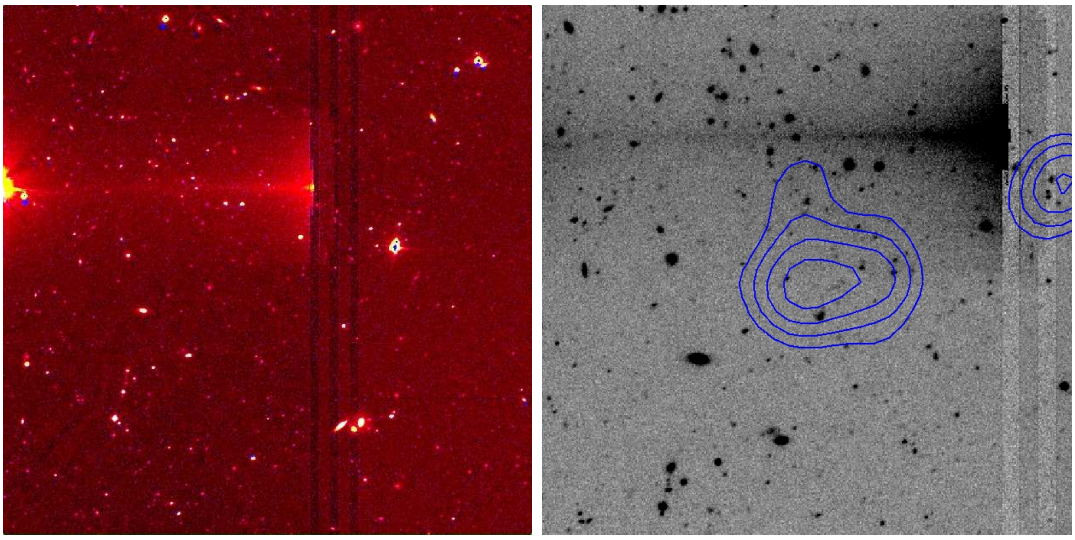

Figure 5.7: Cluster candidate 127c. *Left* 4.5x4.5 arcmin I-H image of the field centered in the target. *Right* 2.5x2.5 arcmin optical image showing inner region of the field. Faint galaxies are seen around the X-ray contours, however the target is strongly affect by two nearby bright stars.

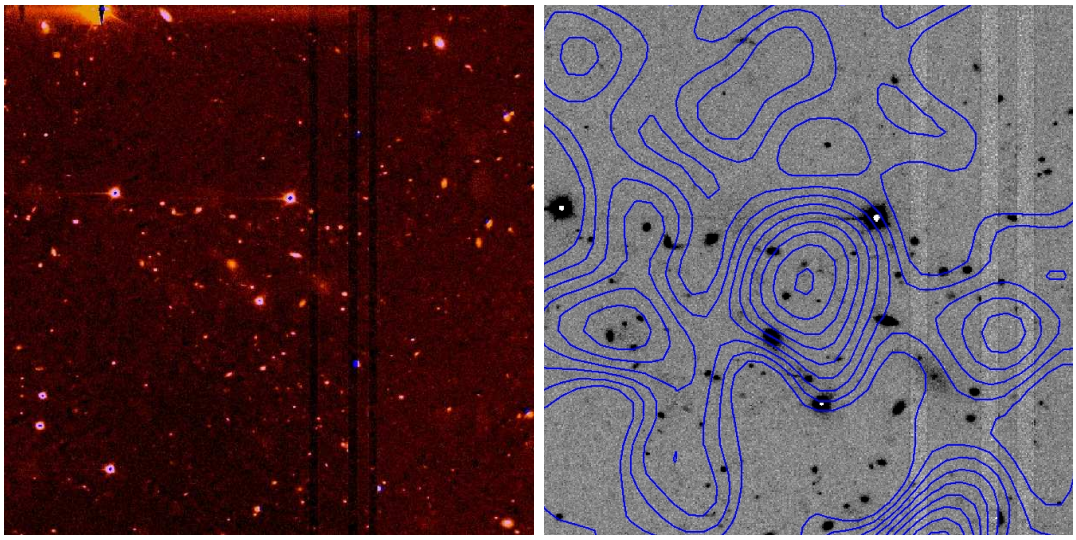

Figure 5.8: Cluster candidate 149. *Left* 4.5x4.5 arcmin I-H image of the field centered in the target. *Right* 2.5x2.5 arcmin optical image showing inner region of the field. No clear overdensity of galaxies is coincident with the X-ray contours, which also are of low significance.

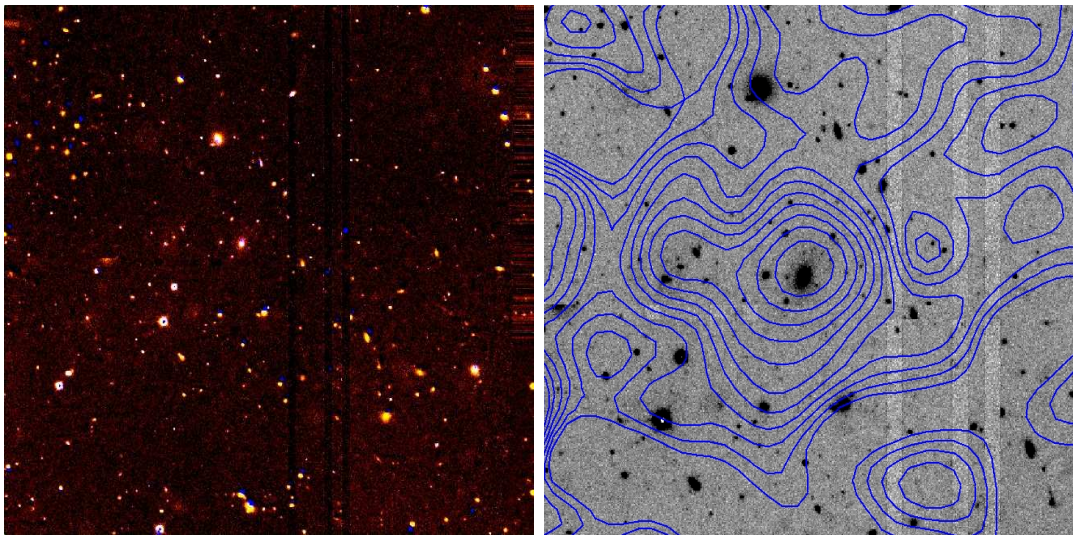

Figure 5.9: Cluster candidate 153. *Left* 4.5x4.5 arcmin I-H image of the field centered in the target. *Right* 2.5x2.5 arcmin optical image showing inner region of the field. Very bright (and possibly nearby) galaxy at the center of the X-ray contours.

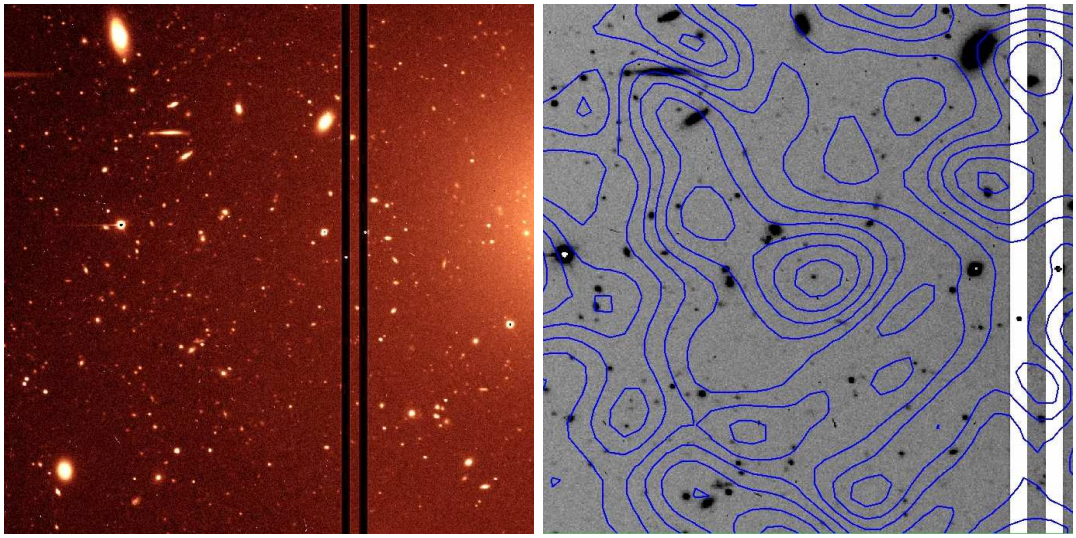

Figure 5.10: Cluster candidate 156. *Left* 4.5x4.5 arcmin I-H image of the field. *Right* 2.5x2.5 arcmin optical image showing inner region of the field. One faint galaxy lies at the center of the X-ray contours however this is not significant to draw a conclusion.

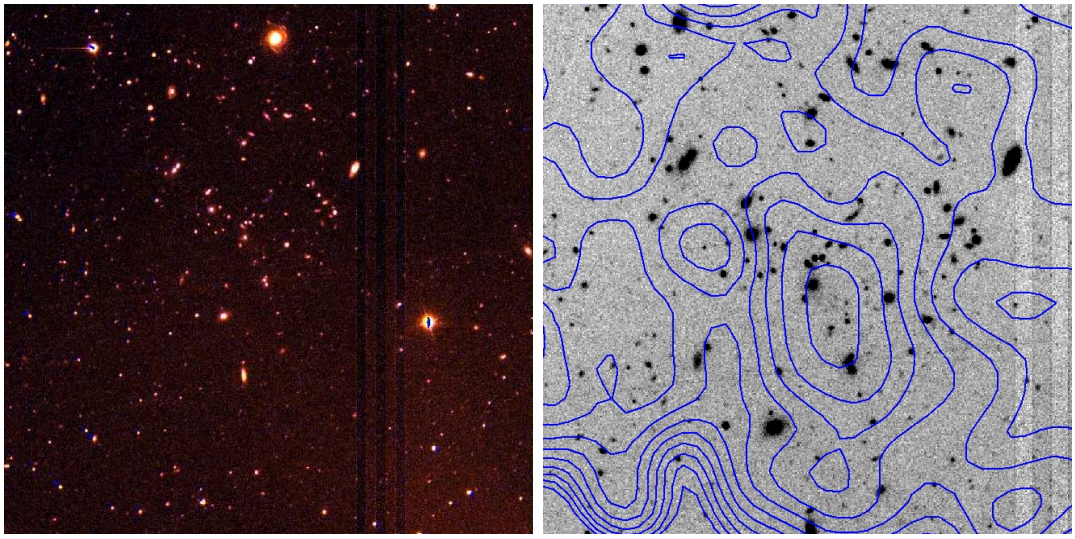

Figure 5.11: Cluster candidate 165. *Left* 4.5x4.5 arcmin I-H image of the field. *Right* 2.5x2.5 arcmin optical image showing inner region of the field. A rich overdensity of galaxies is coincident with the X-ray contours.

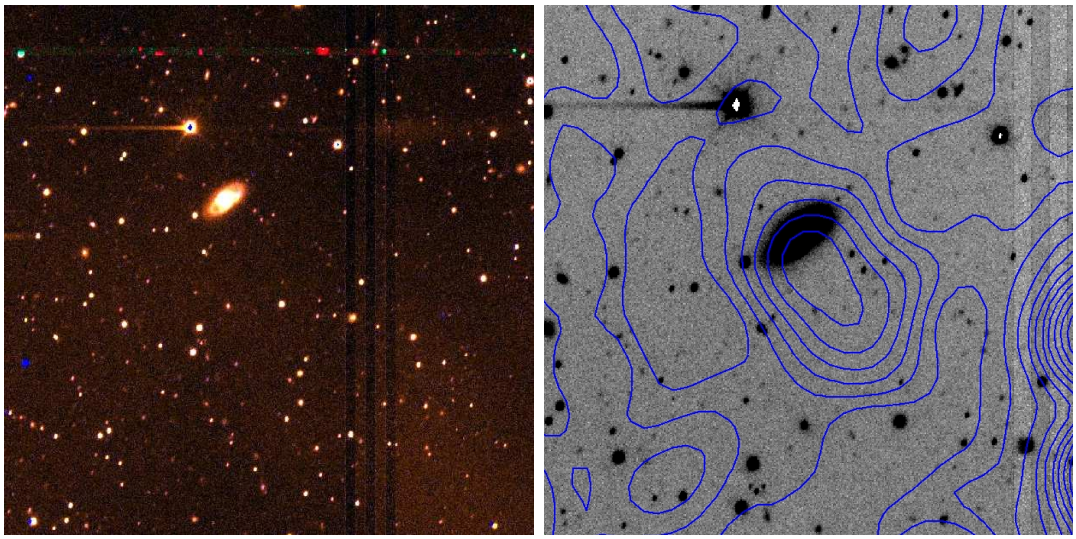

Figure 5.12: Cluster candidate 173. *Left* 4.5x4.5 arcmin I-H image of the field centered in the target. *Right* 2.5x2.5 arcmin optical image showing inner region of the field. Spurious detection.

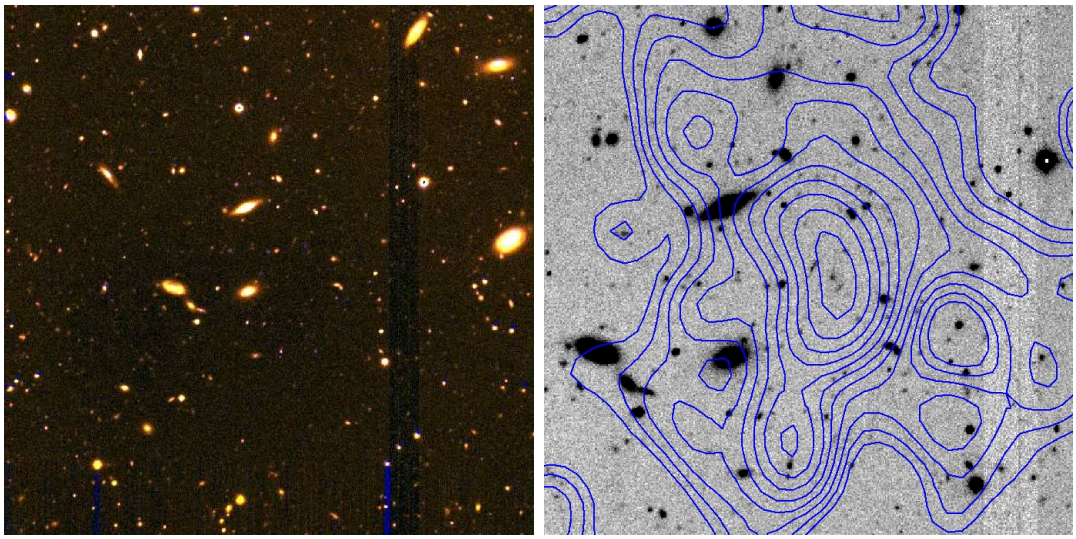

Figure 5.13: Cluster candidate 014. *Left* 4.5x4.5 arcmin I-H image of the field centered in the target. *Right* 2.5x2.5 arcmin optical image showing inner region of the field. Spurious detection or very distant galaxies.

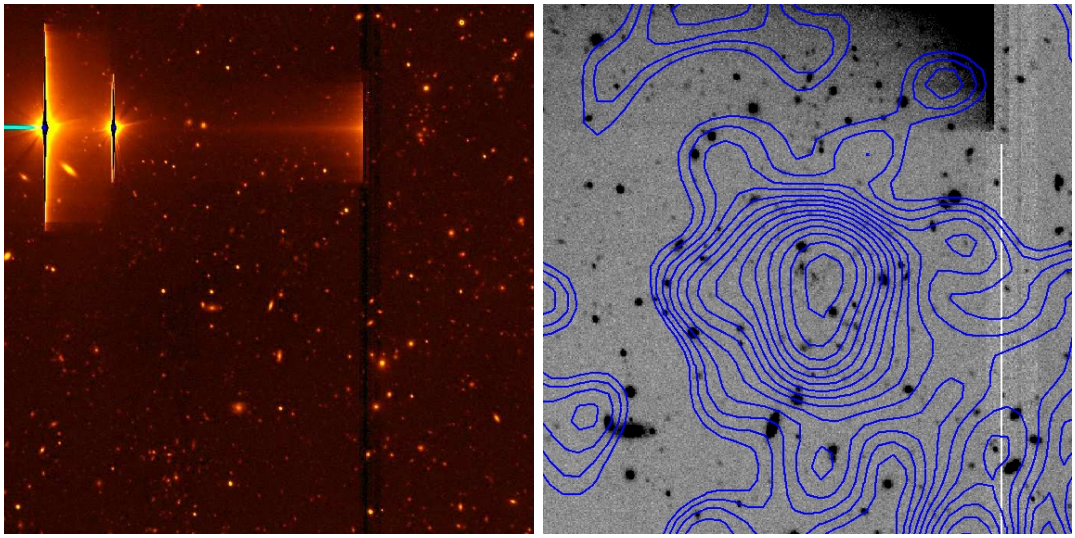

Figure 5.14: Cluster candidate 015. *Left* 4.5x4.5 arcmin I-H image of the field centered in the target. *Right* 2.5x2.5 arcmin optical image showing inner region of the field. Possible distant cluster.

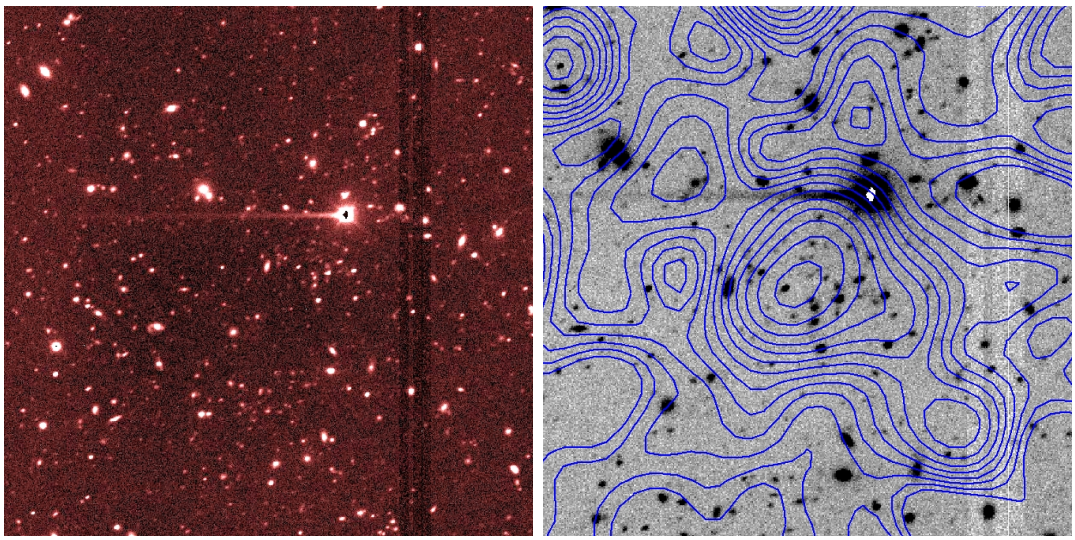

Figure 5.15: Cluster candidate 035. *Left* 4.5x4.5 arcmin I-H image of the field centered in the target. *Right* 2.5x2.5 arcmin optical image showing inner region of the field. An overdensity of galaxies coincident with X-rays indicates a possible cluster. Bright galaxy centered with the contours.

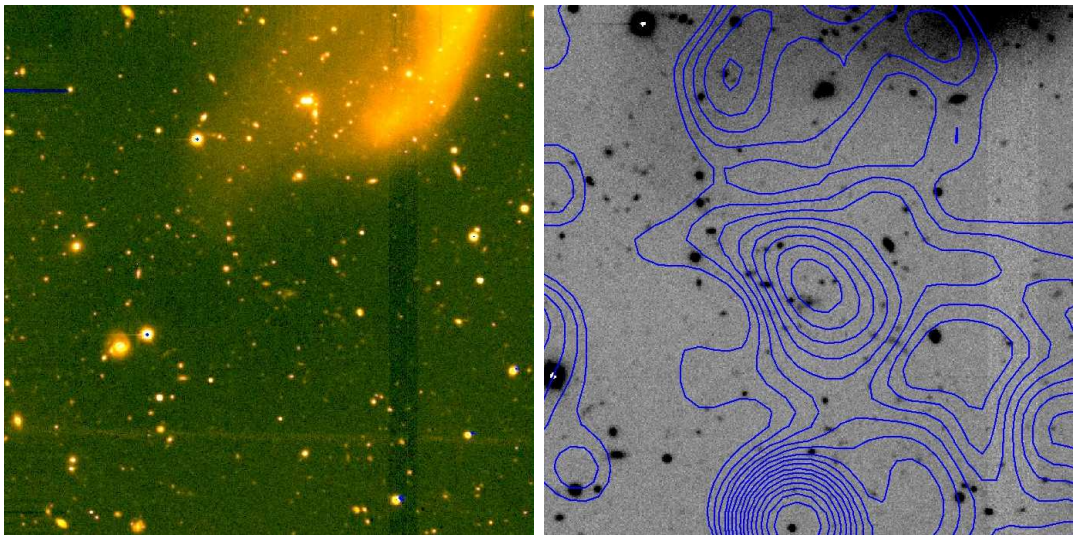

Figure 5.16: Cluster candidate 036. *Left* 4.5x4.5 arcmin I-H image of the field centered in the target. *Right* 2.5x2.5 arcmin optical image showing inner region of the field. Overdensity of galaxies coincident with X-rays.

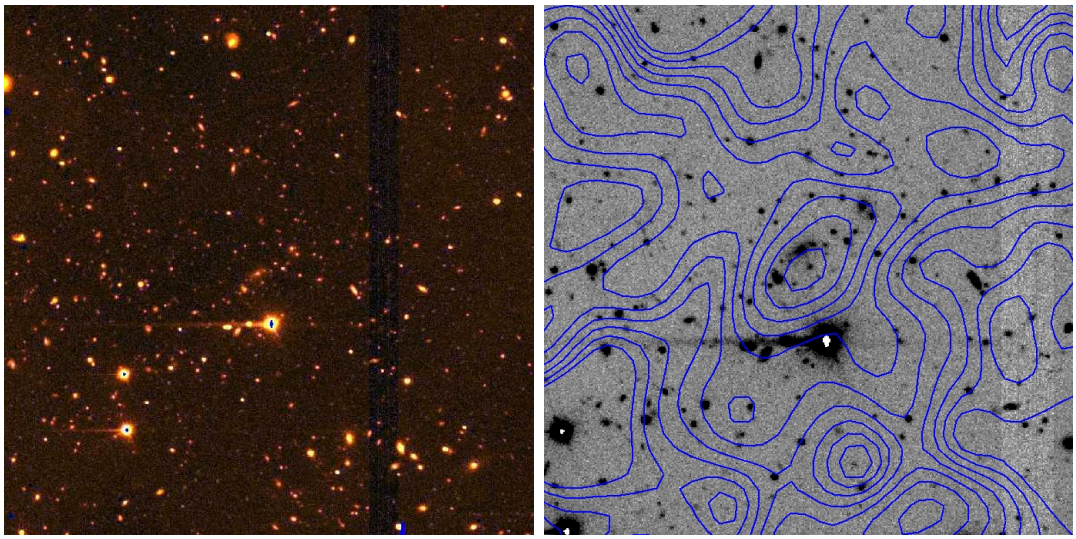

Figure 5.17: Cluster candidate 039. *Left* 4.5x4.5 arcmin I-H image of the field. *Right* 2.5x2.5 arcmin optical image showing inner region of the field. An overdensity of galaxies coincident with X-ray contours indicates a possible cluster.

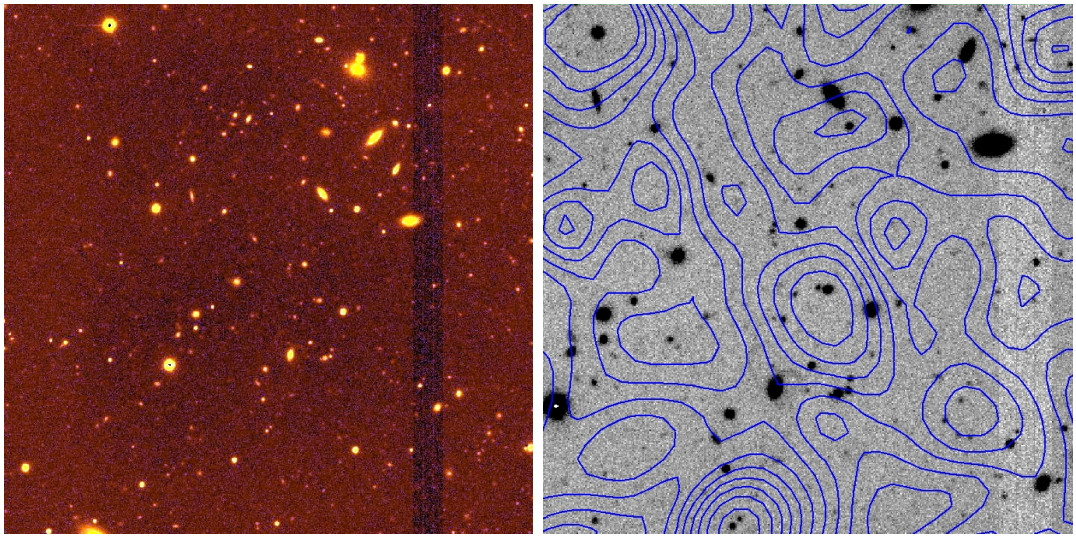

Figure 5.18: Cluster candidate 045. *Left* 4.5x4.5 arcmin I-H image of the field. *Right* 2.5x2.5 arcmin optical image showing inner region of the field. Bright nearby central galaxy which could be a field galaxy.

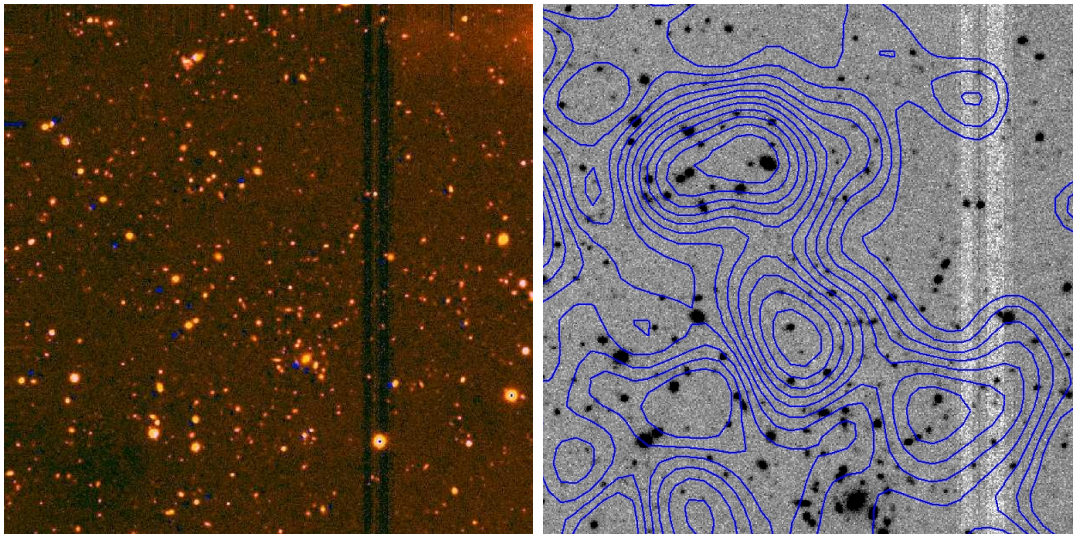

Figure 5.19: Cluster candidate 059c. *Left* 4.5x4.5 arcmin I-H image of the field. *Right* 2.5x2.5 arcmin optical image showing inner region of the field. The X-ray contours indicate two extended sources populated by galaxies. The north clump is rather bright indicating a nearby system.

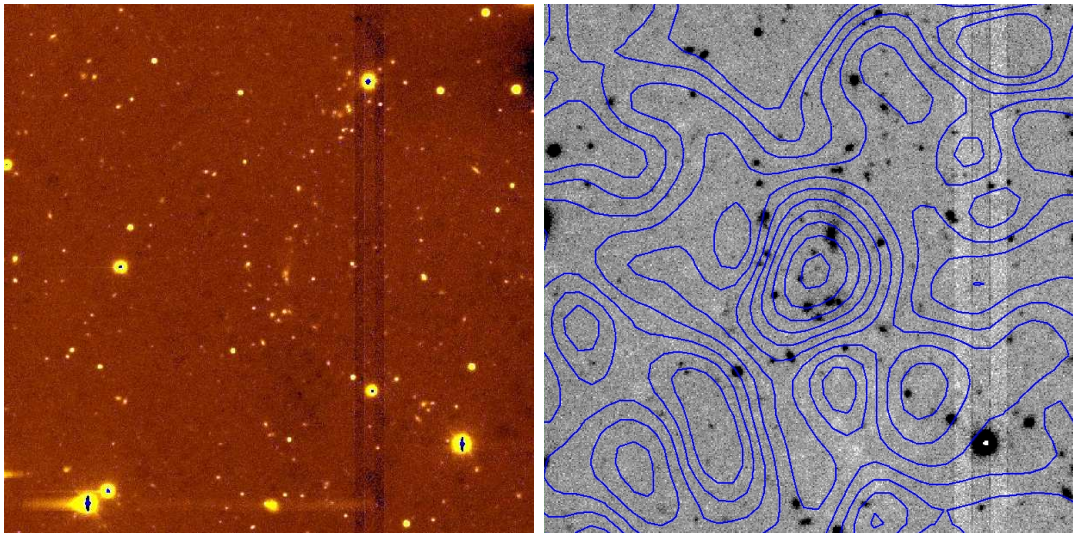

Figure 5.20: Cluster candidate 083. *Left* 4.5x4.5 arcmin I-H image of the field. *Right* 2.5x2.5 arcmin optical image showing inner region of the field. Clear overdensity of galaxies coincident with X-rays.

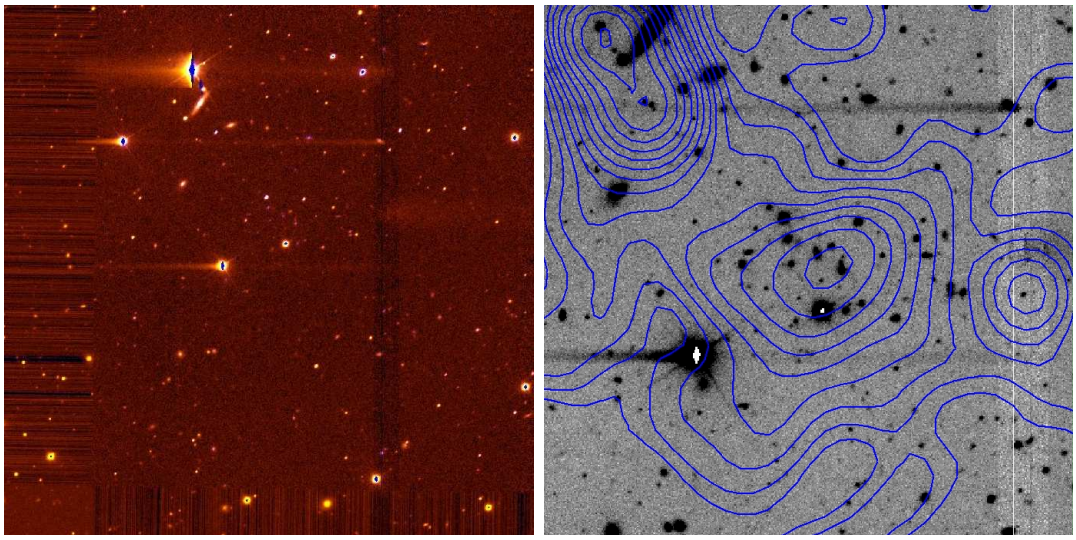

Figure 5.21: Cluster candidate 209b. *Left* 4.5x4.5 arcmin I-H image of the field. *Right* 2.5x2.5 arcmin optical image showing inner region of the field. Clear overdensity of faint galaxies coincident with X-rays.

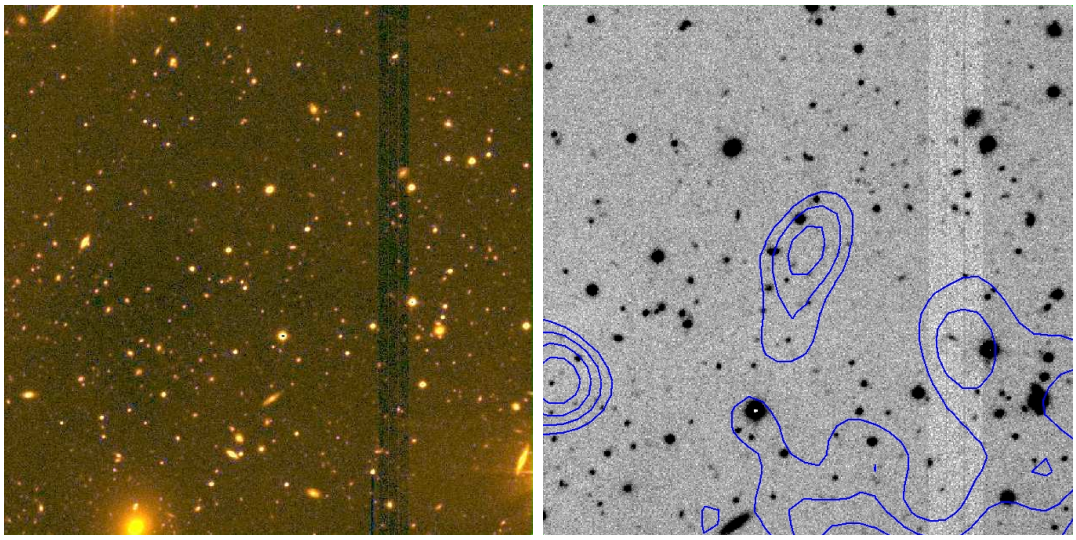

Figure 5.22: Cluster candidate 224. *Left* 4.5x4.5 arcmin I-H image of the field. *Right* 2.5x2.5 arcmin optical image showing inner region of the field. Spurious detection? X-ray contours have low significance although a handful of galaxies is coincident with the contous. Possible group.

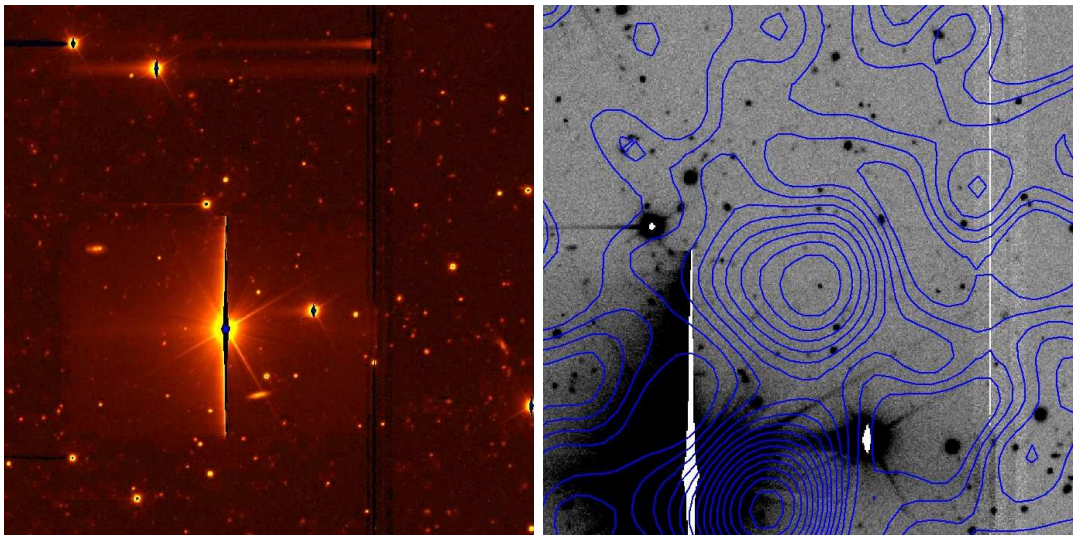

Figure 5.23: Cluster candidate 225b. *Left* 4.5x4.5 arcmin I-H image of the field. *Right* 2.5x2.5 arcmin optical image showing inner region of the field. Spurious detection? A very bright source in the vincinity of the target makes the evaluation very diffcult.

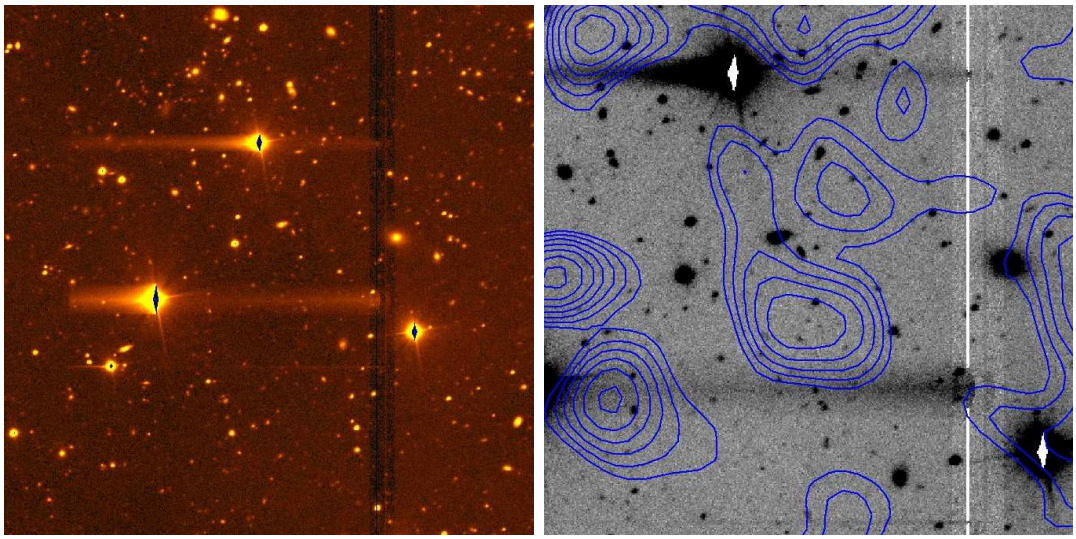

Figure 5.24: Cluster candidate 234b. *Left* 4.5x4.5 arcmin I-H image of the field. *Right* 2.5x2.5 arcmin optical image showing inner region of the field. Spurious detection.

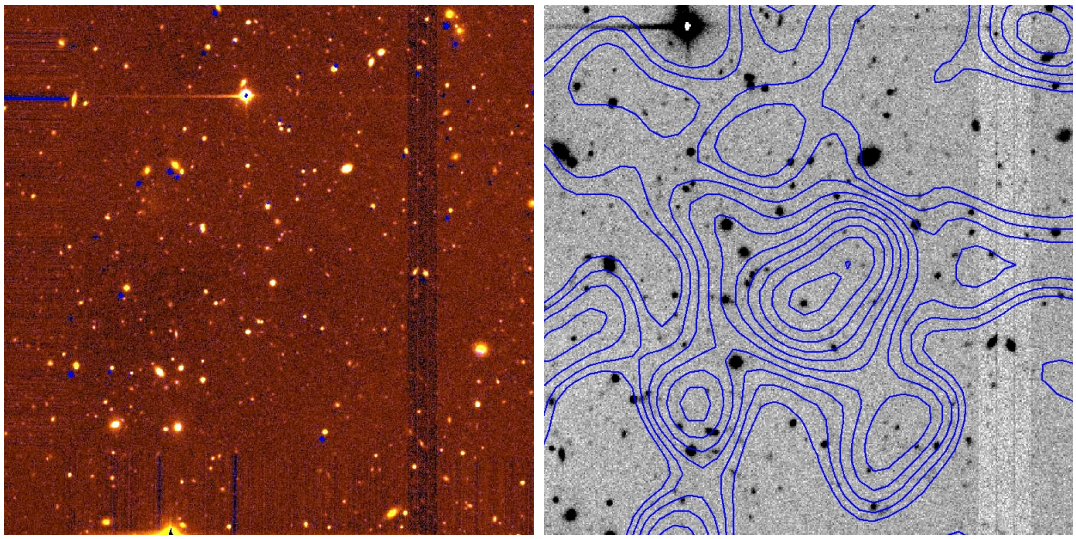

Figure 5.25: Cluster candidate 241. *Left* 4.5x4.5 arcmin I-H image of the field. *Right* 2.5x2.5 arcmin optical image showing inner region of the field. Clear over-density of galaxies coincident with X-rays; BCG centered with the contours.

5.3.4 I-H color-magnitude relation of cluster 165

We construct the I-H CMR for one of the richest cluster candidates in P78, cluster 165. The seeing is very similar is both passbands, 0.77“ in I and 0.73 in H, therefore we ignored aperture corrections in this first quick-look color-magnitude relation. The source detection and photometry were made with SExtractor in *dual mode*, using the SOFI data mapped to the EMMI pixel scale and performing the detection in the H-band. The galactic extinction was accounted for using dust extinction maps from Schlegel et al. (1998) available at the Nasa Extragalactic Database (NED). We retrieved E(B-V) = 0.025 mag, corresponding to corrections in the I- and H-bands of 0.049 mag and 0.015 mag, respectively. The color measurement was performed in apertures of 3 pix, corresponding to 1.0“ in the EMMI pixel scale (smaller than this radius would give noisy measurements). The color-magnitude diagram is presented in Fig. 5.27. We made a visual selection of galaxies likely to belong to the cluster, based on the color image and X-ray contours. These objects are marked with red circles in the CMR. A tentative fit to these galaxies indicates a I-H zero point of ∼2.8, which is consistent with a cluster at redshift 0.8, according to Fassbender (2008), based on syntethic stellar population modelling of the redshift evolution of the I-H color.

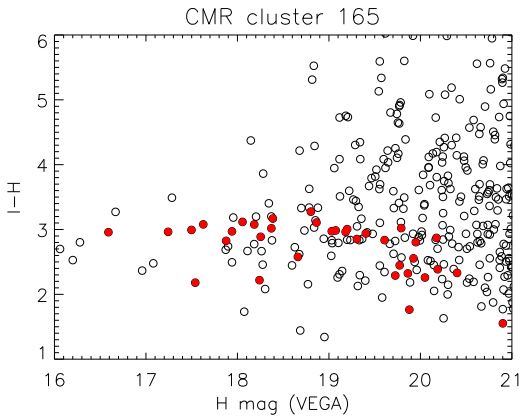

Figure 5.26: I-H color-magnitude diagram of potential distant cluster 165.

5.4 Summary and conclusions

The XDCP has already proven to be a successful survey, with the discovery of 11 z$\gtrsim$1 clusters. The I-H follow-up of 22 cluster candidates selected in this programme indicates that ∼ 12 candidates do show a convincing overdensity of galaxies coincident with the X-ray emission, and therefore should be subsequently observed with FORS2

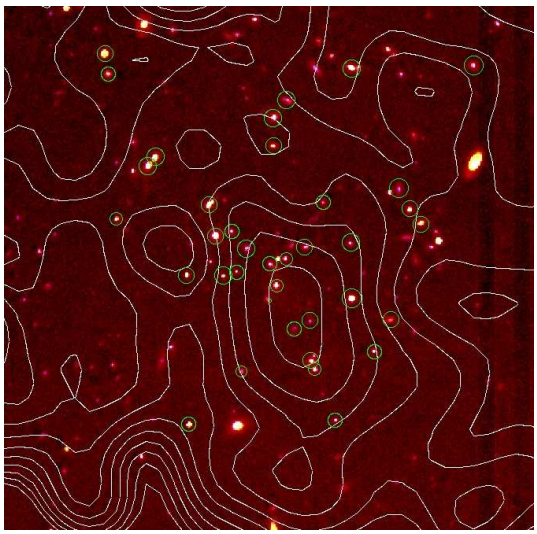

Figure 5.27: I-H color image of cluster 165 indicating the selection of potential cluster galaxies in green circles.

to aquire spectra, after imposing a suitable estimated redshift cut by means of the CMRs. This subsample represents 10% of the total number of observed candidates within the XDCP. The I-H color-magnitude relation derived for cluster 165 indicates this is a promising z$\sim$0.8 cluster with a distinct red-sequence. Spectroscopic observations have already been obtained using FORS2 at the VLT for part of the sample, including cluster 165. The processing of the full sample is underway.

This analysis opens the way to the next chapter, where we make an in-depth study of the galaxy population in a massive cluster with z=0.976 discovered in the XDCP, using HST/ACS imaging.

6

Multi-wavelength observations of a rich galaxy cluster at z ∼ 1

Abstract

XMMU J1229+0151 is a rich galaxy cluster with redshift z=0.975, which was serendipitously detected in X-rays within the scope of the XMM-Newton Distant Cluster Project.

We investigate the photometric, structural and spectral properties of the early-type galaxies in this high-redshift cluster, based on observations carried out using the Advanced Camera for Surveys at the Hubble Space Telescope under Program ID 10496; the Very Large Telescope at the ESO Paranal Observatory under Program IDs 176.A-0589(A), 276.A-5034(A) and the New Technology Telescope at the ESO/La Silla Observatory under Program ID 078.A-0265(B).

We perform the source detection and measure aperture photometry in the optical and Near-InfraRed (NIR) imaging. Galaxy morphology is inspected visually and by means of Sersic profile fitting to the 21 spectroscopically confirmed cluster members in the ACS field of view. A new method to construct the i_{775}-z_{850} color-magnitude relation (CMR) is explored, based on the Sersic galaxy models. Fitting the red-sequence in the CMR allows us to color-select other galaxies lying in this region. Stellar masses and formation ages of the cluster galaxies are derived by fitting the observed spectral energy distributions (SED) with models based on Bruzual & Charlot (2003). Star formation histories of early-types are constrained by analysis of the stacked spectrophotometric data. The structural Sersic parameters n and R_e are in agreement

with the visual morphological classification, indicating a clear predominance of elliptical galaxies, both in the confirmed members (15/21) and color-selected samples (32/36). The i_{775}-z_{850} color-magnitude relation of the spectroscopic members shows a very tight red sequence with zero point 0.829±0.041 and scatter 0.042±0.011 mag. This population is fairly old, with a star formation weighted age of 4.3 Gyr for a median mass of 7.4 $\times 10^{10}$ $M_{\odot}$. Instead of an unambiguous brightest cluster galaxy (BCG), we find that the three brightest cluster galaxies have a similar z_{850} magnitude, and in addition are the most massive, with $\sim 2 \times 10^{11}$ $M_{\odot}$. Our results are consistent with a "downsizing" scenario where the most massive galaxies are the oldest.

6.1 Introduction

Distant (z∼1) galaxy clusters are unique astrophysical laboratories particularly suited to witness and study galaxy formation and evolution.

Detailed studies of the properties of galaxies in large samples of high-redshift clusters are required to distinguish the two main galaxy formation scenarios, which have been under discussion for more than 30 years. In the *monolithic picture* (Eggen et al. (1962); Larson (1974)), massive galaxies are expected to be formed early from a single progenitor. In contrast, the *hierarchical scenario* (Toomre (1977); White & Rees (1978)) predicts that elliptical galaxies should form later, through mergers. The behavior of early-type galaxies (ETGs), which are found to comprise both the most massive *and* oldest systems, is the main cause for this debate. Indeed, it is now established that the star formation histories of ellipticals are mass-dependent (De Lucia et al. (2004), Thomas et al. (2005), van der Wel et al. (2005)), in which low mass galaxies have more extended star formation histories than massive galaxies. This implies that the less massive galaxies have a lower formation redshift than the more massive systems, whose star formation histories typically peak at z∼5 (De Lucia et al. (2006)). This scenario is commonly refered to as "downsizing" (Cowie et al. (1996)). Supporting this picture, there is strong observational evidence for the bulk of the stars in massive ellipticals to be already formed at redshift > 2 (van Dokkum (2005), Tran 2005, Holden et al. (2005)), which appears to be in contradiction with the predictions from the cold dark matter (CDM) standard cosmology.

The color-magnitude relation (CMR, Visvanathan & Sandage (1977), Sandage & Visvanathan (1978)) is a fundamental scaling law to assess the evolution of galaxy populations. The CMR of local clusters shows the existence of a tight Red Sequence (RS, Bower et al. (1992), de Propris et al. (1998)) (Gladders & Yee (2000)) formed of massive red elliptical galaxies undergoing passive evolution, and the analysis of its main parameters (zero point, scatter and slope) provides a means to quantify evolution of the galaxies properties with redshift. It remains, nevertheless, unclear to what degree the CMR is determined by age and metallicity effects.

The study of high-z samples of galaxies is also important to provide information for the modelling of physical processes in semi-analytical modelling (SAM). SAM employing AGN feedback to prevent the overproduction of blue galaxies have recently succeeded in predicting a large amount of massive old galaxies (De Lucia et al. (2006), Bower et al. (2006), Menci et al. (2006)), however, several issues remain yet to be solved, such as the incapability to reproduce quantitatively the color-bimodality in the color-magnitude diagram and the scatter of the red-sequence, which is overestimated by a factor 2-3 (e.g. Menci et al. (2008)).

The exceptional high-resolution provided by the Advanced Camera for Surveys (ACS) at the Hubble Space Telescope (HST) has greatly contributed to the current knowledge on the evolution of galaxies in dense environments. Results on the eight z∼1 clusters of the ACS Intermediate redshift cluster survey (Blakeslee et al. (2003); Mei et al. (2007), Holden et al. (2005)), and studies of individual distant clusters (RDCS 1252.9-2927 at z=1.235: Lidman et al. (2004), Demarco et al. (2007); XMMU J2235.3-2557 at z=1.393: Rosati (2008), Lidman et al. (2008)) point toward the prevalence of a clear RS up to z=1.4, where the CMR zero point and scatter are observed to slightly increase with redshift.

In this paper we provide a detailed analysis of the galaxy properties in XMMU J1229+0151 (hereafter, XMM1229), an X-ray selected, optically rich and distant cluster (z=0.976 corresponding to a lookback time of 7.6 Gyr). We derive accurate color measurements from the high-resolution ACS data, and characterize the galaxy morphology through a visual inspection and by fitting Sersic profiles. Stellar masses, ages and star formation histories of the cluster's early-types are derived by fitting the coadded spectrophotometric data with Bruzual & Charlot (2003) templates.

The paper is organized as follows: in Sect. 2 we present the imaging and spectroscopic data, as well as reduction procedures. The ACS morphological analysis of the confirmed cluster members is introduced in Sect. 3. In Sect. 4 we derive the $i_{775} - z_{850}$ CMR and the results from the SED fitting are presented in Section 5. In Sect. 6 we investigate the brightest cluster galaxies. We conclude in Sect. 7.

The cosmological parameters used throughout the paper are H_0=70 km/s/Mpc, Ω_Λ=0.7 and Ω_m =0.3. Filter magnitudes are presented in the AB system unless stated otherwise.

6.2 Observations and data reduction

6.2.1 XMM-Newton data

The cluster XMM1229 was initially detected in a serendipitous cluster survey of the XMM-Newton archive, the XMM-Newton Distant Cluster Project (XDCP, Böhringer et al. (2005), Fassbender (2008)). Our target was observed in 25 XMM-Newton pointings of the bright radio loud quasar 3C 273 at an off-axis angle of approximately 13 ar-

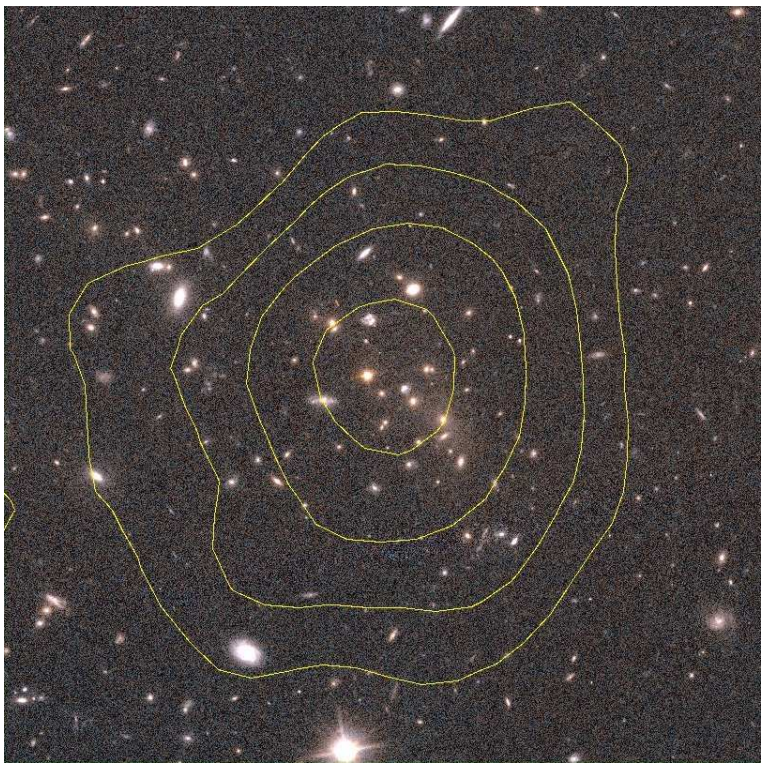

Figure 6.1: HST/ACS color image of XMMU J1229+0151 with X-ray contours. The image is centered on the cluster X-ray emission and has a size of 1.5 arcmin^2.

cmin. We selected only observations whose exposure time, after cleaning for high background periods, was larger than 10 ks. Unfortunately, XMM1229 was not observed by the pn camera, since the pn was always operated in Small Window Mode (except for Obs_Id=0126700201, having a clean exposure time of only ∼ 6 ks). Therefore, we used only the data from the two XMM/MOS CCDs. The 11 observations selected for our analysis are listed in Table 6.1.

Data were processed using the XMM-Newton Science Analysis Software (`SAS v7.0.0`). Light curves for pattern=0 events in the $10 - 15$ keV band were produced to search for periods of background flaring, which were selected and removed by applying a 3σ clipping algorithm. Light curves in the $0.3 - 10$ keV band were visually inspected to remove residual soft-proton induced flares. We selected events with patterns 0 to 12 (single, double and quadruple) and further removed events with low spectral quality (i.e. `FLAG=0`). Table 6.1 lists the resulting clean exposure times for each observation. We obtained total exposure times of ∼ 370 and ∼ 400 ks for the XMM/MOS1 and

XMM/MOS2, respectively.

The spectra of the cluster were extracted from a circular region of radius 30 arcsec centered at RA=12:29:29.2, Dec=+01:51:26.4. The background was estimated from a circular region on the same chip of radius ~ 2 arcmin centered at RA=12:29:21.2, Dec=+01:51:55.4, after removing cluster and point sources.

To correct for vignetting effects, we used the `SAS` task `EVIGWEIGHT` (Arnaud et al. (2001)), so that we can use on axis effective areas. Redistribution matrices were generated using the `SAS` task `RMFGEN` for each pointing, filter, and detector.

Time averaged spectra for the source and the background were obtained by adding the counts for each channel. Since different filters were used for the observations, we weighted each instrument effective area (ARF) and redistribution matrix (RMF) with the exposure time of the observation. In order to use the χ^2 minimization in the spectral fitting we binned the spectra with a minimum number of 20 counts per bin.

Table 6.1: Log of the XMM-Newton observations of XMM1229. The information given is the following: observation date (column 1), XMM-Newton observation identification number (column 2) and revolution (column 3), filter (M=medium, T=thin) and mode (F=full window, S=small window) used (column 4), good exposure time of XMM/MOS1+MOS2, after cleaning for high particle background periods (column 5).

Date	**Obs. Id.**	**Rev.**	**Filt./Mode**	**T$_{exp}$ [ks]**
(1)	(2)	(3)	(4)	(5)
2000-06-13	0126700201	0094	M/F	11.7+11.6
2000-06-14	0126700301	0094	M/F	56.4+56.1
2000-06-15	0126700601	0095	M/S	24.0+23.7
2000-06-16	0126700701	0095	M/S	17.5+17.8
2000-06-18	0126700801	0096	M/S	40.8+41.1
2001-06-13	0136550101	0277	T/S	40.1+40.1
2003-07-07	0159960101	0655	T/S	51.3+54.6
2004-06-30	0136550801	0835	T1-M2/S	14.3+47.7
2005-07-10	0136551001	1023	M/S	26.9+26.7
2007-01-12	0414190101	1299	M/S	57.3+55.5
2007-06-25	0414190301	1381	M/S	26.8+26.2

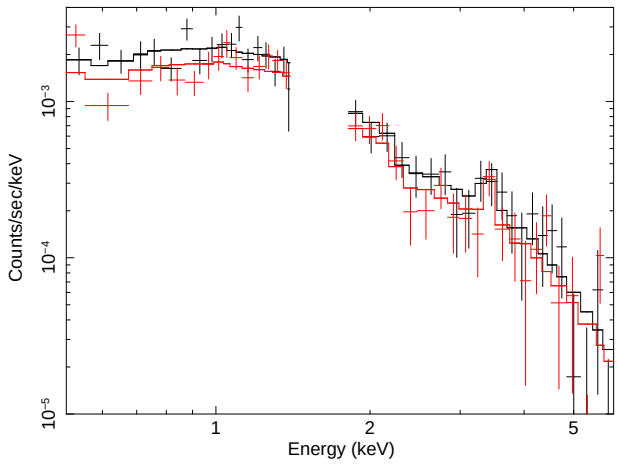

Figure 6.2: X-ray spectra of XMM1229 from the XMM/MOS1 (black) and XMM/MOS2 (red) detectors. The solid lines show the best-fit models. The Fe K-line is prominent at 3.2 keV.

6.2.1.1 Spectral analysis

The two XMM/MOS spectra were analyzed with XSPEC v11.3.1 (Arnaud (1996)) and were fitted with a single-temperature `mekal` model (Kaastra (1992); Liedahl et al. (1995)). We modeled Galactic absorption with `tbabs` (Wilms et al. (2000)). We always refer to values of solar abundances as in Anders & Grevesse (1989).

The fits were performed over the $0.5 - 6$ keV band. We excluded energies below 0.5 keV, due to calibration uncertainties, and above 6 keV, where the background starts to dominate. Furthermore, due to the relatively low S/N of the observations, we notice that instrumental Kα emission lines[1] from Al (at ~ 1.5 keV) and Si (at ~ 1.7 keV) may affect the spectral analysis significantly. Therefore, we also excluded photons in the energy range $1.4 - 1.8$ keV from our spectral analysis. In the selected energy bands we have a total of ~ 1300 and ~ 1200 net counts for the XMM/MOS1 and XMM/MOS2, respectively.

The free parameters in our spectral fits are temperature, metallicity, redshift and normalization, although we also performed the fit freezing the redshift to 0.975, the median spectroscopic redshift of the confirmed galaxies. Local absorption is fixed to the Galactic neutral hydrogen column density, as obtained from radio data (Dickey & Lockman (1990)).

Results of the spectral analysis are listed in Table 6.2, the quoted errors are at the 1 sigma confidence level. The rest-frame luminosity corrected for Galactic absorption

[1] http://xmm.vilspa.esa.es/external/xmm_user_support/documentation /uhb/node35.html

Table 6.2: Results of the X-ray spectral analysis. The information given is the following: data set used, i.e. XMM/MOS1, XMM/MOS2, and the two combined (column 1), temperature (column 2), iron abundance (column 3), redshift (column 4), χ^2 and number of degrees of freedom (column 5). The last line refers to the spectral fit with redshift set to 0.975.

Detector	**kT [keV]**	$\mathbf{Z_{Fe}}$ $[\mathbf{Z_\odot}]$	**z**	χ^2**/d.o.f.**
(1)	(2)	(3)	(4)	(5)
MOS1	$6.2^{+1.0}_{-0.8}$	$0.37^{+0.20}_{-0.18}$	$0.961^{+0.020}_{-0.025}$	45.1/51
MOS2	$6.2^{+1.1}_{-0.6}$	$0.42^{+0.22}_{-0.21}$	$0.950^{+0.027}_{-0.021}$	50.1/44
MOS1+2	$6.25^{+0.69}_{-0.55}$	0.38 ± 0.14	0.956 ± 0.017	95.4/98
MOS1+2	$6.4^{+0.7}_{-0.6}$	$0.34^{+0.14}_{-0.13}$	–	96.8/99

in the $0.5 - 2.0$ keV range is $(1.3 \pm 0.2) \times 10^{44}$ erg s^{-1}, for an aperture of 30 arcsec radius, which corresponds to a physical size of 240 kpc. Extrapolating the luminosity to a radius of 2 Mpc assuming a King model with standard parameters β=0.7 and core radius r_c=250 kpc, the luminosity increases by a factor 2.24, L_X (r<2 Mpc) $\sim 3 \times 10^{44}$ erg s^{-1}.

6.2.2 HST/ACS i_{775} and z_{850} band imaging

In the framework of the Supernova Cosmology Project (Dawson (2009)) we obtained the HST/ACS Wide Field Camera (WFC) data. Images in the F775W (i_{775}) and F850LP (z_{850}) passbands were acquired in December 2006 with total exposures of 4110 sec and 10940 sec respectively. The i_{775} and z_{850} are the most efficient filters in supernova searches and, although they are not optimal for a cluster at this redshift, the i_{775} encloses the D4000 break, which is redshift to 7920 $\mathring{A}$ at the cluster redshift. ACS has a field of view (FoV) of 3.3 x 3.3 arcmin and a pixel scale of 0.05"/pix. The images were processed with the *Apsis* pipeline (Blakeslee et al. (2003)), with a *Lanczos*3 interpolation kernel. The photometric zero points are 34.65 and 34.93 in the i_{775} and z_{850} bands respectively. To account for the galactic extinction we applied the correction factor $E(B-V)$=0.017 retrieved from the NASA Extragalactic Database[2] and using the dust extinction maps from Schlegel et al. (1998). The corresponding correction in the optical bands is E(i_{775}-z_{850})=0.010 mag.

[2]http://nedwww.ipac.caltech.edu/

6.2.3 VLT/FORS2 spectroscopy

Spectroscopic observations were carried with Focal Reducer and Low Dispersion Spectrograph (FORS2: Appenzeller et al. (1998)) on Antu (Unit 1 of the ESO Very Large Telescope (VLT)) as part of a program to search for very high redshift Type Ia supernova in the hosts of early type galaxies of rich galaxy clusters (Dawson (2009)). In this respect, the field XMM1229 was very rich in candidates, with three candidates occurring in the space of a few months. One candidate was identified as a Type Ia supernova at the cluster redshift (Dawson (2009)).

FORS2 was used with the 300I grism and the OG590 order sorting filter. This configuration has a dispersion of 2.3 Åper pixel and provides a wavelength range starting at 5900 Angstroms and extending to approximately 10000 Å. Since the observations had to carried out at short notice (the SN had to be observed while it was near maximum light), most of the observations were done with the multi-object spectroscopic (MOS) mode of FORS2. The MOS mode consists of 19 moveable slits (with lengths that vary between 20" and 22") that can be inserted into the focal plane. The slit width was set to 1". On one occasion, when the MOS mode was unavailable because of technical reasons, the field was observed with the MXU mode of FORS2. The MXU mode consists of precut mask that is inserted into the FORS2 focal plane once the field has been acquired. Since the length of the slit can be made much shorter in the MXU mode than in the MOS mode, the number of targets that could be observed in the MXU mode was a factor of two larger than the number of targets that could be observed in the MOS mode. However, the time to prepare, cut and insert a mask is usually a couple of days, whereas the MOS observations can be done with a few hours notice.

The field of XMM1229 was observed with four different configurations, 4 MOS and one MXU. The details of the of the observations are given in Table 6.3. The MOS configurations were used when the supernovae (there were three supernova visible in the field of XMM1229 at the same time) were near maximum light. The MXU mask was used several months later when the supernovae were significantly fainter. In all masks, slits were placed on the supernova, thus spectra of the supernovae together with their hosts and spectra of the hosts without the supernovae were obtained. The other slits were placed on candidate cluster galaxies or field galaxies. For each MOS setup, between 4 and 9 exposures of 700 to 900 seconds were taken. Between each exposure, the telescope was moved a few arc seconds along the slit direction. These offsets, which shift the spectra along detector columns, allow one to remove detector fringes, as described in Hilton et al. (2007), which also details how the FORS2 data was processed.

A total of 100 slits over four masks were used to observe 75 individual targets. Some cluster members were observed in more than mask. From these 74 targets, 64 redshifts were obtained, and 27 of these are cluster members. A total of 21 confirmed

Table 6.3: FORS2 Observing Log

Mask	Type	Slits	Grism & Filter	T_{exp} (s)	Airmass	Date (UT)
1	MOS	12	300I+OG590	8 x 750	1.3	2006 Jan 01
2	MOS	18	300I+OG590	8 x 700	1.2	2006 Jan 30
3	MOS	18	300I+OG590	4 x 700	1.1	2006 Jan 31
4	MOS	18	300I+OG590	4 x 700	1.2	2006 Feb 01
5	MXU	34	300I+OG590	9 x 900	1.3	2006 Jun 20-21

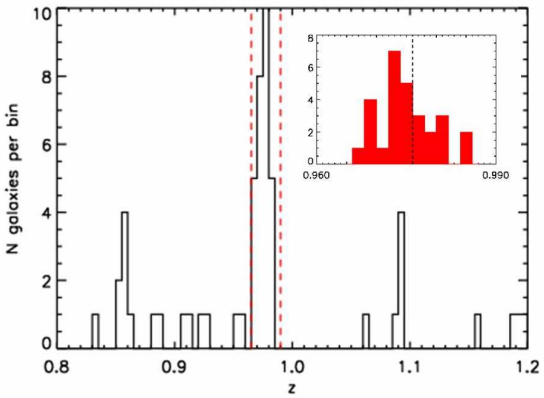

Figure 6.3: Redshift distribution of the galaxies in the cluster XMMU J1229+0151. Vertical red-dashed lines refer to redshift cuts at z=0.965, 0.990 used to select the cluster members. This region is shown in more detail in the top-right inslet.

galaxies are within the FoV of ACS.

Following Danese et al. (1980) we determined the cluster velocity dispersion from the 27 spectroscopic members, obtaining σ= 683 km/s. Cluster membership was attributed by a reasonable selection of galaxies within 2000 km/s or $\sim$ 3-σ. In Table 6.4 we list the 27 cluster members, indicating the spectral class according to the scheme proposed in Dressler et al. (1999) based on the strength of the OII and H_δ lines.

6.2.4 NTT/SOFI J- and Ks-band imaging

NIR imaging in the J- and Ks-bands were acquired using SOFI (Moorwood et al. (1998)) at the New Technology Telescope (NTT) at the ESO/La Silla observatory.

Table 6.4: Spectroscopic confirmed members. The information given is the following: galaxy ID (column 1); galaxy coordinates in the J2000 system, RA (column 2) and DEC (column 3); redshift (column 4); and spectral classification (column 5).

Object ID	**RA (J2000)**	**DEC (J2000)**	**z**	**Class**
(1)	(2)	(3)	(4)	(5)
5417	187.3857875	1.8712528	0.977	a+k
3428	187.3793000	1.8563222	0.984	a+k
3430	187.3720375	1.8560639	0.974	k
3025	187.3771333	1.8363889	0.979	e(c)
4055	187.3573750	1.8601056p	0.968	k
3301	187.3466250	1.8502667	0.969	e(c)
4155	187.3885500	1.8644889	0.969	k+a
5411	187.3718958	1.8717778	0.974	k
20008	187.3734583	1.8726667	0.973	e(a)
3497	187.3724875	1.8579083	0.982	a+k
20010	187.3726625	1.8579944	0.977	k
4126	187.3900292	1.8628750	0.973	k
3507	187.3716250	1.8571444	0.976	k
20013	187.3684167	1.8559167	0.979	k
20014	187.3654583	1.8485556	0.969	k
3949	187.3696083	1.8602611	0.976	k
30004	187.3697875	1.8601389	0.970	k
3495	187.3715708	1.8582111	0.980	k
3524	187.3807000	1.8676667	0.969	a+k
5499	187.3844542	1.8685722	0.973	k
3205	187.3747292	1.8461806	0.984	a+k
4661	187.3631292	1.8977194	0.975	k+a
5001	187.3500083	1.8870944	0.973	k
4956	187.3367208	1.8890611	0.978	k
4794	187.3342500	1.8927333	0.974	k
4910	187.3213042	1.8925528	0.976	e(b)
4800	187.3186708	1.8948944	0.976	k

The observations were taken in March 2007, as part of the NIR follow-up of the XDCP survey programme. The instrument was operated in the *Large field* mode, corresponding to a 5x5 arcmin Field of View (FoV), with a pixel scale of 0.288 arcsec/pix. Since the NIR background is generally highly variable, a large dithering

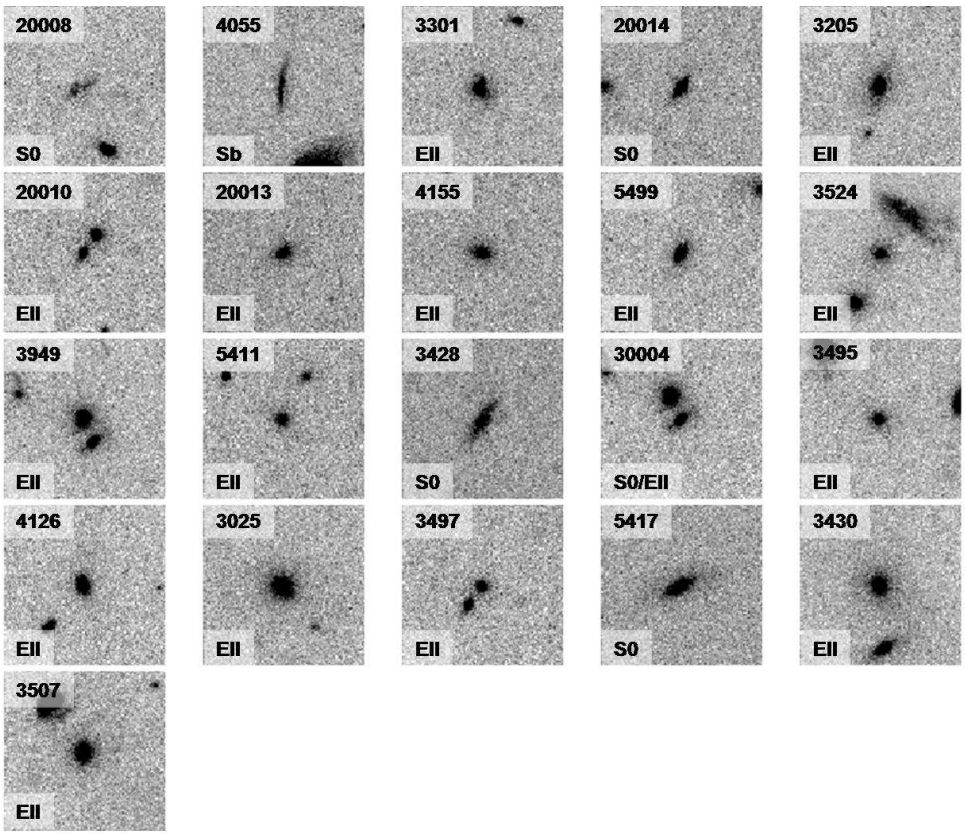

Figure 6.4: i_{775} image gallery of the 21 spectroscopically confirmed members in the ACS FoV, ordered in increasing i_{775}-z_{850} color. Individual stamps are centered on the cluster members and have a size of 5" x 5". Top labels correspond to the spectroscopic galaxy ID and bottom labels refer to the visual morphological classification.

pattern has to be applied; we set the automatic jitter box to a width of 30 arcsec. Total exposure times amount to 1hr in Ks and 45 min in J. The J-band data have a seeing of 0.98" whereas the Ks-band have an image quality of 0.69".

Photometric calibration standards (Persson et al. (1998)) were acquired several times during the observation run. The zero points (ZP) were computed using the reduced standards (background subtracted, count rate image) with the following relation:

$$ZP = mag + 2.5log(countrate) + atm_{corr} * airmass \tag{6.1}$$

where mag refers to the standard star magnitude, and atm_{corr} refers to the wave-

length dependent atmospheric correction. The stellar flux was measured within circular apertures with 6" radius; such a large radius ensures that we account for the bulk of the flux. The background was estimated with a 3σ clipping algorithm. The scatter of the zero points is 0.015 mag and 0.04 mag for the J and Ks filter, respectively. We converted VEGA magnitudes to the AB photometric system with the ESO web-tool available at $http://archive.eso.org/apps/mag2flux$.

The data was reduced with the package ESO/MVM (Vandame (2004)) using the HST/ACS catalog to match the astrometry. We used SExtractor (Bertin & Arnouts (1996)) in *dual image mode* to perform the source detection in the Ks-band, and the photometry of both images.

6.3 Structural analysis

6.3.1 Surface brightness profile fitting

The radial surface brightness profiles of galaxies can be described by the Sersic law (Sersic (1968)),

$$\Sigma(r) \propto exp(r/r_e)^{1/n} - 1 \tag{6.2}$$

where $\Sigma(r)$ is the surface brightness at radius r, the Sersic index, n, characterizes the degree of concentration of the profile; and the effective radius, R_e, corresponds to the projected radius enclosing half of the galaxy light.

Using the ACS data we made a 2D bulge/disk galaxy decomposition with the software GIM2D (Simard et al. (2002)). The galaxy model is the sum of a bulge component (Sersic profile) and an exponential disk, depending on a total of eleven parameters. Of these parameters, three describe the shape of the Sersic profile, including the index n, which we constrained to $0< n <4$. The upper bound is introduced because larger values of n usually do not improve the fit much, however the covariance between n and R_e can lead to an overestimate of R_e for large n (Blakeslee 2006), and also because n=4 corresponds to the de Vaucouleurs profile, a purely empirical fit to the profiles of elliptical galaxies and bulges (de Vaucouleurs (1961)). For each passband we constructed empirical Point Spread Functions (PSFs) by computing the median profile of a handful of stars in the science images. The resulting PSFs were convolved with the 2D models to fit the galaxies.

The median Sersic index n of the spectroscopically confirmed galaxies is 3.9 and the median effective radius is 5.5 pixel (0.28") (see 6.5). The R_e and n distributions in the i-band are consistent with the ones measured in the z-band, within the 1σ errors as shown in the comparison between the R_e (i_{775}) and R_e (z_{850}) in Fig. 6.6. The reduced χ^2 of the best-fit models is ∼1 for the majority of the galaxies, emphasizing the quality of the fit.

We also fitted the sample of color-selected galaxies located in the red-sequence

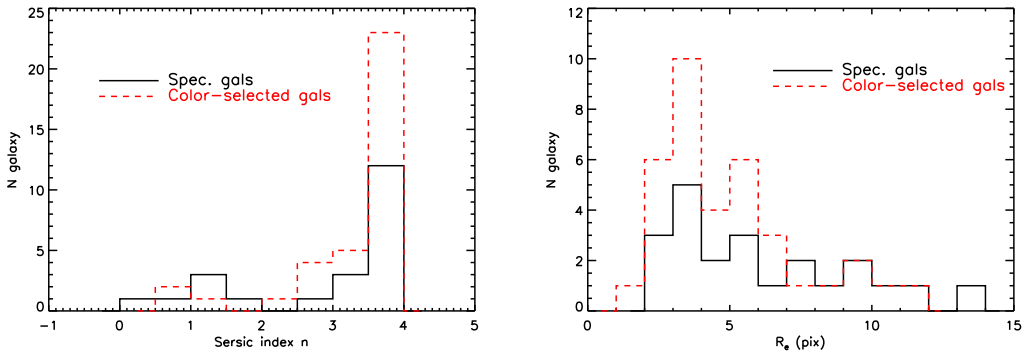

Figure 6.5: Distribution of the morphological fit parameters, Sersic index (*left*) and effective radius (*right*), of the cluster members (black solid line) and color-selected galaxies (red dashed line) using the ACS/i_{775} band.

(see Sect. 4.2) and present the R_e and n distributions in Fig. 6.5. These galaxies have an overall smaller effective radius in comparison with the cluster members, with a median value of 4.2 pix, which is expected since they are also fainter. Their n distribution is however similar to the values obtained for the spectroscopic sample, indicating a predominance of concentrated profiles, likely to be elliptical galaxies.

6.3.2 Visual morphological classification

In addition to the profile fitting, we made a visual classification of the spectroscopic members and color-selected galaxies, using morphological templates from M. Postman. In Fig. 6.4 we show postage stamps of the cluster members in the i_{775} passband labelled with the morphological type. We note two pre-merging red galaxy pairs (ID=20010/3497, 30004/3949).

The morphology of the spectroscopic galaxies in XMM1229 is clearly dominated by elliptical galaxies (15/21) with only one galaxy classified as spiral (ID=4055), unlike other distant clusters (see for eg. the EDisCS high-redshift sample, z$\leq$0.8, De Lucia et al. (2004)). The remaining five cluster members are classified as S0's. The color-selected sample is morphologically very similar to the spectroscopic members, with 32/36 galaxies classified as ellipticals, the remaining ones as S0's.

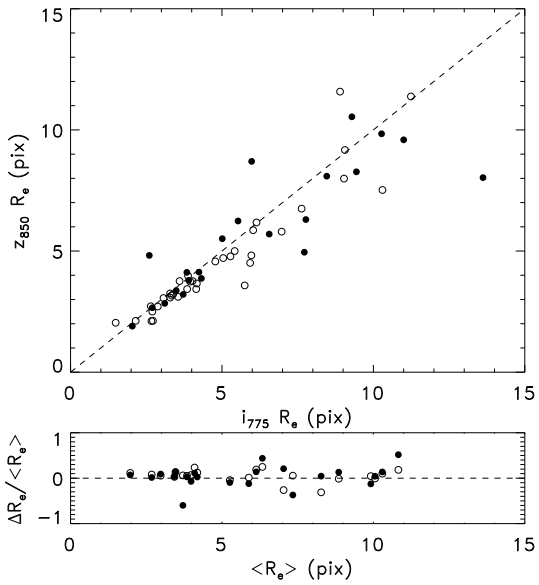

Figure 6.6: Comparison of the R_e obtained with GIM2D in the i_{775} and z_{850} bands. Spectroscopic members are represented in solid circles and color-selected galaxies are shown in open circles. The dashed line indicates the one-to-one relation. The bottom plot shows the difference in the R_e values for the two bands normalized by the average R_e. The dashed line represents the constant zero value.

6.4 The $i_{775} - z_{850}$ color-magnitude relation

6.4.1 Galaxy photometry

We use SExtractor in *dual image mode* to perform the source detection in the z_{850} band, and the photometry in both bands. The image quality of the i_{775} band is sightly better than the z_{850} band, with a FWHM of the PSF of 0.085“, as opposed to 0.095” in the z_{850}. The effect of the z_{850} PSF broadening has been investigated in other works and is attributed to the long-wavelength halo of the ACS/WFC (Sirianni et al. (2005)). This effect, although small, bears implications on the galaxy color measurement and has to be accounted for. We analyze the differential PSF blurring by selecting a few stars for which we measure growth curves normalized to the central intensity. We obtain a differential (z_{850}-i_{775}) median radial profile that shows a steep behavior for radii smaller than 3 pix - see Fig. 6.7.

The $i_{775} - z_{850}$ color is determined in small apertures to avoid intrinsic galaxy color gradients. We choose a fixed aperture of 5 pix since at this radius the PSF broadening is no longer dominant (see Fig. 6.7), and we apply a correction of 0.034

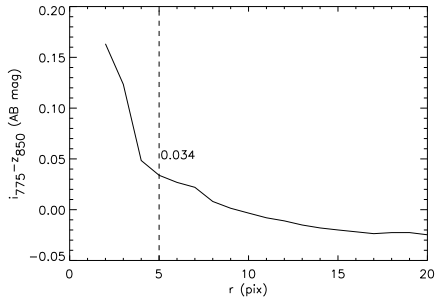

Figure 6.7: Differential PSF blurring effect in i and z-bands: at r=5 pix (0.25“) the PSF correction is 0.034 mag (vertical line).

mag to the i_{775} band in order to match the poorer seeing of the z_{850} band. Total z_{850} band magnitudes are obtained with SExtractor parameter `MAGAUTO`.

The color-magnitude relation is presented in Fig 6.8. We flag the 35 confirmed interlopers (green triangles), since nearly a fourth of them (9/35) are located on the red-sequence.

Further to the spectroscopic sample, we are interested in studying all galaxies situated on the red-sequence. In order to do this we perform a robust linear fit using bisquare weights to the CMR of the confirmed passive members. The linear fit has a slope of -0.039 and a zero point CMR_{ZP}=0.861±0.038, which was determined with a bi-weighted mean. The scatter of the CMR including only the passive galaxies is 0.039 mag.

The criteria to select the red-sequence galaxies are the following: (*i*) galaxies with a i_{775}-z_{850} color in the area defined by CMR_{ZP}±3.0.038, (*ii*) brighter than z_{850} mag=24 (since the characteristic magnitude M_* is about 22 mag at the cluster redshift) and (*iii*) within a radius of 1.5 arcmin from the cluster center, defined by the X-ray emission. A total of 36 galaxies meet these criteria.

6.4.2 Model color-magnitude relation

To avoid dealing with the PSF blurring affecting the color measurement, we explored a new strategy to obtain i_{775}- and z_{850}-band magnitudes. Using the surface brightness best-fit models, in which the PSF deconvolution is already taken care of, we use the output model adding gaussian noise, to measure aperture and total magnitudes. Similarly to the "data" CMR, the color measurements are performed in fixed apertures with r=5 pix (0.25"). Integrating over the effective radius proved unreliable since, for many galaxies R_e is smaller than 3 pix, which is really too small to make a proper color measurement - noise, explain. Total magnitudes were derived using

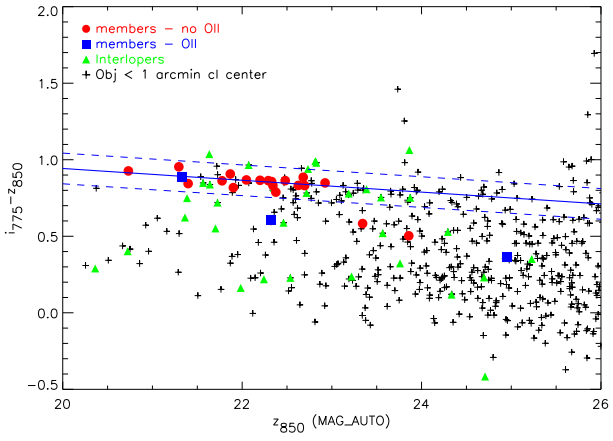

Figure 6.8: i_{775}-z_{850} color-magnitude relation of XMM1229. The black solid line refers to the linear fit to the passive cluster members shown in red circles. The dashed lines correspond to the 3-σ confidence region. The galaxies with OII emission are displayed in blue squares. Green triangles refer to interlopers.

apertures with radius of $10\times R_e$ instead of using SExtractor `MAGAUTO`, which we found to be inaccurate in comparison with large aperture magnitudes. These discrepancies are visible in the total z_{850} magnitude of the brightest galaxies in the two CMR's represented in Figs. 6.8 and 6.9.

The procedure to fit the CMR and obtain its zero point is identical to the method described earlier for the "data" CMR, only that now we use both the early-type cluster members and the color selected red-sequence galaxies. The fit results are the following: CMR_{ZP}=0.814±0.038, the slope is -0.045±0.008 and the scatter is 0.055±0.014. If we consider only the confirmed passive members in the linear fit we obtain a zero point CMR_{ZP}=0.829±0.041, the slope flattens to -0.031±0.016 and the scatter decreases to 0.042 ± 0.011. The error of the scatter is estimated with Monte Carlo simulations of the galaxy models, varying the Sersic index and the effective radius within the 1-σ confidence errors.

The scatter in the color-magnitude relations derived from SAM is obtained by computing the total galaxy magnitudes - which is precisely known in simulations - and is a factor 2-3 larger than our observational scatter (see for e.g. Menci et al. (2008)). A possible reason for this difference is the existence of color gradients which are taken into account in the total galaxy magnitudes used in SAM to measure the scatter, whereas in the observations we limit the color measurement to a small central aperture, being more insensitive to such gradients. To investigate this problem we measured the galaxy colors in increasing fixed radii (r=10,15 pix) and obtained a cor-

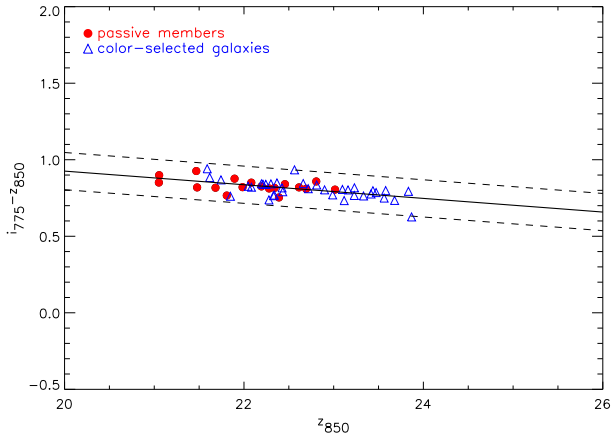

Figure 6.9: i_{775}-z_{850} color-magnitude relation of XMM1229 using the best-fit galaxy models. The black solid line refers to the composite linear fit to both the passive cluster members (red circles) and the color-selected galaxies (blue triangles). The dashed lines correspond to the 3-σ confidence region.

responding scatter of 0.077, 0.099, respectively. The observed increasing scatter goes in the direction of the results obtained with simulations, however a more thorough analysis is needed to confirm this result.

6.5 The NIR color-magnitude relation

Although the quality of the ground-based data is inferior with respect to the HST/ACS data, we nevertheless present the NIR CMD for completeness. The J-Ks color is measured in apertures with 4 pix (1.16“) radius. Smaller apertures would likely output noisy values, and we considered that, for example in Lidman et al. (2004) data of similar quality was used to derive the CMD of a cluster at z=1.235 using apertures with r=3 pix. We matched the Ks-band to the seeing of the J-band with the method described in Sect. 6.3.1. At the radius r=4 pix we need to decrease the flux of the K-s-band objects by an equivalent magnitude of 0.03 mag. The galactic extinction was accounted for by applying corrections of 0.015 and 0.006 mag in the J- and Ks-band respctively, derived from $E(B-V)$= 0.017. We obtained total Ks magnitudes with the SExtractor parameter `MAGAUTO` and we perfomed a linear fit to the passive spectroscopic members. The zero point of the color-magnitude relation was obtained by computing the biweighted mean of the spectroscopic members J-Ks color. The linear fit has a slope of -0.06 and the CMD_{NIRZP} is 0.971 (see Fig. 6.10).

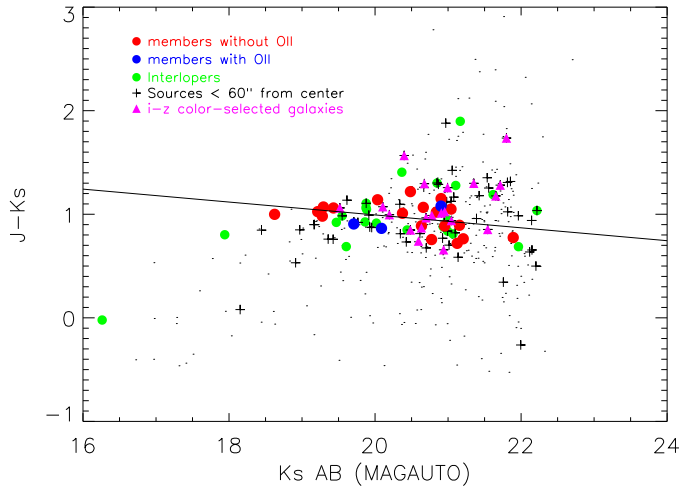

Figure 6.10: J-Ks Color magnitude relation. Spectroscopic passive members are shown in red circles; members presenting OII emission are shown in blue; and interlopers are in green. Magenta triangles refer to the i-z color selected galaxies, and the sources within 1 arcmin distance from the cluster center are represented by crosses.

6.6 Analysis of the spectral energy distributions

The observed spectral energy distribution of a galaxy is a record of its stellar population history. The SED fitting method relies on the comparison of the observed SED with synthetic SED's. The latter are then convolved with the transmission curves of the filters used in the observations and the output magnitudes are compared with the observed magnitudes. Galaxy SED's were determined by measuring the flux within a fixed aperture of 3 arcsec in the four available passbands.

There are 20 spectroscopic members common to the FoV of SOFI and ACS, however, four of the confirmed members are found in two red galaxy pairs that are not properly resolved in the NIR data. For this reason we had to leave them out of the spectral analysis.

Only four of the remaining 16 studied galaxies show OII emission lines (IDs: 3025, 3205, 3301, 4055) signaling ongoing star formation, and the first two also present OIII lines. The first three galaxies have been visually classified as ellipticals, although galaxy 3301 has a low Sersic index, n=1.5. Galaxy ID=4055 is an edge-on spiral which is reflected in the low Sersic index (n=1.2). These four galaxies will be refered to as late-type galaxies hereafter.

Additionally, we also constructed SEDs of the i_{775}-z_{850} color-selected galaxies lying on the ACS CMR red sequence. As mentioned earlier, we find 36 galaxies in the locus of the red-sequence. The poorer quality of the NIR data can only resolve 20 of these galaxies.

Given the large disparity in the resolution of the ground- and space-based data, a careful matching of the different PSFs must be done, when constructing the multi-wavelength catalog for sampling the galaxies' SEDs. The method we used to derive aperture corrections is the following: we smoothed the i_{775}, z_{850} and Ks-band images with gaussian kernels to match the seeing of the J-band ($\sim$1") and made growth curves of stars in the original and degraded (smoothed) images. We then obtained a differential median radial profile for each band with which we derive corrections at a given radius. In the multi-color catalog we use galaxy magnitudes corrected to match the fluxes to the worst seeing image (J-band), measured within 0.5" radius apertures for the ACS bands, and 1.16" for the NIR data. We opted to work with magnitudes extrapolated to 3" radius, which safely enclose the bulk of the galaxy flux.

6.6.1 Spectrophotometric properties: masses, ages

Stellar masses, ages and star formation histories are derived from the synthetic galaxy fluxes, assuming solar metalicity and a Salpeter (Salpeter (1955)) initial mass function (IMF), with a mass cut off [0.1-100] M$\odot$. We perform a three parameter (age T, τ, mass) fit to the SEDs using a grid of Bruzual & Charlot (2003) models characterized by a delayed exponential star formation rate: $\frac{t}{\tau^2}.exp(\frac{-t}{\tau})$, performing a minimization of the χ^2. The parameter τ spans a range of [0.2- 5.8] Gyr, where 5.8 Gyr is the age of Universe at the cluster redshift. As an example, in Fig. 6.11 we present the fit to the SED of 3025, one of the three brightest galaxies (see Sect.6), together with the filter transmission curves.

The star formation weighted age (SFR age) represents the mean age of the bulk of the stars in a galaxy (depending on the τ parameter), and is defined as:

$$t_{SFR} = \frac{\int_0^T dt'(T-t')\Psi(t')}{\int_0^T dt'\Psi(t')} \tag{6.3}$$

where Ψ is the star formation rate as described in Gobat et al. (2008). Galaxy SFR ages do not change significantly if other models (Maraston (2005)) and different IMF's are used (Chabrier (2003), Kroupa & Weidner (2003)), however the stellar masses are dependent on the chosen IMF.

The spectroscopic cluster members form a fairly old population, with a median SFR age of 4.3 Gyr, with stellar masses in the range 4×10^{10}-2.3 $\times10^{11}$ M$_\odot$. With the color-selected sample we are probing to fainter galaxies, with a median mass=6.4 $\times10^{10}$ M$_\odot$, however, since we do not have redshifts for these galaxies, we cannot make strong conclusions about their masses and formation ages.

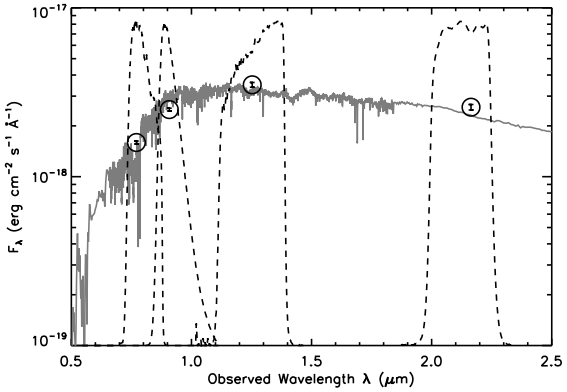

Figure 6.11: SED fit of one of the three brightest galaxies, ID=3025 (solid line). The flux measurements in the i_{775}, z_{850}, J and Ks-bands (respectively from left-to-right) are shown in circles, with 1-σ error bars, along with the filters transmission curves (dashed lines).

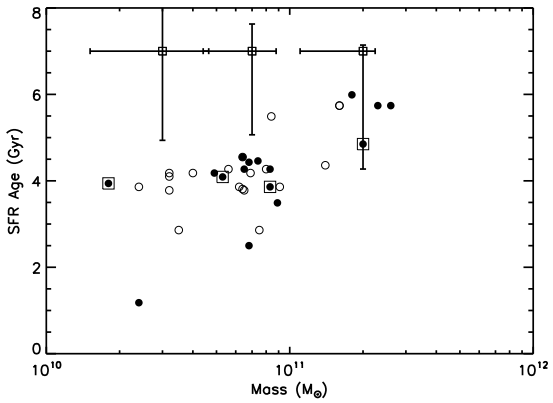

Figure 6.12: Photometric masses of the 16 spectroscopic cluster galaxies (filled circles) and 20 color-selected galaxies (open circles) as a function of their star formation weighted ages. Spectroscopic members with OII emission or morphologically classified as late-type galaxies are signaled with square symbols. Mean error bars corresponding to three mass bins (bin1: m $<4.5\times10^{10}$, bin2: 4.5×10^{10} < m $<1\times10^{11}$, bin3: m $>1\times10^{11}$, with m in solar masses) are shown on the top.

In Fig. 6.12 we show the correlation between the star formation weighted age and stellar mass content in both the spectroscopic (filled circles) and color-selected sam-

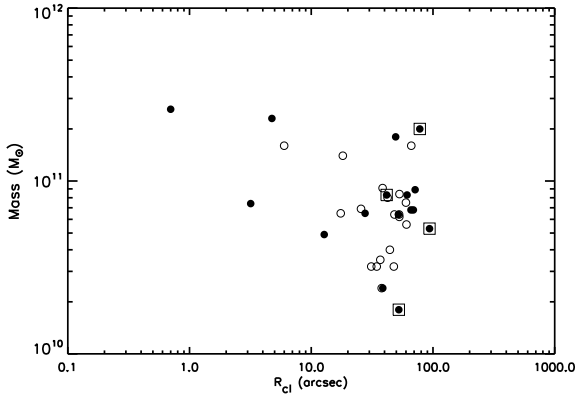

Figure 6.13: Correlation between photometric mass and radial distance to cluster center. Spectroscopic members with OII emission or morphologically classified as late-type galaxies are signaled with square symbols.

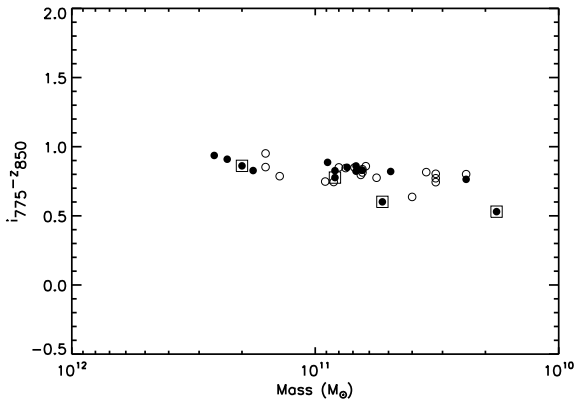

Figure 6.14: Correlation between galaxy $i_{775} - z_{850}$ color and photometric mass. Spectroscopic members with OII emission or morphologically classified as late-type galaxies are signaled with square symbols.

ples (open circles). This correlation evidences an anti-hierarchical behavior (downsizing), where the most massive galaxies are also the oldest.

We find a dependence of the galaxy radial distance to the cluster center with mass, in which the most massive galaxies populate the cluster core (see Fig. 6.13). (add references to similar results). Furthermore, the four late-type galaxies are situated in

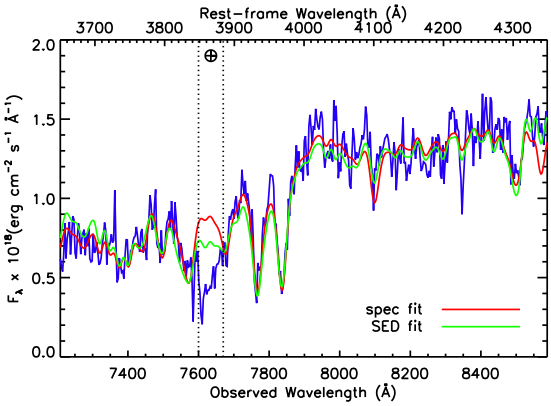

Figure 6.15: Stacked spectrum (in blue) of all passive members which do not show strong H_δ absorption (k type, see Table 6.4). The red line refers to the best-fit model to the stacked spectrum and the green line refers to the best-fit model to the average SED. The region around the atmospheric A-band at 7600 Å(dashed lines) is difficult to subtract and was therefore ignored in the fit.

the cluster's outskirts, at about 1 arcmin from the center, indicating star formation taking place in these regions.

We also investigate the relation between the $i_{775}-z_{850}$ color and the mass (Fig. 6.14) and we observe the expected trend of the most massive galaxies being redder.

6.6.2 Star formation histories

The spectra of 12 confirmed passive members were coadded to obtain the stacked spectrum. However, four (ID=3428, 3524, 4155 and 5417) of these 12 galaxies have strong H_δ absorption, EW(H_δ) ≥ 3 (these are a+k/k+a spectral types, see Table 6.4) and therefore we removed them from the stacking procedure. Three of these galaxies are at about 1 arcmin from the X-ray cluster center and only galaxy (ID=3428) is closer to the core, at ~ 0.5 arcmin from the center. In Fig. 6.15 we present the coadded spectrum of 8 spectroscopic passive members with weak or no H-delta absorption. The best-fit SED is shown in green and the spectral fit is shown in red.

Star formation histories were derived only for the eight galaxies which do not have significant H_δ absorption. The star formation weighted age and formation redshift obtained by the best fitting models (i.e. those within the 3-σ confidence), is $3.7\ ^{+0.4}_{-0.5}$ Gyr and $z_f = 3.0 \pm 0.5$ respectively, when using the combined spectrophotometric data.

Table 6.5: Properties of the three brightest galaxies. The information given is the following: galaxy ID (column 1), total z_{850} magnitude from best-fit model (column 2), distance to the X-ray cluster center (column 3), photometric mass (column 4), star formation weighted age (column 5).

ID	$\mathbf{z_{850}}$**mag**	**dist [arcsec]**	**Mass** [10^{10} $\mathbf{M_\odot}$]	**Age [Gyr]**
(1)	(2)	(3)	(4)	(5)
3025	21.051	78	20^{+6}_{-9}	$4.85^{+0.89}_{-2.36}$
3430	21.055	5	23^{+3}_{-11}	$5.74_{-2.84}$
3507	21.468	1	26^{+3}_{-11}	$5.74_{-2.50}$

6.7 Is there a Brightest Cluster Galaxy?

The cores of rich galaxy clusters most often host a massive and bright giant elliptical galaxy - the brightest cluster galaxy (BCG). In XMM1229, instead of one prominent BCG, we find three brightest galaxies within $\sim$ 0.5 mag. The total z_{850}-band magnitudes are derived by integrating the best-fit surface brightness model to a large radius, r=10$\times R_e$. In Table 6.5 we summarize the most relevant characteristics of these galaxies. As expected, the three BCGs are the most massive galaxies, with masses of the order of 2 $\times 10^{11}$ $M_\odot$. The galaxy ID=3025 located at 1.3“ from the cluster center shows strong OII emission, indicating ongoing star formation which is confirmed by a lower star formation weighted age of 4.85 Gyr, approximately 1 Gyr younger than the other two brightest galaxies. In addition, this galaxy is fainter by $\sim$ 0.2 mag in Ks and $\sim$ 0.15 mag in J, with respect to the other two BCGs.

6.8 Discussion and conclusions

XMMU J1229+0151 is a rich galaxy cluster with redshift z=0.975 which makes it an adequate laboratory for studying galaxy evolution. With the high quality ACS imaging data combined with the FORS2 spectra we derived accurate galaxy photometry, and the additional NIR J- and Ks-bands allowed us to make an SED analysis.

From the X-ray spectral analysis we obtained a global cluster temperature of 6.3 keV and a luminosity $L_x[0.5-2.0]keV$=1.3 $\times 10^{44}$ erg s^{-1}, indicating that XMM1229 is a massive cluster. Fixing the redshift to the spectroscopic value we obtain the metal abundance $Z/Z_\odot = 0.34\ ^{+0.14}_{-0.13}$.

With the aid of morphological templates published in Postman et al. (2005) we made a visual classification of the cluster galaxies. This method indicates a predominance of ellipticals in both the spectroscopic sample (15/21) and in the color

selected sample (32/36). Five cluster members are classified as S0 Only one galaxy is clearly a spiral type and two galaxy pairs appear in a stage of pre-merging. In addition to this qualitative assessment we also fitted Sersic models to the surface brightness profiles of the two galaxy samples. The best-fit model parameters n and R_e are in good agreement with the visual classification as the n distribution peaks at 3.9 suggesting a majority of bulge dominated galaxies. The median effective radius is 0.275“, approximately the radius chosen for measuring the i_{775}-z_{850} color (r=0.25”).

Two methods were explored to construct the CMR: (*i*) the 'standard' method in which we correct the different PSF's of the i_{775} and z_{850} bands, and (*ii*) an alternative approach using the best-fit galaxy models, in which the PSF is already deconvolved. The CMR at this high redshift is found already to be very tight, with a scatter of 0.05 ±, similar to the local Coma cluster thus confirming that cluster ETGs in clusters assembled early on and in short timescales. The scatter of the red-sequence is essentially the same from these two independent methods, showing that the second method is robust against uncertainties arising from PSF corrections. The slope of the red-sequence including only the cluster members is -0.031±0.016, steepening to -0.045±0.008 when accounting also for the color-selected galaxies. These results are in agreement with Mei et al. (2006) and Blakeslee et al. (2003) (quote value), who also showed that the CMR scatter and slope vary slightly with redshift.

The spectrophotometric analysis shows a red-sequence populated by moderately massive galaxies, with a median stellar mass of 7.4 $\times 10^{10}$ $M_\odot$. The combined SED + spectral fit to the stacked spectrum of the passive members allowed us to constrain the ages of the ETGs to 3.7 $^{+0.4}_{-0.5}$ Gyr, and a formation redshift $z_f = 3.0 \pm 0.5$.

These results indicate that star formation in the cluster ETGs have completed most of the chemical enrichment, which is confirmed by the high metal abundance of the ICM, $Z/Z_\odot = 0.34$.

The correlation between stellar mass and galaxy age favors an anti-hierarchical behavior where the most massive galaxies are the oldest, which also tend to be closer to the cluster core (Figs. 6.12, 6.13).

Acknowledgements

We acknowledge the excellent support provided by the staff at the Paranal observatory. In particular, we wish to acknowledge their assistance in setting up the observations with the MXU mode of FORS2 when technical problems prevented us from using the MOS mode. JSS would like to thank D. Pierini for useful discussions. JSS is supported by the Deutsche Forschungsgemeinschaft under contract BO702/16-2. This research has made use of the NASA/IPAC Extragalactic Database (NED) which is operated by the Jet Propulsion Laboratory, California Institute of Technology, under contract with the National Aeronautics and Space Administration.

7
Conclusions

Everything is just an impression. Monimus

Galaxy clusters are remarkable systems since they are representative of the matter content of the Universe. While these objects are dominated by a dark matter halo, most of their baryonic content, observed in the form of a hot X-ray emitting plasma and galaxy stellar light, is governed by complex non-gravitational processes that affect (sometimes dramatically) the structure of clusters.

The detailed study of such systems especially those at high redshift, with multi-wavelength observations, offers an excellent opportunity to study non-trivial physical processes which shape the population of these massive "island universes", and contribute to the understanding of the history and mapping of large-scale structures.

In this thesis, I have studied high-redshift X-ray selected galaxy clusters and their underlying stellar populations. I have thus probed both, the ICM through X-ray imaging, and the galaxy populations with optical & NIR imaging and spectroscopy.

High-redshift studies are imperative to increase the leverage on the constraints regarding the timescales of the physical processes that drive the formation and evolution of clusters. However, good quality data and robust methodologies are essential to optimally extract information from these low contrast systems, with small extend on the sky.

In Chapter 4, I present the first conclusive investigation on the abundance of cool cores in the most distant cluster sample currently available. Radiative cooling in the cores of clusters has been a debated topic in the past few years, due to discrepancies between the observations and the model expectations, based on steady state cooling.

Tracing the fraction of cool cores with redshift is important not only to the understanding of the cooling and feedback mechanisms responsible for the appearance of cool core clusters, but it is also necessary to improve the X-ray scaling relations which present deviations from self-similarity due to CCs. This investigation also has an impact in the derivation of cosmological parameters with galaxy clusters: Can clusters be treated as standard candles? Do we have a fair knowledge on the regularity of the cluster population?

The analysis undertaken is based on the surface brightness of a statistically representative sample of clusters with $0.7 < z < 1.4$ - the highest redshift bin currently reachable - using *Chandra* images. A central surface brightness excess emission is one of the most robust indicators of cooling. We therefore defined a surface brightness concentration, c_{SB}, a phenomenological parameter that efficiently segregates three categories of cooling: strong, mild and non-cool cores, based on a control low-z sample. This parameter shows that the majority of the distant clusters present mild cool cores, although no significant strong cool core was found. The azymuthally averaged SB profiles scaled according to the empirical scaling law, confirmed this result. Furthermore, the analysis of the central cooling time t_{cool} is in agreement with this finding, indicating that 10/15 distant clusters have t_{cool} smaller than the Hubble time. In addition t_{cool} strongly correlates with c_{SB} (Santos et al. (2008)). A comparison of our results with cosmological simulations can provide new constraints to cluster formation scenarios.

Within the scope of the XMM-Newton Distant Cluster Project, I have observed and analyzed 22 cluster candidates using a I- and H-band photometric technique. This work included the preparation of the observations, participating in the observing runs at ESO/La Silla and performing the data reduction. I also prepared spectroscopic observations for VLT/FORS2 of several candidates. I present the NIR and optical reduction of these 22 targets. These sources have now an identification probability as distant clusters, with about half of the systems being good, promising cluster candidates. This is an important step to select the prospective objects for the next expensive identification and redshift measurement stage, with spectroscopy. It is also a crucial step to assess the completeness and efficiency of the survey. The impact of these results still has to be assessed during the coming months when spectroscopic observations covering part of the sample will also be analyzed. Nevertheless it already appears that about half of these candidates will be z$\geq$0.8 clusters, based on their I-H color (Chapter 5).

The formation and evolution of massive elliptical galaxies - the building-blocks of massive galaxy clusters - was investigated with an exceptional multi-wavelength dataset, composed of HST/ACS and SOFI+EMMI/NTT imaging, and FORS2/VLT

spectroscopy, of a rich, X-ray luminous cluster at z=0.975, XMMU J1229+0151, discovered in the XDCP (Chapter 6). Up to now, only a few high-quality datasets of distant clusters are currently available, therefore this is a valuable contribution to the study of the properties of galaxies in high density environments at z$\sim$ 1. The FORS2 spectroscopy secured 27 cluster members, 21 of which are within the FoV of ACS. This spectroscopic sub-sample was visually classified (Postman et al. (2005)) using the ACS data. Additionally, we performed a morphological analysis by fitting Sersic models to the surface brightness profiles of the galaxies. We find that 15/21 members are elliptical galaxies and the Sersic index n correlates well with the visual classification. The $i_{775} - z_{850}$ color-magnitude diagram shows that the passive members form a tight red-sequence with a scatter of only 0.04 mag. This value lends further evidence to other ACS studies of distant clusters (e.g., Mei (2008)), suggesting no strong evolution of the scatter of the CMR with redshift, in the range [0.8-1.2]. The fit to the spectrophotmetric data with spectral synthesis models yields an average formation redshift $z_f \sim$ 3-4 of the ETGs, with stellar masses in the range 5×10^{10} - 2×10^{11} $M_{\odot}$. Furthermore, the high iron abundance of this cluster, $Z/Z_{\odot}=0.34\pm0.13$, which augment the sample of distnat clusters with reliable measurements of metallicity (Balestra et al. (2007)), shows that the chemical enrichment of the ICM was completed at much earlier cosmic epochs with respect to the cluster redshift, consistently with the star formation history and ages derived for the ETGs in this cluster at z$\sim$1.

In this work we found indications for clusters with redshift up to 1.4 still displaying a relaxed state, both in terms of the intracluster medium which shows signs of mild central cooling, but also by probing the stellar content of clusters, where a large fraction of galaxies is already undergoing passive evolution, and must have formed at $z \gtrsim 3$ with a high degree of synchronicity.

To firmly constrain the epoch of formation of the first X-ray clusters we need to perform detailed analysis of a larger sample of z$\geq$1 clusters, and to push observations to even higher redshifts. Multi-wavelength studies are the best approach to reach a unified picture of the cosmic baryons in their different phases (hot gas, "cold" galaxies), although advances in instrumentation and observational techniques are required in order to meet the challenge of exploring the most distant clusters.

8
Outlook

Following the work developed in this thesis to study the evolution of Cool Core Clusters (Chapter 4 and Santos et al. (2008)), I intend to investigate further this issue via an independent spectroscopic analysis of H_α emission in distant clusters, which, if present, would indicate that radiative cooling is taking place.

In the context of the co-evolution of baryons in the hot (ICM/X-rays) and cold (galaxy populations/optical) phase at intermediate redshift, I plan to study the interplay between star formation properties and the state of the intracluster gas in merging systems. We will investigate the most famous merging cluster, the Bullet Cluster (Clowe et al. (2006), Markevitch (2006)), using a rich dataset composed of ACS and WIFI imaging, the 1 Msec Chandra exposure, in addition to extensive VIMOS spectroscopy.

The completion of the imaging and spectroscopical follow-up of the XDCP cluster candidates has provided us with a wealth of multi-wavelength data which will be reduced and interpreted in the near future, with the purpose of characterizing the high-z cluster population.

I will take a post-doc position at the *Osservatorio Astronomico di Trieste* where, in addition to these projects, I will be involved in a search for serendipitous clusters of galaxies from the SWIFT X-ray Telescope (XRT) archive. The goal of this survey is to compile a complete new sample of $z>1$ clusters and $z<0.3$ groups, to address

two main scientific issues: (*i*) the evolution of the iron abundance; (*ii*) the entropy distribution in groups where the effect of non gravitational processes is expected to be larger than in clusters.

References

Allen, S. W., Ettori, S., Fabian, A. C. (2001), MNRAS, 324, 877

Allen, S. W., Rapetti, D. A., Schmidt, R. W., Ebeling, H., Morris, R. G., Fabian, A. C. (2008), MNRAS, 383, 879

Anders, E., Grevesse, N. (1989), Geochim. Cosmochim. Acta, 53, 197

Appenzeller, I., Fricke, K., Fürtig, W., Gässler, W., Häfner, R., Harke, R., Hess, H.-J., Hummel, W., Jürgens, P., Kudritzki, R.-P., Mantel, K.-H., Meisl, W., Muschielok, B., Nicklas, H., Rupprecht, G., Seifert, W., Stahl, O., Szeifert, T., Tarantik, K. (1998), The Messenger, 94, 1

Arabadjis, J. S., Bautz, M. W., Garmire, G. P. (2002), ApJ, 572, 66

Arimoto, N., Yoshii, Y. (1987), A&A, 173, 23

Arnaud, K. A. (1996), in *Astronomical Data Analysis Software and Systems V*, edited by G. H. Jacoby, J. Barnes, volume 101 of *Astronomical Society of the Pacific Conference Series*, 17–+

Arnaud, M. (2005), in *Background Microwave Radiation and Intracluster Cosmology*, edited by F. Melchiorri, Y. Rephaeli, 77–+

Arnaud, M., Aghanim, N., Neumann, D. M. (2002), A&A, 389, 1

Arnaud, M., Evrard, A. E. (1999), MNRAS, 305, 631

Arnaud, M., Neumann, D. M., Aghanim, N., Gastaud, R., Majerowicz, S., Hughes, J. P. (2001), A&A, 365, L80

Arnaud, M., Pointecouteau, E., Pratt, G. W. (2005), A&A, 441, 893

Astier, P., Guy, J., Regnault, N., Pain, R., Aubourg, E., Balam, D., Basa, S., Carlberg, R. G., Fabbro, S., Fouchez, D., Hook, I. M., Howell, D. A., Lafoux, H., Neill, J. D., Palanque-Delabrouille, N., Perrett, K., Pritchet, C. J., Rich, J., Sullivan, M., Taillet, R., Aldering, G., Antilogus, P., Arsenijevic, V., Balland, C., Baumont, S., Bronder, J., Courtois, H., Ellis, R. S., Filiol, M., Gonçalves, A. C., Goobar,

A., Guide, D., Hardin, D., Lusset, V., Lidman, C., McMahon, R., Mouchet, M., Mourao, A., Perlmutter, S., Ripoche, P., Tao, C., Walton, N. (2006), A&A, 447, 31

Baldi, A., Ettori, S., Mazzotta, P., Tozzi, P., Borgani, S. (2007), ApJ, 666, 835

Baldry, I. K., Glazebrook, K., Brinkmann, J., Ivezić, Ž., Lupton, R. H., Nichol, R. C., Szalay, A. S. (2004), ApJ, 600, 681

Balestra, I., Tozzi, P., Ettori, S., Rosati, P., Borgani, S., Mainieri, V., Norman, C., Viola, M. (2007), A&A, 462, 429

Bauer, F. E., Fabian, A. C., Sanders, J. S., Allen, S. W., Johnstone, R. M. (2005), MNRAS, 359, 1481

Baum, W. A. (1959), PASP, 71, 106

Bender, R., Burstein, D., Faber, S. M. (1992), ApJ, 399, 462

Bernardi, M., Renzini, A., da Costa, L. N., Wegner, G., Alonso, M. V., Pellegrini, P. S., Rité, C., Willmer, C. N. A. (1998), ApJ, 508, L143

Bertin, E., Arnouts, S. (1996), A&AS, 117, 393

Bignamini, A., Tozzi, P., Borgani, S., Ettori, S., Rosati, P. (2008), ArXiv e-prints, 807

Blakeslee, J. P., Franx, M., Postman, M., Rosati, P., Holden, B. P., Illingworth, G. D., Ford, H. C., Cross, N. J. G., Gronwall, C., Benítez, N., Bouwens, R. J., Broadhurst, T. J., Clampin, M., Demarco, R., Golimowski, D. A., Hartig, G. F., Infante, L., Martel, A. R., Miley, G. K., Menanteau, F., Meurer, G. R., Sirianni, M., White, R. L. (2003), ApJ, 596, L143

Blakeslee, J. P., Holden, B. P., Franx, M., Rosati, P., Bouwens, R. J., Demarco, R., Ford, H. C., Homeier, N. L., Illingworth, G. D., Jee, M. J., Mei, S., Menanteau, F., Meurer, G. R., Postman, M., Tran, K.-V. H. (2006), ApJ, 644, 30

Böhringer, H., Collins, C. A., Guzzo, L., Schuecker, P., Voges, W., Neumann, D. M., Schindler, S., Chincarini, G., De Grandi, S., Cruddace, R. G., Edge, A. C., Reiprich, T. H., Shaver, P. (2002), ApJ, 566, 93

Böhringer, H., Mullis, C., Rosati, P., Lamer, G., Fassbender, R., Schwope, A., Schuecker, P. (2005), The Messenger, 120, 33

Böhringer, H., Schuecker, P., Guzzo, L., Collins, C. A., Voges, W., Cruddace, R. G., Ortiz-Gil, A., Chincarini, G., De Grandi, S., Edge, A. C., MacGillivray, H. T., Neumann, D. M., Schindler, S., Shaver, P. (2004), A&A, 425, 367

Böhringer, H., Schuecker, P., Guzzo, L., Collins, C. A., Voges, W., Schindler, S., Neumann, D. M., Cruddace, R. G., De Grandi, S., Chincarini, G., Edge, A. C., MacGillivray, H. T., Shaver, P. (2001), A&A, 369, 826

Böhringer, H., Schuecker, P., Pratt, G. W., Arnaud, M., Ponman, T. J., Croston, J. H., Borgani, S., Bower, R. G., Briel, U. G., Collins, C. A., Donahue, M., Forman, W. R., Finoguenov, A., Geller, M. J., Guzzo, L., Henry, J. P., Kneissl, R., Mohr, J. J., Matsushita, K., Mullis, C. R., Ohashi, T., Pedersen, K., Pierini, D., Quintana, H., Raychaudhury, S., Reiprich, T. H., Romer, A. K., Rosati, P., Sabirli, K., Temple, R. F., Viana, P. T. P., Vikhlinin, A., Voit, G. M., Zhang, Y.-Y. (2007), A&A, 469, 363

Böhringer, H., Voges, W., Huchra, J. P., McLean, B., Giacconi, R., Rosati, P., Burg, R., Mader, J., Schuecker, P., Simiç, D., Komossa, S., Reiprich, T. H., Retzlaff, J., Trümper, J. (2000), ApJS, 129, 435

Bouwens, R., Broadhurst, T., Silk, J. (1998), ApJ, 506, 557

Bower, R. G., Benson, A. J., Malbon, R., Helly, J. C., Frenk, C. S., Baugh, C. M., Cole, S., Lacey, C. G. (2006), MNRAS, 370, 645

Bower, R. G., Lucey, J. R., Ellis, R. S. (1992), MNRAS, 254, 589

Brüggen, M., Kaiser, C. R. (2002), Nature, 418, 301

Bruzual, G., Charlot, S. (2003), MNRAS, 344, 1000

Burenin, R. A., Vikhlinin, A., Hornstrup, A., Ebeling, H., Quintana, H., Mescheryakov, A. (2007), ApJS, 172, 561

Burns, J. O. (1990), AJ, 99, 14

Burns, J. O., Hallman, E. J., Gantner, B., Motl, P. M., Norman, M. L. (2008), ApJ, 675, 1125

Carroll, S. M., Press, W. H., Turner, E. L. (1992), ARA&A, 30, 499

Casali, M., Pirard, J.-F., Kissler-Patig, M., Moorwood, A., Bedin, L., Biereichel, P., Delabre, B., Dorn, R., Finger, G., Gojak, D., Huster, G., Jung, Y., Koch, F., Lizon, J.-L., Mehrgan, L., Pozna, E., Silber, A., Sokar, B., Stegmeier, J. (2006), in *Society of Photo-Optical Instrumentation Engineers (SPIE) Conference Series*, volume 6269 of *Presented at the Society of Photo-Optical Instrumentation Engineers (SPIE) Conference*

Cavaliere, A., Fusco-Femiano, R. (1976), A&A, 49, 137

Chabrier, G. (2003), PASP, 115, 763

Chen, Y., Reiprich, T. H., Böhringer, H., Ikebe, Y., Zhang, Y.-Y. (2007), A&A, 466, 805

Churazov, E., Forman, W., Jones, C., Böhringer, H. (2000), A&A, 356, 788

Clemens, M. S., Bressan, A., Nikolic, B., Alexander, P., Annibali, F., Rampazzo, R. (2006), MNRAS, 370, 702

Clowe, D., Bradač, M., Gonzalez, A. H., Markevitch, M., Randall, S. W., Jones, C., Zaritsky, D. (2006), ApJ, 648, L109

Cohn, J. D., White, M. (2005), Astroparticle Physics, 24, 316

Coles, P., Lucchin, F. (1995), Chichester: Wiley, —c1995

Cowie, L. L., Binney, J. (1977), ApJ, 215, 723

Cowie, L. L., Songaila, A., Hu, E. M., Cohen, J. G. (1996), AJ, 112, 839

Croston, J. H., Pratt, G. W., Böhringer, H., Arnaud, M., Pointecouteau, E., Ponman, T. J., Sanderson, A. J. R., Temple, R. F., Bower, R. G., Donahue, M. (2008), A&A, 487, 431

Danese, L., de Zotti, G., di Tullio, G. (1980), A&A, 82, 322

Dawson, K. (2009), in preparation

De Filippis, E., Sereno, M., Bautz, M. W., Longo, G. (2005), ApJ, 625, 108

De Lucia, G., Blaizot, J. (2007), MNRAS, 375, 2

De Lucia, G., Kauffmann, G., White, S. D. M. (2004), MNRAS, 349, 1101

De Lucia, G., Springel, V., White, S. D. M., Croton, D., Kauffmann, G. (2006), MNRAS, 366, 499

de Propris, R., Eisenhardt, P. R., Stanford, S. A., Dickinson, M. (1998), ApJ, 503, L45+

de Vaucouleurs, G. (1961), ApJS, 5, 233

Dekker, H., Delabre, B., Dodorico, S. (1986), in *Instrumentation in astronomy VI; Proceedings of the Meeting, Tucson, AZ, Mar. 4-8, 1986. Part 1 (A87-36376 15-35). Bellingham, WA, Society of Photo-Optical Instrumentation Engineers, 1986, p. 339-348.*, edited by D. L. Crawford, volume 627 of *Presented at the Society of Photo-Optical Instrumentation Engineers (SPIE) Conference*, 339–348

Demarco, R., Rosati, P., Lidman, C., Girardi, M., Nonino, M., Rettura, A., Strazzullo, V., van der Wel, A., Ford, H. C., Mainieri, V., Holden, B. P., Stanford, S. A., Blakeslee, J. P., Gobat, R., Postman, M., Tozzi, P., Overzier, R. A., Zirm, A. W., Benítez, N., Homeier, N. L., Illingworth, G. D., Infante, L., Jee, M. J., Mei, S., Menanteau, F., Motta, V., Zheng, W., Clampin, M., Hartig, G. (2007), ApJ, 663, 164

Dickey, J. M., Lockman, F. J. (1990), ARA&A, 28, 215

Dressler, A., Lynden-Bell, D., Burstein, D., Davies, R. L., Faber, S. M., Terlevich, R., Wegner, G. (1987), ApJ, 313, 42

Dressler, A., Smail, I., Poggianti, B. M., Butcher, H., Couch, W. J., Ellis, R. S., Oemler, A. J. (1999), ApJS, 122, 51

Edge, A. C., Frayer, D. T. (2003), ApJ, 594, L13

Edge, A. C., Stewart, G. C. (1991), MNRAS, 252, 414

Eggen, O. J., Lynden-Bell, D., Sandage, A. R. (1962), ApJ, 136, 748

Eilek, J. A. (2004), in *The Riddle of Cooling Flows in Galaxies and Clusters of galaxies*, edited by T. Reiprich, J. Kempner, N. Soker, 165–+

Ettori, S., Tozzi, P., Borgani, S., Rosati, P. (2004), A&A, 417, 13

Evrard, A. E., Metzler, C. A., Navarro, J. F. (1996), ApJ, 469, 494

Fabian, A. C., Crawford, C. S., Edge, A. C., Mushotzky, R. F. (1994), MNRAS, 267, 779

Fabian, A. C., Nulsen, P. E. J. (1977), MNRAS, 180, 479

Fabian, A. C., Nulsen, P. E. J., Canizares, C. R. (1984), 310, 733

Fassbender, R. (2008), arXiv:0806.0861, 806

Fassbender, R., Böhringer, H., Lamer, G., Mullis, C. R., Rosati, P., Schwope, A., Kohnert, J., Santos, J. S. (2008), A&A, 481, L73

Fioc, M., Rocca-Volmerange, B. (1997), A&A, 326, 950

Gladders, M. D., Lopez-Cruz, O., Yee, H. K. C., Kodama, T. (1998), ApJ, 501, 571

Gladders, M. D., Yee, H. K. C. (2000), AJ, 120, 2148

Gobat, R., Rosati, P., Strazzullo, V., Rettura, A., Demarco, R., Nonino, M. (2008), ArXiv e-prints, 806

Hashimoto, Y., Böhringer, H., Henry, J. P., Hasinger, G., Szokoly, G. (2007), A&A, 467, 485

Hasinger, G., Cappelluti, N., Brunner, H., Brusa, M., Comastri, A., Elvis, M., Finoguenov, A., Fiore, F., Franceschini, A., Gilli, R., Griffiths, R. E., Lehmann, I., Mainieri, V., Matt, G., Matute, I., Miyaji, T., Molendi, S., Paltani, S., Sanders, D. B., Scoville, N., Tresse, L., Urry, C. M., Vettolani, P., Zamorani, G. (2007), ApJS, 172, 29

Hicks, A. K., Ellingson, E., Bautz, M., Cain, B., Gilbank, D. G., Gladders, M. G., Hoekstra, H., Yee, H. K. C., Garmire, G. (2008), ApJ, 680, 1022

Hilton, M., Collins, C. A., Stanford, S. A., Lidman, C., Dawson, K. S., Davidson, M., Kay, S. T., Liddle, A. R., Mann, R. G., Miller, C. J., Nichol, R. C., Romer, A. K., Sabirli, K., Viana, P. T. P., West, M. J. (2007), ApJ, 670, 1000

Hogg, D. W., Baldry, I. K., Blanton, M. R., Eisenstein, D. J. (2002), ArXiv Astrophysics e-prints

Holden, B. P., Blakeslee, J. P., Postman, M., Illingworth, G. D., Demarco, R., Franx, M., Rosati, P., Bouwens, R. J., Martel, A. R., Ford, H., Clampin, M., Hartig, G. F., Benítez, N., Cross, N. J. G., Homeier, N., Lidman, C., Menanteau, F., Zirm, A., Ardila, D. R., Bartko, F., Bradley, L. D., Broadhurst, T. J., Brown, R. A., Burrows, C. J., Cheng, E. S., Feldman, P. D., Golimowski, D. A., Goto, T., Gronwall, C., Infante, L., Kimble, R. A., Krist, J. E., Lesser, M. P., Magee, D., Mei, S., Meurer, G. R., Miley, G. K., Motta, V., Sirianni, M., Sparks, W. B., Tran, H. D., Tsvetanov, Z. I., White, R. L., Zheng, W. (2005), ApJ, 626, 809

Homeier, N. L., Demarco, R., Rosati, P., Postman, M., Blakeslee, J. P., Bouwens, R. J., Bradley, L. D., Ford, H. C., Goto, T., Gronwall, C., Holden, B., Jee, M. J., Martel, A. R., Mei, S., Menanteau, F., Zirm, A., Clampin, M., Hartig, G. F., Illingworth, G. D., Ardila, D. R., Bartko, F., Benítez, N., Broadhurst, T. J., Brown, R. A., Burrows, C. J., Cheng, E. S., Cross, N. J. G., Feldman, P. D., Franx, M., Golimowski, D. A., Infante, L., Kimble, R. A., Krist, J. E., Lesser, M. P., Meurer, G. R., Miley, G. K., Motta, V., Sirianni, M., Sparks, W. B., Tran, H. D., Tsvetanov, Z. I., White, R. L., Zheng, W. (2005), ApJ, 621, 651

Hubble, E. P. (1936), Realm of the Nebulae, by E.P. Hubble. New Haven: Yale University Press, 1936

Jenkins, A., Frenk, C. S., White, S. D. M., Colberg, J. M., Cole, S., Evrard, A. E., Couchman, H. M. P., Yoshida, N. (2001), MNRAS, 321, 372

Jones, C., Forman, W. (1984), ApJ, 276, 38

Kaastra, J. (1992), Internal SRON-Leiden Report, updated version 2.0

Kaiser, N. (1986), MNRAS, 222, 323

Kauffmann, G., Charlot, S. (1998), MNRAS, 294, 705

Kodama, T., Arimoto, N. (1997), A&A, 320, 41

Kodama, T., Yamada, T., Akiyama, M., Aoki, K., Doi, M., Furusawa, H., Fuse, T., Imanishi, M., Ishida, C., Iye, M., Kajisawa, M., Karoji, H., Kobayashi, N., Komiyama, Y., Kosugi, G., Maeda, Y., Miyazaki, S., Mizumoto, Y., Morokuma, T., Nakata, F., Noumaru, J., Ogasawara, R., Ouchi, M., Sasaki, T., Sekiguchi, K., Shimasaku, K., Simpson, C., Takata, T., Tanaka, I., Ueda, Y., Yasuda, N., Yoshida, M. (2004), MNRAS, 350, 1005

Kolb, E. W., Turner, M. S. (1990), Frontiers in Physics, Reading, MA: Addison-Wesley, 1988, 1990

Komatsu, E., Dunkley, J., Nolta, M. R., Bennett, C. L., Gold, B., Hinshaw, G., Jarosik, N., Larson, D., Limon, M., Page, L., Spergel, D. N., Halpern, M., Hill, R. S., Kogut, A., Meyer, S. S., Tucker, G. S., Weiland, J. L., Wollack, E., Wright, E. L. (2008), ArXiv e-prints, 803

Kroupa, P., Weidner, C. (2003), ApJ, 598, 1076

Landolt, A. U. (1992), AJ, 104, 340

Larson, R. B. (1974), MNRAS, 166, 585

Liang, H., Lémonon, L., Valtchanov, I., Pierre, M., Soucail, G. (2000), A&A, 363, 440

Lidman, C., Rosati, P., Demarco, R., Nonino, M., Mainieri, V., Stanford, S. A., Toft, S. (2004), A&A, 416, 829

Lidman, C., Rosati, P., Tanaka, M., Strazzullo, V., Demarco, R., Mullis, C., Ageorges, N., Kissler-Patig, M., Petr-Gotzens, M. G., Selman, F. (2008), ArXiv e-prints, 808

Liedahl, D. A., Osterheld, A. L., Goldstein, W. H. (1995), ApJ, 438, L115

Maraston, C. (2005), MNRAS, 362, 799

Markevitch, M. (1998), ApJ, 504, 27

Markevitch, M. (2006), in *The X-ray Universe 2005*, edited by A. Wilson, volume 604 of *ESA Special Publication*, 723–+

Markevitch, M., Vikhlinin, A. (2001), ApJ, 563, 95

Martini, P., Kelson, D. D., Mulchaey, J. S., Athey, A. (2004), in *Clusters of Galaxies: Probes of Cosmological Structure and Galaxy Evolution*, edited by J. S. Mulchaey, A. Dressler, A. Oemler

Mei, M. (2008), submitted to ApJ

Mei, S., Blakeslee, J. P., Côté, P., Tonry, J. L., West, M. J., Ferrarese, L., Jordán, A., Peng, E. W., Anthony, A., Merritt, D. (2007), ApJ, 655, 144

Mei, S., Holden, B. P., Blakeslee, J. P., Rosati, P., Postman, M., Jee, M. J., Rettura, A., Sirianni, M., Demarco, R., Ford, H. C., Franx, M., Homeier, N., Illingworth, G. D. (2006), ApJ, 644, 759

Menci, N., Fontana, A., Giallongo, E., Grazian, A., Salimbeni, S. (2006), ApJ, 647, 753

Menci, N., Rosati, P., Gobat, R., Strazzullo, V., Rettura, A., Mei, S., Demarco, R. (2008), ArXiv e-prints, 806

Moorwood, A., Cuby, J.-G., Lidman, C. (1998), The Messenger, 91, 9

Mullis, C. R., Rosati, P., Lamer, G., Böhringer, H., Schwope, A., Schuecker, P., Fassbender, R. (2005), ApJ, 623, L85

Mullis, C. R., Vikhlinin, A., Henry, J. P., Forman, W., Gioia, I. M., Hornstrup, A., Jones, C., McNamara, B. R., Quintana, H. (2004), ApJ, 607, 175

Navarro, J. F., Frenk, C. S., White, S. D. M. (1996), ApJ, 462, 563

Navarro, J. F., Frenk, C. S., White, S. D. M. (1997), ApJ, 490, 493

Neumann, D. M., Arnaud, M. (1999), A&A, 348, 711

O'Hara, T. B., Mohr, J. J., Bialek, J. J., Evrard, A. E. (2006), ApJ, 639, 64

Ota, N., Mitsuda, K. (2004), A&A, 428, 757

Peacock, J. A. (1999), Cosmological Physics, by John A. Peacock, pp. 704. ISBN 052141072X. Cambridge, UK: Cambridge University Press, January 1999.

Peebles, P. J. E. (1993), Princeton Series in Physics, Princeton, NJ: Princeton University Press, —c1993

Peng, C. Y., Ho, L. C., Impey, C. D., Rix, H.-W. (2002), AJ, 124, 266

Peres, C. B., Fabian, A. C., Edge, A. C., Allen, S. W., Johnstone, R. M., White, D. A. (1998), MNRAS, 298, 416

Perlman, E. S., Horner, D. J., Jones, L. R., Scharf, C. A., Ebeling, H., Wegner, G., Malkan, M. (2002), ApJS, 140, 265

Perlmutter, S., Gabi, S., Goldhaber, G., Goobar, A., Groom, D. E., Hook, I. M., Kim, A. G., Kim, M. Y., Lee, J. C., Pain, R., Pennypacker, C. R., Small, I. A., Ellis, R. S., McMahon, R. G., Boyle, B. J., Bunclark, P. S., Carter, D., Irwin, M. J., Glazebrook, K., Newberg, H. J. M., Filippenko, A. V., Matheson, T., Dopita, M., Couch, W. J., The Supernova Cosmology Project (1997), ApJ, 483, 565

Persson, S. E., Murphy, D. C., Krzeminski, W., Roth, M., Rieke, M. J. (1998), AJ, 116, 2475

Peterson, J. R., Fabian, A. C. (2006), Phys. Rep., 427, 1

Peterson, J. R., Kahn, S. M., Paerels, F. B. S., Kaastra, J. S., Tamura, T., Bleeker, J. A. M., Ferrigno, C., Jernigan, J. G. (2003), ApJ, 590, 207

Peterson, J. R., Paerels, F. B. S., Kaastra, J. S., Arnaud, M., Reiprich, T. H., Fabian, A. C., Mushotzky, R. F., Jernigan, J. G., Sakelliou, I. (2001), A&A, 365, L104

Pierre, M., Pacaud, F., Duc, P.-A., Willis, J. P., Andreon, S., Valtchanov, I., Altieri, B., Galaz, G., Gueguen, A., Le Fèvre, J.-P., Fèvre, O. L., Ponman, T., Sprimont, P.-G., Surdej, J., Adami, C., Alshino, A., Bremer, M., Chiappetti, L., Detal, A., Garcet, O., Gosset, E., Jean, C., Maccagni, D., Marinoni, C., Mazure, A., Quintana, H., Read, A. (2006), MNRAS, 372, 591

Poole, G. B., Fardal, M. A., Babul, A., McCarthy, I. G., Quinn, T., Wadsley, J. (2006), MNRAS, 373, 881

Postman, M., Franx, M., Cross, N. J. G., Holden, B., Ford, H. C., Illingworth, G. D., Goto, T., Demarco, R., Rosati, P., Blakeslee, J. P., Tran, K.-V., Benítez, N., Clampin, M., Hartig, G. F., Homeier, N., Ardila, D. R., Bartko, F., Bouwens, R. J., Bradley, L. D., Broadhurst, T. J., Brown, R. A., Burrows, C. J., Cheng, E. S., Feldman, P. D., Golimowski, D. A., Gronwall, C., Infante, L., Kimble, R. A., Krist, J. E., Lesser, M. P., Martel, A. R., Mei, S., Menanteau, F., Meurer, G. R., Miley, G. K., Motta, V., Sirianni, M., Sparks, W. B., Tran, H. D., Tsvetanov, Z. I., White, R. L., Zheng, W. (2005), ApJ, 623, 721

Pratt, G. W., Arnaud, M. (2002), A&A, 394, 375

Pratt, G. W., Böhringer, H., Croston, J. H., Arnaud, M., Borgani, S., Finoguenov, A., Temple, R. F. (2007), A&A, 461, 71

Predehl, P., Hasinger, G., Böhringer, H., Briel, U., Brunner, H., Churazov, E., Freyberg, M., Friedrich, P., Kendziorra, E., Lutz, D., Meidinger, N., Pavlinsky, M., Pfeffermann, E., Santangelo, A., Schmitt, J., Schuecker, P., Schwope, A., Steinmetz, M., Strüder, L., Sunyaev, R., Wilms, J. (2006), in *Space Telescopes and Instrumentation II: Ultraviolet to Gamma Ray. Edited by Turner, Martin J. L.; Hasinger, Günther. Proceedings of the SPIE, Volume 6266, pp. 62660P (2006).*, volume 6266 of *Presented at the Society of Photo-Optical Instrumentation Engineers (SPIE) Conference*

Press, W. H., Schechter, P. (1974), ApJ, 187, 425

Reese, E. D., Carlstrom, J. E., Joy, M., Mohr, J. J., Grego, L., Holzapfel, W. L. (2002), *Determining the Cosmic Distance Scale from Interferometric Measurements of the Sunyaev-Zeldovich Effect*, ApJ, 581, 53

Rettura, A., Rosati, P., Nonino, M., Fosbury, R. A. E., Gobat, R., Menci, N., Strazzullo, V., Mei, S., Demarco, R., Ford, H. C. (2008), ArXiv e-prints, 806

Riess, A. G., Strolger, L.-G., Tonry, J., Casertano, S., Ferguson, H. C., Mobasher, B., Challis, P., Filippenko, A. V., Jha, S., Li, W., Chornock, R., Kirshner, R. P., Leibundgut, B., Dickinson, M., Livio, M., Giavalisco, M., Steidel, C. C., Benítez, T., Tsvetanov, Z. (2004), ApJ, 607, 665

Romer, A. K., Viana, P. T. P., Liddle, A. R., Mann, R. G. (2001), ApJ, 547, 594

Rosati, P. (2008), in preparation

Rosati, P., Borgani, S., Norman, C. (2002), ARA&A, 40, 539

Rosati, P., della Ceca, R., Norman, C., Giacconi, R. (1998), ApJ, 492, L21+

Rosati, P., Stanford, S. A., Eisenhardt, P. R., Elston, R., Spinrad, H., Stern, D., Dey, A. (1999), AJ, 118, 76

Rosati, P., Tozzi, P., Ettori, S., Mainieri, V., Demarco, R., Stanford, S. A., Lidman, C., Nonino, M., Borgani, S., Della Ceca, R., Eisenhardt, P., Holden, B. P., Norman, C. (2004), AJ, 127, 230

Salpeter, E. E. (1955), ApJ, 121, 161

Sánchez-Blázquez, P., Gorgas, J., Cardiel, N., González, J. J. (2006), A&A, 457, 809

Sandage, A., Visvanathan, N. (1978), ApJ, 225, 742

Sanderson, A. J. R., Ponman, T. J., O'Sullivan, E. (2006), MNRAS, 372, 1496

Santos, J. S., Rosati, P., Tozzi, P., Böhringer, H., Ettori, S., Bignamini, A. (2008), A&A, 483, 35

Sarazin, C. L. (1988), Cambridge Astrophysics Series, Cambridge: Cambridge University Press, 1988

Schlegel, D. J., Finkbeiner, D. P., Davis, M. (1998), ApJ, 500, 525

Schuecker, P., Böhringer, H., Collins, C. A., Guzzo, L. (2003a), A&A, 398, 867

Schuecker, P., Böhringer, H., Guzzo, L., Collins, C. A., Neumann, D. M., Schindler, S., Voges, W., De Grandi, S., Chincarini, G., Cruddace, R., Müller, V., Reiprich, T. H., Retzlaff, J., Shaver, P. (2001), A&A, 368, 86

Schuecker, P., Caldwell, R. R., Böhringer, H., Collins, C. A., Guzzo, L., Weinberg, N. N. (2003b), A&A, 402, 53

Scoville, N., Aussel, H., Brusa, M., Capak, P., Carollo, C. M., Elvis, M., Giavalisco, M., Guzzo, L., Hasinger, G., Impey, C., Kneib, J.-P., LeFevre, O., Lilly, S. J., Mobasher, B., Renzini, A., Rich, R. M., Sanders, D. B., Schinnerer, E., Schminovich, D., Shopbell, P., Taniguchi, Y., Tyson, N. D. (2007), ApJS, 172, 1

Sersic, J. L. (1968), Cordoba, Argentina: Observatorio Astronomico, 1968

Simard, L., Willmer, C. N. A., Vogt, N. P., Sarajedini, V. L., Phillips, A. C., Weiner, B. J., Koo, D. C., Im, M., Illingworth, G. D., Faber, S. M. (2002), ApJS, 142, 1

Sirianni, M., Jee, M. J., Benítez, N., Blakeslee, J. P., Martel, A. R., Meurer, G., Clampin, M., De Marchi, G., Ford, H. C., Gilliland, R., Hartig, G. F., Illingworth, G. D., Mack, J., McCann, W. J. (2005), PASP, 117, 1049

Spergel, D. N., Bean, R., Doré, O., Nolta, M. R., Bennett, C. L., Dunkley, J., Hinshaw, G., Jarosik, N., Komatsu, E., Page, L., Peiris, H. V., Verde, L., Halpern, M., Hill, R. S., Kogut, A., Limon, M., Meyer, S. S., Odegard, N., Tucker, G. S., Weiland, J. L., Wollack, E., Wright, E. L. (2007), ApJS, 170, 377

Stanford, S. A., Holden, B., Rosati, P., Eisenhardt, P. R., Stern, D., Squires, G., Spinrad, H. (2002), AJ, 123, 619

Stanford, S. A., Romer, A. K., Sabirli, K., Davidson, M., Hilton, M., Viana, P. T. P., Collins, C. A., Kay, S. T., Liddle, A. R., Mann, R. G., Miller, C. J., Nichol, R. C., West, M. J., Conselice, C. J., Spinrad, H., Stern, D., Bundy, K. (2006), ApJ, 646, L13

Strateva, I., Ivezić, Ž., Knapp, G. R., Narayanan, V. K., Strauss, M. A., Gunn, J. E., Lupton, R. H., Schlegel, D., Bahcall, N. A., Brinkmann, J., Brunner, R. J., Budavári, T., Csabai, I., Castander, F. J., Doi, M., Fukugita, M., Győry, Z., Hamabe, M., Hennessy, G., Ichikawa, T., Kunszt, P. Z., Lamb, D. Q., McKay, T. A., Okamura, S., Racusin, J., Sekiguchi, M., Schneider, D. P., Shimasaku, K., York, D. (2001), AJ, 122, 1861

Tanaka, M., Kodama, T., Arimoto, N., Okamura, S., Umetsu, K., Shimasaku, K., Tanaka, I., Yamada, T. (2005), MNRAS, 362, 268

Thomas, D., Maraston, C., Bender, R., Mendes de Oliveira, C. (2005), ApJ, 621, 673

Toomre, A. (1977), in *Evolution of Galaxies and Stellar Populations*, edited by B. M. Tinsley, R. B. Larson, 401–+

Tran, K.-V. H., van Dokkum, P., Illingworth, G. D., Kelson, D., Gonzalez, A., Franx, M. (2005), ApJ, 619, 134

Truemper, J. (1992), QJRAS, 33, 165

van der Wel, A., Franx, M., van Dokkum, P. G., Rix, H.-W., Illingworth, G. D., Rosati, P. (2005), ApJ, 631, 145

van Dokkum, P. G. (2005), AJ, 130, 2647

van Dokkum, P. G., Stanford, S. A., Holden, B. P., Eisenhardt, P. R., Dickinson, M., Elston, R. (2001), ApJ, 552, L101

van Dokkum, P. G., van der Marel, R. P. (2007), ApJ, 655, 30

Vandame, B. (2004), Ph.D. thesis, Nice University, France

Vikhlinin, A., Burenin, R., Forman, W. R., Jones, C., Hornstrup, A., Murray, S. S., Quintana, H. (2007), in *Heating versus Cooling in Galaxies and Clusters of Galaxies*, edited by H. Böhringer, G. W. Pratt, A. Finoguenov, P. Schuecker, 48–+

Vikhlinin, A., Burenin, R. A., Ebeling, H., Forman, W. R., Hornstrup, A., Jones, C., Kravtsov, A. V., Murray, S. S., Nagai, D., Quintana, H., Voevodkin, A. (2008), ArXiv e-prints, 805

Vikhlinin, A., Markevitch, M., Murray, S. S., Jones, C., Forman, W., Van Speybroeck, L. (2005), ApJ, 628, 655

Vikhlinin, A., Voevodkin, A., Mullis, C. R., VanSpeybroeck, L., Quintana, H., McNamara, B. R., Gioia, I., Hornstrup, A., Henry, J. P., Forman, W. R., Jones, C. (2003), ApJ, 590, 15

Visvanathan, N., Sandage, A. (1977), ApJ, 216, 214

von der Linden, A., Best, P. N., Kauffmann, G., White, S. D. M. (2007), MNRAS, 379, 867

White, S. D. M., Frenk, C. S. (1991), ApJ, 379, 52

White, S. D. M., Rees, M. J. (1978), MNRAS, 183, 341

Wilms, J., Allen, A., McCray, R. (2000), ApJ, 542, 914

Zhang, Y.-Y., Finoguenov, A., Böhringer, H., Kneib, J.-P., Smith, G. P., Czoske, O., Soucail, G. (2007), A&A, 467, 437

Zwicky, F. (1937), ApJ, 86, 217

Acknowledgements

Naturally, this thesis wouldn't have been possible without the support, guidance and knowledge transmitted by my two advisors, Hans Böhringer and Piero Rosati, to whom I am very grateful and indebted. Hans sponsored frequent & distant travel and allowed me to pursue more independent lines of research. Piero had a lot of patience, good humour and an incredible capacity to teach, in spite of my tendency to complicate things...

I would also like to thank the organizers of the International Max Planck Research School for Astrophysics, who have created a very well structured PhD program, with adequate and up-to-date graduate courses lectured by many prominent scientists.

I wish to thank my colleagues at MPE and also from other institutes who gave me insight, cleared up doubts and gave me much appreciated advice when I needed it.

It was a pleasure to work with my collaborators, in particular Paolo, who provided many valuable contributions and stimulating discussions.

Observing in La Silla was definitely one of the highlights of this thesis; this was a great experience which I hope to repeat again. Many thanks to the support astronomers, telescope operators and all the friendly personnel in both observatories.

Agradeço à minha família a paciência e o apoio à distancia... pode ser que o meu regresso esteja próximo!

I was very fortunate during this time to have encountered so many inspiring and encouraging people who shared so much with me and made life joyful and meaningful in Munich. You are too many for me to name here so I will just say a heartfelt *obrigada* and hope to enjoy your company wherever I may roam!